SLAC-381
July 1991
(T)

A MEASUREMENT OF THE BRANCHING RATIO OF THE Z BOSON TO BOTTOM QUARKS USING PRECISION TRACKING*

ROBERT GIBBS JACOBSEN

Stanford Linear Accelerator Center
Stanford University
Stanford, California 94309

July 1991

Prepared for the Department of Energy
under contract number DE-AC03-76SF00515

Printed in the United States of America. Available from the National Technical Information Service, U.S. Department of Commerce, 5285 Port Royal Road, Springfield, Virginia 22161. Price: Printed Copy A05, Microfiche A01.

* Ph.D. thesis

Abstract

We use the precision vertex detectors installed in the Mark II detector to measure R_b, the fraction of Z^0 bosons decays into hadrons that include bottom quarks. The Z^0 bosons were created via e^+e^- annihilation at 91 GeV by the Stanford Linear Collider during the 1990 running.

The Mark II tracking system, including the Silicon Strip Vertex Detector and Drift Chamber Vertex Detector, achieves a track position resolution of better than 20 microns for high momentum tracks at the collision point. We describe procedures used to obtain this resolution, including alignment of the Silicon Strip Vertex Detector, and techniques used to quantify the achieved resolution.

We can, for the first time, measure the impact parameters of tracks accurately enough to use the finite b quark lifetime to tag a sample of events containing b quarks. This is done by requiring events which contain at least three tracks with impact parameter greater than three times the calculated impact parameter error. The b quark tagging efficiency is 48% and 85% of the tagged sample events contain b quarks.

Using the 29 events tagged out of a total of 220 identified hadronic Z^0 decays, we measure

$$R_b \equiv \frac{Br(Z^0 \rightarrow b\bar{b})}{Br(Z^0 \rightarrow hadrons)} = 0.230 \pm 0.048 \pm 0.030$$

where the first error is statistical and the second is systematic. This value of R_b is in good agreement with existing measurements made using other methods and the Standard Model prediction of 0.22 using a $\sin^2\theta_W$ value of 0.225.

Acknowledgments

It has been a great pleasure to work with and learn from many people at SLAC. I owe the largest debt of gratitude to my advisor, Jonathan Dorfan, who encouraged me to work on interesting topics. I have learned much of the physicist's craft from him and from John Jaros, Alan Litke and Vera Luth. This dissertation is much the better for all the time they have spent listening while I improved my understanding. I fear that I have learned less particle physics than these teachers had hoped, but I certainly learned more than I ever dreamed.

Don Fujino, Dale Koetke, Bruce Schumm and Steve Wagner worked long and hard to understand the vertex detectors and the physics they make accessible. It's a good thing dissertations are written using 'we', because their ideas and results are integral to this one. The mistakes and misunderstandings are, of course, mine.

The Mark II Upgrade and the vertex detectors are the work of too many people to thank individually here. Group C and the Silicon Strip Vertex Detector Group were unfailing friends. All I can say is that I am grateful for all your efforts, and I won't forget you.

Without the people who worked so hard and so long on the SLC, the data for this thesis would not exist. Without the struggle, I would not have met people like Rick Iverson, Alan Rackelmann and Jim Turner. They taught me a lot about how it all really works. Dave Burke, Witold Kozanecki, Nan Phinney, Marc Ross, and Nobu Toge showed me accelerator physics, perseverance and grace under pressure. Hobey DeStaebler always had something interesting to think about, even when my horizons were vanishingly small.

My Dirk's Jerks and Vector Heads teammates, especially Dave Weiss and Jordan Nash, would often listen to my tales of woe when they should have been concentrating on the game. I thank them for it, but doubt a Ph.D. will improve my batting average.

In addition to my parents, who put up with a lot, there were two special relatives who encouraged my interest in science and technology. My grandfather, Dr. Albert G. Gibbs, was unfailingly patient in explaining the contents of the

latest Popular Science, often before he had a chance to read it. My uncle Ed McLaughlin gave me a copy of 'Space-Time Physics' 19 years ago - I didn't understand the math then, but the magic was unmistakable.

Finally, with deep gratitude, I wish to acknowledge Heather and Katherine Jacobsen. Katherine shared her intuitive understanding of the value of sitting in front of the computer. Heather originally gave me the courage for this adventure, has been unceasingly supportive, and has helped me remember that the writing of a thesis is neither a beginning nor an ending, it's just a pain in the neck.

Table of Contents

Abstract i

Acknowledgments iii

Table of Contents v

Chapter

1 Introduction 1

1.1 The Standard Model 2

1.2 Calculation of Hadronic Decays of the Z^0 Boson . . . 4

1.2.1 Higher Order Corrections to Z^0 Decay Rates . . 6

1.3 Theoretical Extensions of the Standard Model 8

1.4 Prior Methods and Measurements 11

1.4.1 Boosted Sphericity Product 11

1.4.2 High P_T Lepton Tagging 13

1.5 Preview of the Experimental Method 14

1.5.1 Impact Parameter 16

1.5.2 Expected Distributions 16

2 Experimental Apparatus 23

2.1 The Stanford Linear Collider 23

2.2 The Mark II Detector 25
2.2.1 The Central Drift Chamber 26
2.2.2 The Drift Chamber Vertex Detector 31
2.2.3 The Silicon Strip Vertex Detector 37
2.2.4 The Beam Pipe 40
2.2.5 Other Systems 41
2.2.6 The Trigger and Data Acquisition System . . 42
2.3 The Monte Carlo Simulation 44

3 Precision Tracking Method 49
3.1 Track Reconstruction Errors 49
3.1.1 Multiple Scattering 50
3.1.2 Intrinsic Tracking Resolution 50
3.1.3 Total Tracking Resolution 51
3.2 Track Reconstruction Overview 53
3.2.1 General properties of least-squares fits 54
3.3 CDC Tracking 55
3.4 DCVD Tracking 56
3.5 SSVD Tracking 57
3.5.1 Hit Finding 57
3.5.2 Track Fitting 60
3.6 SSVD alignment 60
3.6.1 Use of the CDM 62
3.6.2 The global alignment technique 62
3.6.3 The need for local alignment 64
3.6.4 The local alignment procedure 64
Division into subsamples and cross checks . 67
3.6.5 Systematics 68
3.7 Monte Carlo Verification 71
3.8 IP Finding 71
3.9 Impact Parameter Signing 75

4 Tracking Performance 79
4.1 Resolution 79
4.1.1 Normalized Impact Parameter 79

4.1.2 Cuts 80
4.1.3 Core and Tail Resolution Comparison 81
4.1.4 Leptonic Z Decays 90
4.1.5 Limit on Tracks With Very Large S 91
4.1.6 Resolution Function for All Tracks 92
4.1.7 Effect of Thrust Axis Uncertainty 92
4.1.8 Impact Parameter Distributions 93
4.1.9 Resolution Summary 95
4.2 Tracking Efficiency 96
4.3 Mean IP Finding 96
4.4 Systematic Tracking Biases 99

5 Bottom Quark Tagging 101
5.1 Possible Algorithms 102
5.2 The Measurement Algorithm 104
5.3 The Result 109
5.4 Checks 110
5.4.1 Sensitivity to Tag Parameters 110
5.4.2 Analysis by Differences 110
5.4.3 Tagging Using Mean IP 113
5.4.4 A Tagged Event 114
5.5 Systematic Errors 116
5.5.1 Tracking 117
Core and Tail Resolution 117
Tracks With Very High Significance 118
Tracking Efficiency 118
Material and Multiple Scattering 120
5.5.2 Monte Carlo Input Parameters 120
Fragmentation 120
B Hadron Lifetime 121
Multiplicity 122
B Decay Kinematics 122
Charm Fraction 123
Secondary b Quark Production 123

5.5.3 Monte Carlo Statistics 124
5.5.4 Systematic Error Summary 124
5.6 Tagging Summary 124

6 Conclusions 127
6.1 Observations 128

Appendix

A Tracking Resolution in Pictures 131

B The Mathematics of Precision Tracking 137

C Tracking Resolution Tables 141

References 149

Colophon 155

Indeed, modern theoretical physics is constantly filling the vacuum with so many contraptions that it is amazing a person can even see the stars on a clear night!

M. J. G. Veltman

1 Introduction

High energy physics has developed a mixture of theoretical and experimental results known as the Standard Model. It has given us detailed predictions of particle interactions and properties while so far resisting contradiction.

In this dissertation, we study the specific case of the decay of Z^0 bosons to hadrons containing b quarks. The Standard Model predicts a specific value for the fraction of Z^0 decays to hadrons that contain b quarks, written as

$$R_b \equiv \frac{Br(Z^0 \to b\bar{b})}{Br(Z^0 \to hadrons)}. \tag{1}$$

The sample of Z^0 bosons created by the Stanford Linear Collider (SLC), combined with the unsurpassed charged particle tracking precision of the Mark II vertex detectors, allows us to efficiently separate a clean sample of these events. We then use the size of this sample to calculate R_b. The use of tracking information for this separation is novel and provides a measurement with different systematic errors from existing measurements at SLC and LEP.

In this chapter we discuss the theoretical mechanisms thought to underlie the production of b quarks. In addition to the comparatively simple Standard Model predictions, we survey proposed theoretical extensions which effect R_b. We finish by examining the properties of $Z^0 \to b\bar{b}$ events useful to our analysis technique.

1.1 The Standard Model

During the past 20 years, a combination of experimental and theoretical results has resulted in the Standard Model of particle physics. We cannot cover it in full detail here and excellent discussions exist at many levels.[1][2][3][4] In this section we provide just a brief review.[5][6]

The Standard Model is a gauge theory with an $SU(3)_{color} \wedge SU(2) \wedge U(1)$ gauge structure. It incorporates three forces felt by elementary particles, namely the strong (color) force, the weak force and electromagnetism. These forces act on constituents - six quarks and six leptons. The six quark flavors *u, d, s, c, b, t* carry color, weak and electric charges. The up-type *u, c, t* quarks have an electric charge Q of +2/3, while the down-type *d, s, b* quarks have Q = –1/3. The three charged leptons *e*, μ, τ carry electric charges (Q = –1) and weak charges, while the three uncharged neutrinos (neutral leptons) ν_e, ν_μ, ν_τ carry only weak charges. Since leptons carry no color charge, they are unaffected by the strong interaction. The neutrinos are also electrically neutral, so they have no electromagnetic interactions.

The left-handed fermions are arranged in weak doublets:

$$\begin{pmatrix} u \\ d' \end{pmatrix}_L \quad \begin{pmatrix} c \\ s' \end{pmatrix}_L \quad \begin{pmatrix} t \\ b' \end{pmatrix}_L$$

$$\begin{pmatrix} \nu_e \\ e \end{pmatrix}_L \quad \begin{pmatrix} \nu_\mu \\ \mu \end{pmatrix}_L \quad \begin{pmatrix} \nu_\tau \\ \tau \end{pmatrix}_L .$$

T_3, the third component of the weak charge, is +1/2 for the upper member of each doublet and –1/2 for the lower. The right-handed fermions are individual singlets with a T_3 value of zero. Since the neutrinos are thought to be massless there is no need for right-handed ones.

Flavor is not exactly conserved among the quarks because the weak eigenstates are not the same as the mass eigenstates. It is conventional to represent this by the Cabibbo-Kobayashi-Maskawa mixing matrix[7] relating the mass and weak eigenstates of the left-handed down-type *d, s, b* quarks. This is written

$$\begin{bmatrix} d' \\ s' \\ b' \end{bmatrix} = \begin{bmatrix} V_{ud} & V_{us} & V_{ub} \\ V_{cd} & V_{cs} & V_{cb} \\ V_{td} & V_{ts} & V_{tb} \end{bmatrix} \begin{bmatrix} d \\ s \\ b \end{bmatrix} \qquad (2)$$

where the primed quarks are the weak eigenstates, the unprimed are the mass eigenstates and the meaning of the subscripts will be explained shortly.

Forces in the Standard Model are mediated by the massive vector bosons W^+, W^- and Z^0, plus eight massless gluons and the massless photon. In addition, the minimal version contains a single massive scalar, the H^0. The gluons mediate the strong force by coupling to the color charge of quarks. Since they also carry color, they can couple to each other and must be represented by a non-Abelian group such as SU(3). This part of the Standard Model is called Quantum Chromodynamics (QCD). The gluon-gluon interaction causes the polarization of the vacuum due to virtual quark and gluon pairs to enhance any net color charge in a collection of fermions. This anti-screening, the opposite of the charge screening seen in QED, results in quarks being confined in color-neutral hadrons and in the decrease of the strength of the QCD interaction at small separations (corresponding to large momentum transfers). The detailed process that takes one or more quarks created in a particular reaction and converts them into collections of colorless hadrons is called fragmentation, and is studied phenomenologically. Since the transverse momentum created in the fragmentation process is limited, the collections of hadrons generated from a single high-energy quarks tend to form collimated groups called 'jets'.[8]

The Standard Model accounts for the mass of the weak vector bosons by symmetry breaking.[9] The simplest system uses a single complex Higgs doublet to provide four fields. Three of these are combined with the underlying, massless gauge fields as the missing longitudinal components needed to form massive gauge bosons. The resulting masses are given in terms of three parameters: the fine structure constant (α), the Fermi coupling constant (G_F) and a mixing parameter ($\sin^2\theta_W$).

$$M_W^2 = \frac{\pi\alpha}{\sqrt{2}G_F}\left(\frac{1}{\sin^2\theta_W}\right) \tag{3}$$

$$M_Z^2 = \frac{M_W^2}{\cos^2\theta_W} = \frac{\pi\alpha}{\sqrt{2}G_F}\left(\frac{1}{\cos^2\theta_W\sin^2\theta_W}\right) \tag{4}$$

These same constants specify the electroweak interactions[10][11] between the gauge bosons and the fermions (Figure 1). The photon coupling is just eQ,[12] while the Z^0 coupling is

$$-\frac{e}{\sin\theta_W\cos\theta_W}(T_3 - Q\sin^2\theta_W) = 2\sqrt{2}\left(\frac{M_Z^2 G_F}{\sqrt{2}}\right)^{1/2}(T_3 - Q\sin^2\theta_W), \quad (5)$$

where the right and left-handed fermions have different T_3 values. Interactions mediated by Z exchange is commonly called the neutral weak current.

The $W^{\pm}$ coupling between the members of a left-handed weak doublet is

$$\frac{e}{\sqrt{2}\sin\theta_W}(T_3), \quad (6)$$

which is called the charged weak current. The decay of the b quark is mediated by W bosons (Figure 2). Formally, the b quark mass eigenstate contains some fraction (V_{cb}) of the s' quark weak eigenstate, allowing the W to interact with a (c s') doublet. This determines the subscript labeling in the CKM matrix, as the V_{ij} element appears in the charged-current coupling between the i and j quark mass eigenstates. The small value of V_{cb} (about 0.04) and the limited energy available for the creation of the virtual W boson give the b quark its long lifetime of about 1.2 picoseconds.

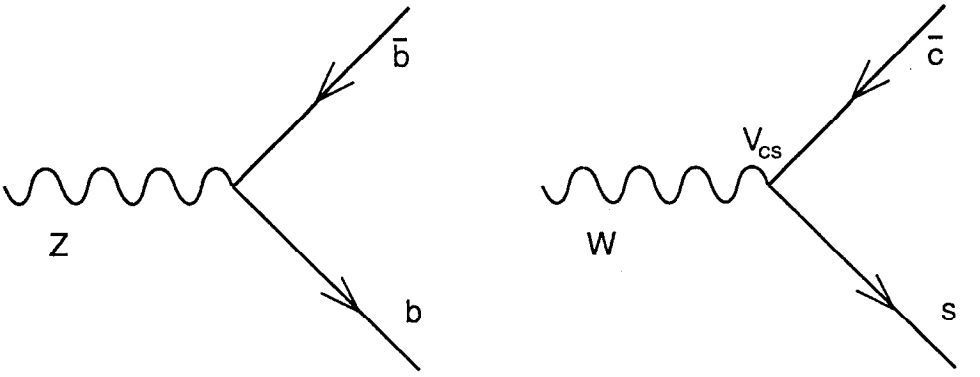

Figure 1 The neutral and charged weak current interactions.

1.2 Calculation of Hadronic Decays of the Z^0 Boson

Figure 3 shows a Z^0 produced via the annihilation of an electron and positron, which then decays to a fermion-antifermion pair. When the center-of-mass energy of

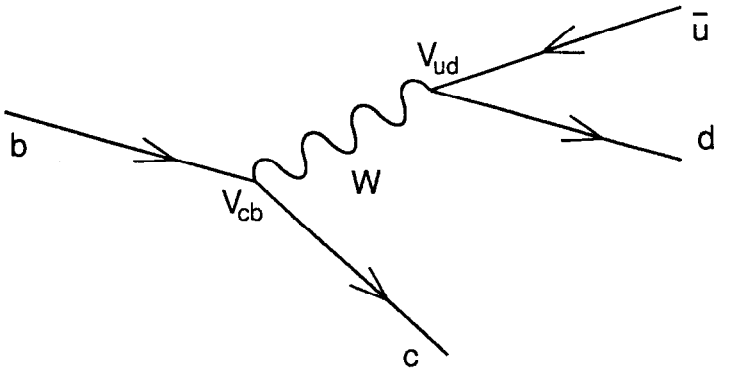

Figure 2 The charged weak current interaction mediating the decay of a b quark. The W boson decays into any of a large number of possible pairs of particles.

the electron and positron is set to the observed Z^0 mass, the calculated width of this diagram is[3]

$$\Gamma(Z^0 \to f\bar{f}) = \frac{DM_Z}{24\pi}\left(\frac{gT_3}{\cos\theta_W} - eQ\tan\theta_W\right)^2 = \frac{G_F DM_Z^3}{\sqrt{2}\,3\pi}(T_3 - Q\sin^2\theta_W)^2 \qquad (7)$$

where we have included the contribution from both right and left-handed fermions as our experimental techniques cannot distinguish them. The color factor D is 1 for leptons and 3 for quarks as there are three indistinguishable color states for the quarks.*

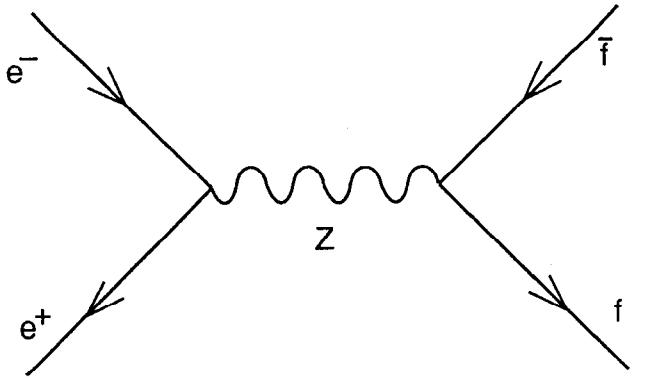

Figure 3 The creation and decay of a Z^0 boson.

* We have neglected the dependance on the velocity of the particles in the final state. For effectively massless particles with $\beta \approx 1$, Equation (7) is correct. A small correction needs to be applied when the final fermions have large masses and thus $\beta < 1$. This is –1.4% for the b quark.

R_b can be found from the individual decay widths

$$R_b \equiv \frac{\Gamma_b}{\Gamma_d + \Gamma_u + \Gamma_s + \Gamma_c + \Gamma_b} \tag{8}$$

where we have ignored the contribution of the t quark as experiment shows it is too massive to be produced as a real particle in Z^0 decays. For $\sin^2\theta_W = 0.225$,[13] R_b is expected to be 0.22.

1.2.1 Higher Order Corrections to Z^0 Decay Rates

So far we have only examined diagrams containing exactly one boson. It is of course possible to add an infinite number of diagrams with more bosons. By adding new boson and fermion lines and interactions in various places in the diagrams, the theory predicts corrections to the first order calculations. These can originate in either QCD or electroweak interactions.

The single largest correction is from radiation of photons by the $e^{\pm}$ before they collide. This bremsstrahlung reduces the center-of-mass energy of the electron-positron annihilation, resulting in a 30% decrease in the cross-section at the peak. The effect on partial and total widths is smaller, about 3%, and is thought to be well-understood. These corrections cancel in the calculation of R_b as they appear in both the numerator and denominator of the ratio, R_b.

The largest QCD corrections are from radiation of soft gluons in the final state. There exist exact calculations of this effect to first order, with higher order calculations only available with various approximations.[14] Most importantly, second order corrections including the effects of the different quark masses are not available. The first order corrections to Γ_b are of the order of 4%, with significant uncertainty from the value of the strong coupling constant. The second and third order contributions are believed to be below 1%. The primary theoretical advantage of considering R_b instead of Γ_b is its relative insensitivity to these corrections due to cancellation in the ratio.

The electroweak corrections also include terms from the emission of photons after the collision. These cancel much like the QCD corrections. There is another class, called 'oblique' corrections, that consist of contributions from additional electroweak bosons added internally. There are various methods for organizing the higher order electroweak diagrams so as to include them in slightly modified values of the masses and coupling constants.[15] This is a subtle point of field theories: we have to determine the parameters of the theory experimentally, which means that

we can only measure the total effect of all possible diagrams. We have no way of directly measuring the numbers which appear in the calculation of the lowest order diagram. Instead, by careful definition we can arrange the constants such that the first order diagrams give essentially the right answer, all higher order diagrams then being arranged to sum to zero. This is one aspect of the renormalization process needed to make physical predictions from quantum field theories.

The electroweak corrections differ slightly between up-type and down-type quarks due to their different couplings to the Z^0, but this is successfully absorbed into the renormalization and need not concern us here.

Z^0 decays to b quarks do have one unique property: because the CKM matrix element V_{tb} is close to unity, diagrams containing virtual t quarks have a large effect on the b quark decay modes.[16] Figure 4 shows the largest contributions. Because the t quark mass is so large, it has a different effect on Γ_b than the u and c quarks have on Γ_d and Γ_s respectively. The center curve in Figure 5[17] shows that R_b can vary a few percent from the first order prediction of 22% due to the effect of the t quark mass. This is considerably beyond our present measurement accuracy, but may eventually be accessible to high statistics experiments.

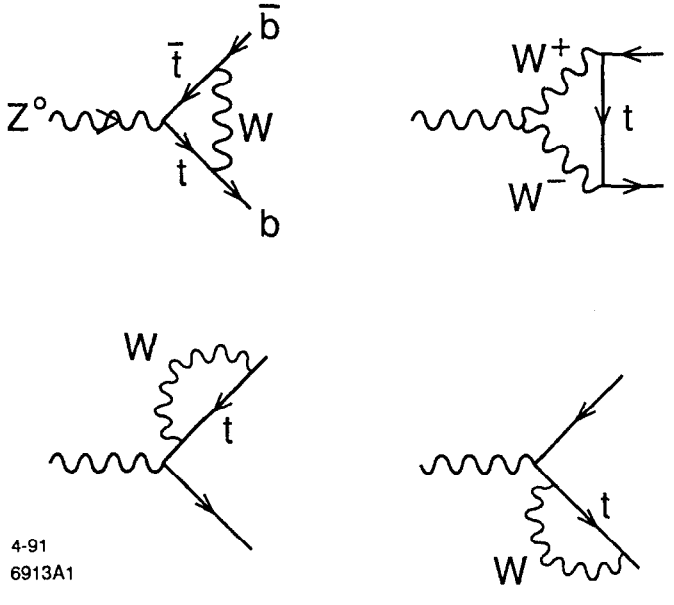

Figure 4 Higher order Standard Model contributions to the Z^0 to b quark coupling from t quarks.

Finally, the coupling of quarks to the Higgs boson of the minimal Standard Model gives the quarks their mass. The large coupling of the Higgs boson to the b

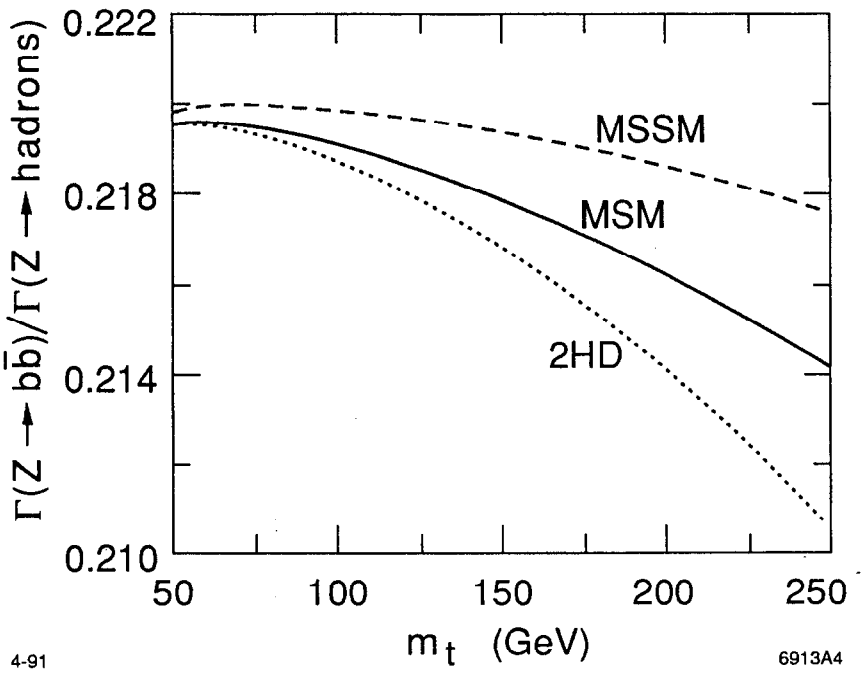

Figure 5 R_b as a function of the t quark mass for the minimal Standard Model (MSM), the standard model with a second Higgs doublet (2HD) and the minimal supersymmetric standard model (MSSM) assuming the parameters of reference [17].

quark (hence the large b quark mass) gives rise to an extremely small dependance of R_b on the mass of the Higgs boson.

1.3 Theoretical Extensions of the Standard Model

The Standard Model explains the masses of the W and Z bosons through the Higgs mechanism,[9] but various other possibilities exist.[18] In addition to the W and Z masses, the same theoretical structures can be used to explain the fermion masses. Because both the b quark and the t quark are massive, whatever mechanism is eventually understood to provide mass will probably have an effect on the dynamics of b quark production.

An example is shown in Figure 6. If, in addition to the Higgs doublet that the minimal Standard Model requires to give mass to the weak bosons, there are additional Higgs doublets, then there will be various charged Higgs particles.*

* Supersymmetry requires two Higgs doublets, so this case is often treated at the start of discussions of the predictions of supersymmetry.[17] It is none-the-less possible to have a more complex Higgs sector without requiring supersymmetry.

Their effect is to drive down R_b through the diagrams of Figure 6. The lower curve in Figure 5 shows that the effect is also at the level of a few percent. In fact, a value for the mass of the t quark is required before a very precise measurement of R_b can demonstrate the effect of a second Higgs doublet.

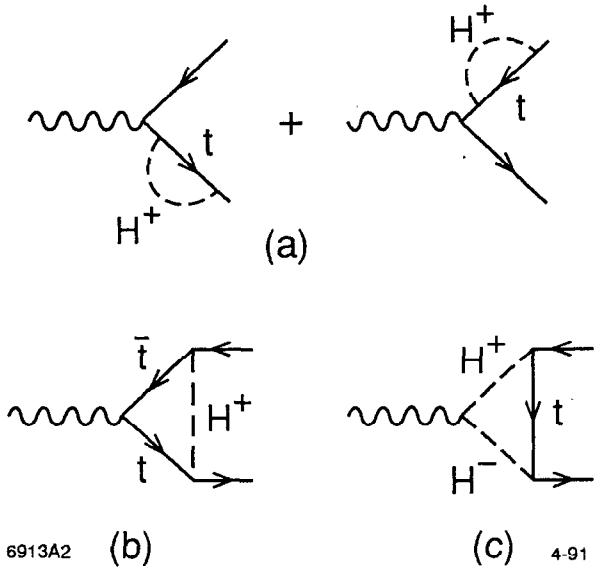

Figure 6 Contributions to the Z^0 to b quark coupling from charged Higgs scalars.

There exists a class of theoretical extensions to the Standard Model called 'supersymmetry'. By postulating new particles and symmetries, these theories hope to explain the huge gap between the particle masses we observe, less than 100 GeV/c^2, and the scale of 10^{12} to 10^{15} GeV/c^2 expected for the theories unifying the QCD and electroweak interactions. In the process, these theories require new partners for all the known particles. Labeled by the whimsical addition of 's' and 'ino' to existing particle names, these partners allow a large number of new diagrams (Figure 7 through Figure 9). In addition to the large number of diagrams, there are a number of parameters for the masses of the new particles. It is hoped that precision electroweak measurements will help to limit the free scope of these theories.[17]

The electroweak theory that now exists is entirely silent about how many different flavors of each particle should exist. Although measurements at SLC and LEP have placed limits on the number of fermions, it is still possible that one or more additional Z bosons exist. Again, measurement of R_b would not conclusively indicate a second Z but would restrict the possible values of its properties.[19]

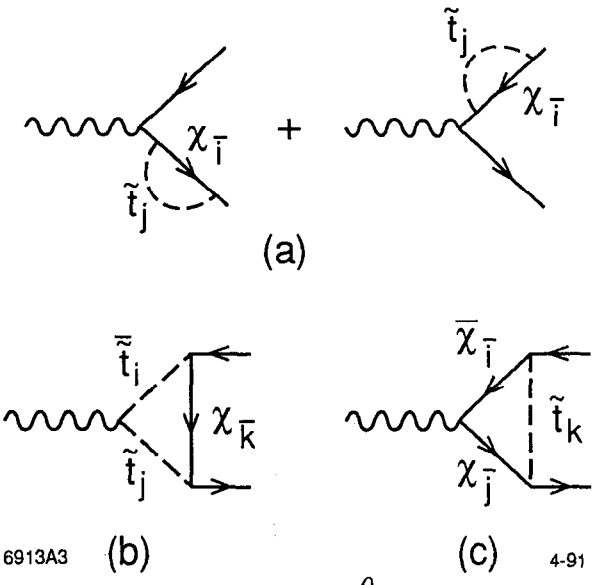

Figure 7 Contributions to the Z^0 to b quark coupling from supersymmetric charginos (χ) and stop quarks ($\tilde{t}$).

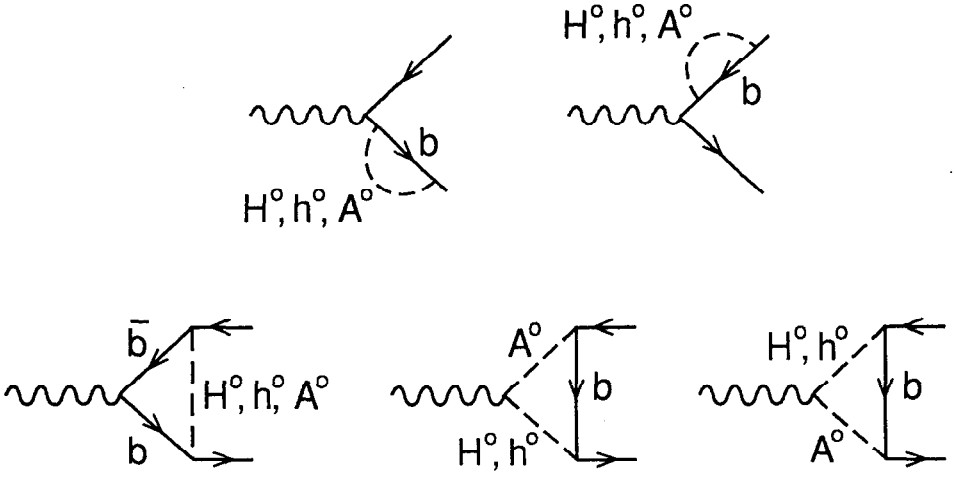

Figure 8 Contributions to the Z0 to b quark coupling from neutral Higgs scalars.

Finally, a class of theories known as 'technicolor' attempts to explain the symmetry breaking underlying particle masses by the dynamics of a new class of particles, called 'technifermions'.[20] As before, these new particles appear in diagrams with topologies similar to those of Figure 6. There are a number of free parameters in technicolor theories, so again a measurement of R_b can only serve as a constraint on the theory, not an existence proof.[19]

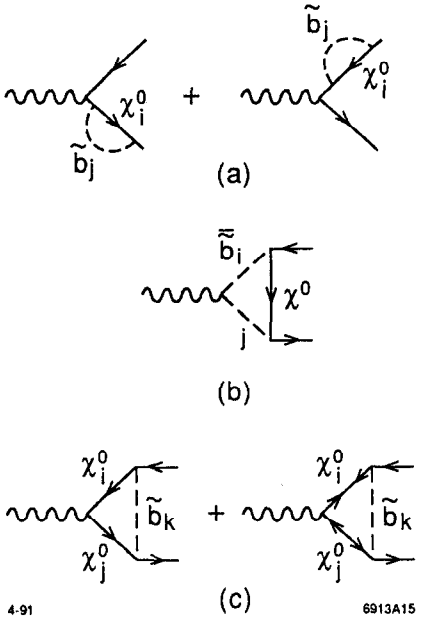

Figure 9 Contributions to the Z^0 to b quark coupling from supersymmetric neutralinos.

We have seen that in the minimal Standard Model, a high precision measurement of R_b can be used to constrain the t quark mass. Since R_b is sensitive to the details of various theoretical speculations at approximately the same level, it is only the combination of R_b and other indirect measurements related to the t quark mass that will provide explicit indications of physics beyond the minimal Standard Model.

1.4 Prior Methods and Measurements

A number of prior measurements related to $Z^0 \to b\bar{b}$ have been made. They draw from the rich set of techniques for measuring Br $(e^+e^- \to b\bar{b})$ used at lower energies. Because of low efficiency, it is not practical to count b quark events by reconstructing the B hadrons known to contain them. Instead, events containing b quarks have been selected on a statistical basis using event shape parameters and specific decay modes. Before turning to our specific measurement, we will briefly survey these alternative techniques.

1.4.1 Boosted Sphericity Product

B mesons can be tagged based on the characteristic "shape" of events containing them. One method that has been used is 'boosted sphericity product'. It is based on

the fact that tracks from the decay of B hadrons tend to contain large transverse momentum (P_T) because of the large mass of the B hadrons. The fragmentation process that makes B hadrons from *b* quarks also tends to give a large fraction of the event's energy to the B hadrons. The tracks from the interaction point (Section 1.5) therefore tend to be softer and at larger angles than in events with only *udsc* quarks.

One way to quantify this shape is 'sphericity', defined as

$$S = \frac{3}{2}\min \frac{\sum_i |\vec{p}_i \times \hat{S}|^2}{\sum_i |\vec{p}_i|^2}, \tag{9}$$

where $\hat{S}$ is a unit vector whose direction is selected to minimize the value of S. $\hat{S}$ is called the sphericity axis. S will be near 1 for spherical events and near 0 for tightly collimated, 2-jet events.

Sphericity can most effectively be calculated for a single jet by transforming to the rest frame of the B hadron contained within it. The large mass of B hadrons results in larger jet sphericity values than found in *udsc* events. Unfortunately, we only know the average B hadron momentum in a jet, so the method involves boosting each jet by a fixed amount, calculating the jet's sphericity, and taking the product of the sphericities found in the event. This distribution is then compared to Monte Carlo either directly or through the efficiency of a particular cut to measure R_b.

TASSO used this method at E_{cm} = 35 GeV. They boosted each jet by β = 0.74 and achieved a B hadron tagging efficiency of 35%. Their method gave a sample purity, defined as the fraction of tagged events containing *b* quarks, of 29%.[21] This is not directly comparable to the results of our method, as the fraction of all events containing *b* quarks is smaller at lower energy.

DELPHI[22] used this method to make the first measurement of R_b. Because of the higher energy available in Z^0 decays, the appropriate value of β was 0.96. A clean separation of *b* quark events was not possible as a purity of only 30% was obtainable using this method. Instead, they fit to the sphericity distribution to obtain an estimate of the contribution from *b* quark events. They found $R_b = 0.209 \pm 0.030 \pm 0.031$, where the first error is statistical and the second is systematic.

1.4.2 High P_T Lepton Tagging

The decay products of b quarks include leptons about 20% of the time. An event sample selected to contain electrons or muons with high P_T is significantly enriched in b quarks.

A number of measurements[23][24][25][26] related to R_b or Γ_{bb} have been obtained using this technique, including one[24] by the Mark II at the SLC.* The limiting systematic error in the initial measurements was the uncertainty in the semileptonic branching ratio, $Br(b \to l+X)$, which was only known to about 10%. This enters because the analysis, by counting leptons, is directly measuring $Br(Z \to b\bar{b}) \times Br(b \to l+X)$. R_b can then be inferred using approximately known branching ratios and widths, although only ALEPH and Mark II have done so in published papers. The ALEPH result has significantly smaller errors and forms the best published measurement of R_b:

$$R_b = 0.220 \pm 0.016 \pm 0.024. \tag{10}$$

Experiment	Quantity	Value
ALEPH	Br(b→e+X) R_b	0.0224±0.0016±0.0010
Mark II	Br(b→l+X) R_b	0.025±0.010±0.005
OPAL	Br(b→μ+X) R_b	0.0226±0.0007±0.0013
L3	Γ_b	385±7±11±19 MeV

Table 1 Published measurements using a lepton tag related to R_b.

L3 has recently used high statistics to measure $Br(b \to l+X)$ and Γ_b simultaneously.[26] They find $\Gamma_b = 385 \pm 7 \pm 11 \pm 19$ MeV, where the first error is statistical, the second is systematic, and the third is the separate systematic contribution from the remaining uncertainty in $Br(b \to l+X)$. They have not published a measurement of R_b.

We can convert the OPAL, Mark II and L3 measurements to measurements of R_b using the L3 measured value of $Br(b \to \mu+X) = 0.113 \pm 0.010 \pm 0.006$ and the Standard Model value of $\Gamma_d+\Gamma_u+\Gamma_s+\Gamma_c+\Gamma_b = 1736.1$ MeV. Table 2 summarizes the

* The data sample used for the measurement in this thesis does not overlap with the sample used in the prior Mark II measurement.

results of these calculations, along with the values of R_b reported by ALEPH and DELPHI.

Experiment	Quantity	R_b Value
ALEPH	R_b	0.220±0.016±0.024
Mark II	Br(b→l+X) R_b	0.22±0.09±0.04±0.02
OPAL	Br(b→μ+X) R_b	0.200±0.006±0.012±0.021
L3	Γ_b	0.221±0.004±0.006±0.010±0.012
DELPHI	R_b	0.209±0.030±0.031

Table 2 R_b values stated or inferred from published measurements. The R_b values for the Mark II, OPAL and L3 results were calculated from the published measurement and other quantities. The last quoted error for those three R_b values is an estimate of the uncertainty in the values used for conversion.

1.5 Preview of the Experimental Method

B mesons are measured[13] to have a lifetime of about 1.2 picoseconds. Combined with their large energy in Z^0 decays, this gives an expected mean decay distance of about 2 millimeters. A detector that can measure the position of a track with a resolution of about 100 microns should be able to distinguish these long-lived particles.

The decay of a B hadron is complex. Most decays include a D meson, which is also long-lived. We refer to the place where the Z^0 decayed as the interaction point, or IP. The point where a B hadron decays is called a secondary vertex, while the decay point of a D meson from the decay of a B hadron is a tertiary vertex. Figure 11 shows the topology of an event.

We will describe the Mark II's tracking system and performance in detail in Chapter 2 through Chapter 4. For our current purposes, we point out that the Mark II has track position resolution typically better than 100 microns in the plane perpendicular to the beams (the xy plane). Since the tracking is done remotely from the collision inside the Mark II beampipe, the event of Figure 11 looks much more ambiguous when viewed by the Mark II reconstruction code. (See Figure 12, where it is difficult to point out the B and D decay vertices without the labels.) A large part of the problem is that in two dimensions, every track crosses every other. Even

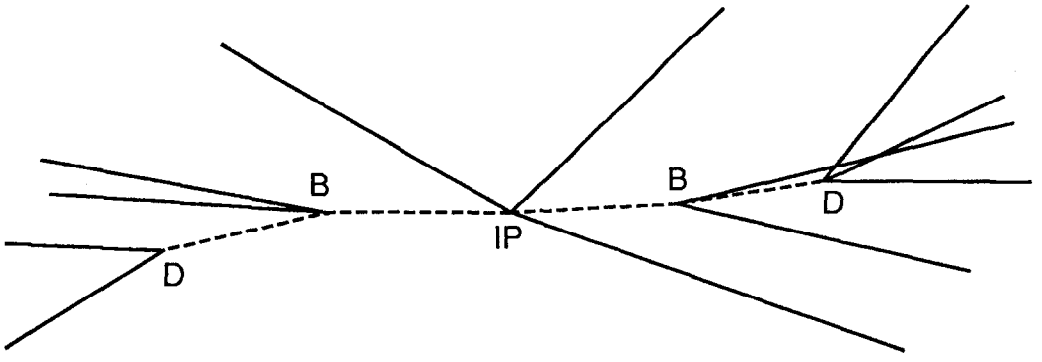

Figure 11 The topology of a Z^0 decay containing b quarks. There is a primary vertex at the IP, plus two secondary B and two tertiary D decay vertices. Note that this is by no means a typical event - most vertices are not this separated, and angles have been exaggerated for clarity.

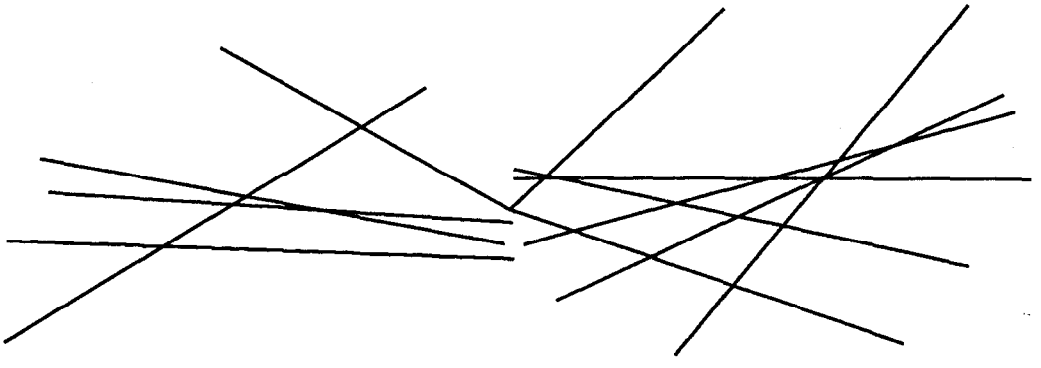

Figure 12 The event of Figure 11 as seen by the Mark II. The tracks are all extrapolated to their point of closest approach too the IP. We have neglected tracking imperfections, including multiple scattering, in this figure.

using kinematic information, such as conservation of momentum at vertices, it is difficult to unambiguously reconstruct the vertices in an event.

On the other hand, the number of tracks that do not originate at the IP in these events is striking. Our analysis concentrates on these miss distances without attempting to identify specific decay vertices..

1.5.1 Impact Parameter

To be precise, the impact parameter (b) is defined* as the distance of closest approach in the xy plane to the assumed IP position.

The impact parameters generated by a particle decay are relatively insensitive to the momentum of the decaying particle so long as it's relativistic. The decay length is $\gamma\beta c\tau$, where τ is the proper decay time, γ and β are the usual relativistic kinematic variables and c is the speed of light. This can be written as $c\tau P/M$ where P and M are the momentum and mass of the decaying hadron. The kink angle (Figure 13) of the flight path of a decay product particle is given by

$$\tan\theta \approx \frac{P_T}{P_L} \tag{11}$$

where P_T is the transverse (perpendicular to the decaying hadron flight path) momentum of the decay product particle and P_L is its longitudinal momentum. For relativistic particles, P_L can be written as a fraction f of the decaying particles momentum P. The impact parameter is then

$$b \approx \text{decay length} \times \tan\theta \approx c\tau f P_T. \tag{12}$$

Since τ and P_T are invariant characteristics of the specific decay and f is approximately determined by the decay product particle multiplicity, the impact parameter distribution is controlled by their distribution. B hadrons have long lifetimes, and their high mass results in large typical P_T so they tend to generate large impact parameters.

1.5.2 Expected Distributions

Figure 14 shows the impact parameter distributions predicted by Monte Carlo simulation of events containing only *udsc* quarks and events containing b quarks. (See Section 2.3 on page 44 for details of the simulation.) The figure is normalized to the number of tracks in our data sample, and 22% of the total events are decays to b quarks. We have assumed perfect resolution in making this plot, so the nonzero impact parameters are all due to the particle decay geometry. The asymmetry

---

* Work on this topic is plagued by ambiguous abbreviations. Impact parameter, bottom quarks and hadrons containing bottom quarks all are represented by various forms of the letter 'b'. To reduce confusion, 'b' will refer only to impact parameter, 'B' will refer only to hadrons (not only mesons unless specified) containing bottom quarks, and '*b* quarks' will always be spelled out as such. Similarly 'IP' will stand for interaction point, where the Z^0 decayed, and 'impact parameter' will be spelled out or represented by 'b'.

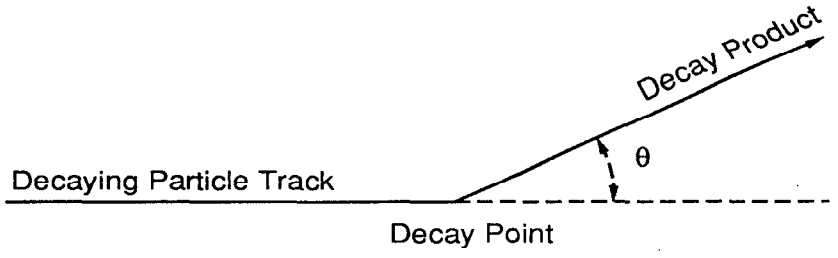

Figure 13 The definition of decay kink angle θ.

comes from our method of choosing the sign of the impact parameter, shown in Figure 15. To emphasize tracks coming from the decay of long-lived particles, we give a positive sign to tracks which cross the assumed decaying particle flight-path, and a negative sign to those that do not. The negative sign then marks tracks that are not consistent with a particle decay geometry. In Figure 14, negative entries come from two sources as shown in Figure 16.* The bins in Figure 14 with impact parameters from -2 to -1 mm show a flat background from the products of K^0 and Λ decays.

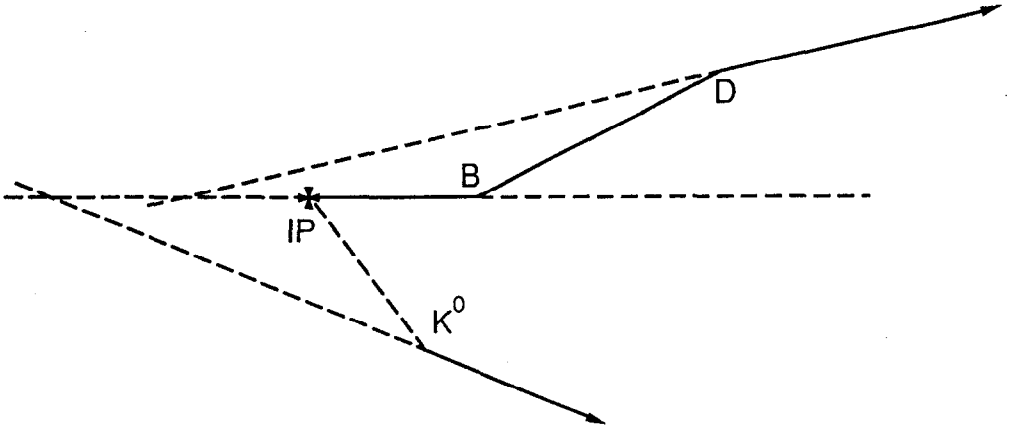

Figure 16 Two geometries that generate negative impact parameters. Tracks from tertiary decays (upper), and tracks from decay of particles that do not travel in the B hadron direction (lower) can be given negative impact parameters.

* In events containing B hadrons, they are assumed to be the decaying particles. Even tracks from tertiary vertices are signed with respect to their original B hadron's direction. In an event containing only *udsc* quarks, the highest momentum two partons set the direction of the assumed decay. This is not as good an approximation, which explains the comparatively large *udsc* quark negative-impact-parameter population between -1 and 0 mm in Figure 14.

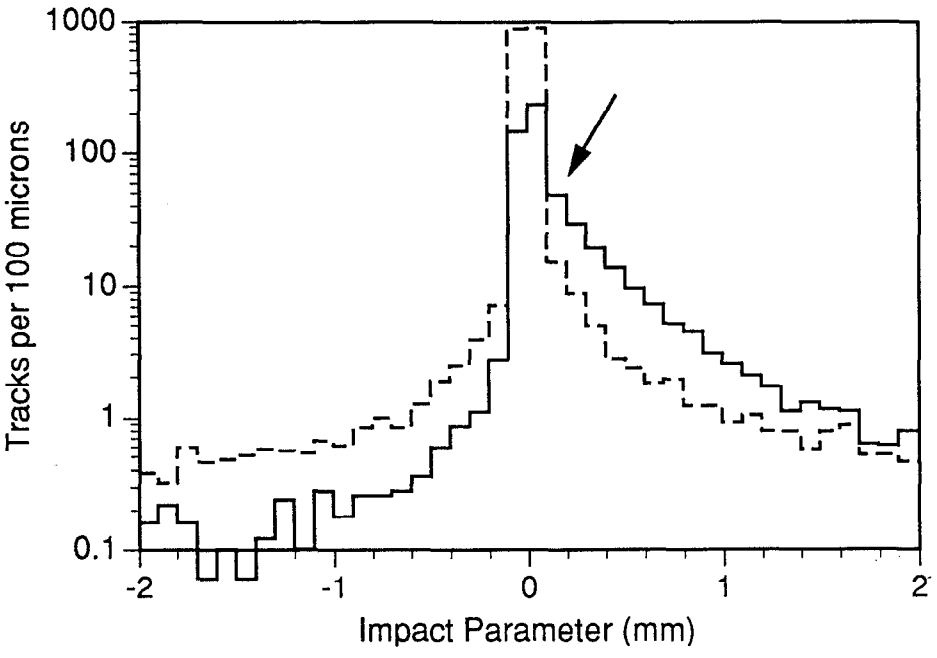

Figure 14 Expected impact parameter distribution for events containing *b* quarks (solid) and events containing only udsc quarks (dashed). Perfect tracking resolution is assumed. Both the IP position and B decay direction are exactly known.

Any realistic tracking system will have a finite resolution. Most of this dissertation examines in great detail the design and performance of the Mark II tracking system. We find an impact parameter resolution varying from 20 to 200 microns, depending on the track momentum and position in the tracking detectors. (The performance is described in several sections, including Section 3.1, "Track Reconstruction Errors," on page 49 and Section 4.1.8, "Impact Parameter Distributions," on page 93.) Using the Monte Carlo resolution model that we will later validate, Figure 17 shows that the distribution grows much wider. More importantly, the large range between the highest and lowest resolution tracks allows the low resolution tracks to dilute quality information about large impact parameters. For example, the bin marked with the arrow in Figure 14 has four times as many tracks from *b* quark events as from *udsc* quark events. In Figure 17 this has degraded to half as many tracks from *b* quark events as *udsc* quark events. This is particularly unfortunate, because this bin now contains a large fraction of the total number of tracks.

By looking at the normalized impact parameter we can reduce the effect of these poor resolution tracks. We will study it in detail later, but normalized impact

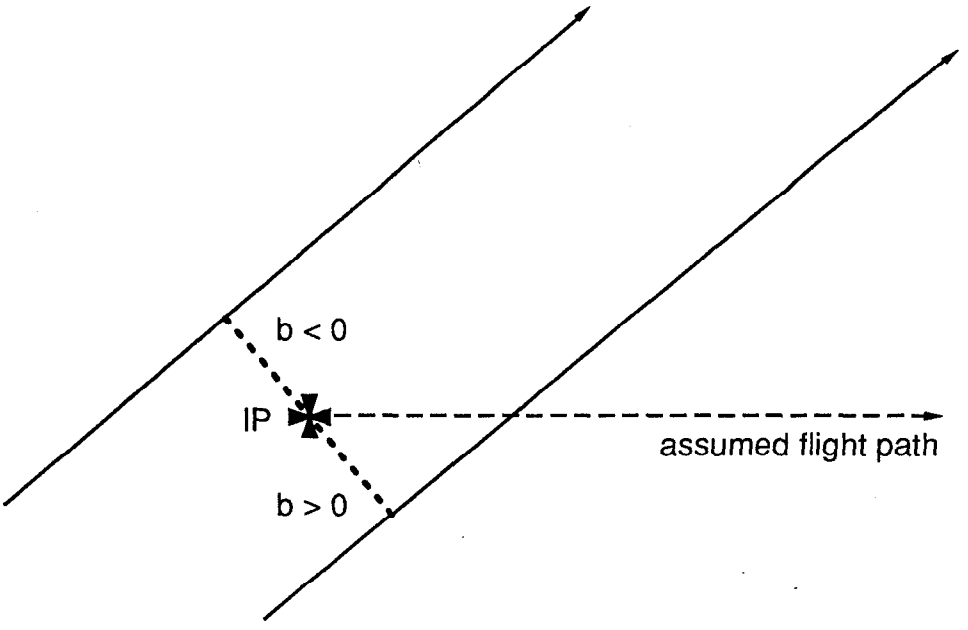

Figure 15 Impact parameter signing. These two tracks cross the assumed flight path of the decaying particle on opposite sides of the IP, and thus are given opposite impact parameter signs.

parameter is defined as the impact parameter divided by the expected impact parameter resolution for the track. Figure 18 shows the normalized error counterpart to Figure 17. In this plot, we still assume that we know the exact position of the IP and the direction of the B hadron(s) for setting the sign of the impact parameter. We have qualitatively regained some of the separation lost to finite resolution.

In a final step toward realism, Figure 19 is the normalized error distribution for the case of not *a priori* knowing the IP position or B hadron decay direction. We use a technique that will be described in Section 3.8 to find an IP in each event. At the same time, we determine a covariance ellipse which represents the uncertainty in that IP determination. Figure 20 shows a sketch of how we project out the effect of that uncertainty in the IP position for a particular track. The expected resolution then consists of the track resolution and IP combined in quadrature. (See Section 4.1.1, "Normalized Impact Parameter," on page 79 for more detail.)

We estimate the B hadron direction using the thrust axis calculated for the event. As shown in Section 3.9 on page 75, this estimator is not perfect. It is occasionally wrong by a large enough angle to change the sign of some B decay

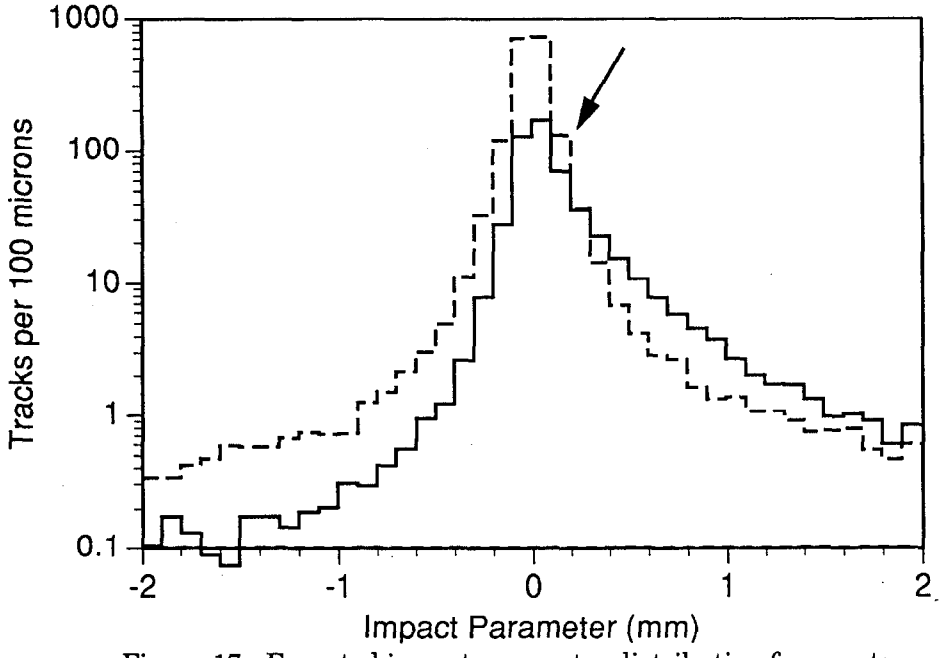

Figure 17 Expected impact parameter distribution for events containing *b* quarks (solid) and events containing only *udsc* quarks (dashed). The tracking resolution observed in the Mark II is simulated. Both the IP position and B decay direction are exactly known. The arrow marks a bin discussed in the text.

impact parameters from positive to negative. This reduces the asymmetry, and thus the signal magnitude.

Figure 19 shows a clear difference between tracks from *b* quark events and events containing only *udsc* quarks, especially for normalized impact parameters greater than 10. Only a small fraction of tracks have such high normalized impact parameters, which makes identifying *b* quark decay events using such a hard cut very inefficient. Because our data sample is of limited size, we will require only normalized impact parameter greater than three. The purity of the sample will be improved by also requiring events to contain several such tracks. This works because, on average, half of the tracks in a *b* quark event are from decay of B hadrons, and are thus likely to have positive normalized impact parameter.

In the next chapter we will review the design and operation of the Mark II, with emphasis on the tracking detectors. Chapter 3 discusses the methods used to combine the raw information into precise track positions. It also describes the methods used to align the Silicon Strip Vertex Detector after installation in the Mark II. Chapter 4 then compares the tracking performance predicted by the Monte

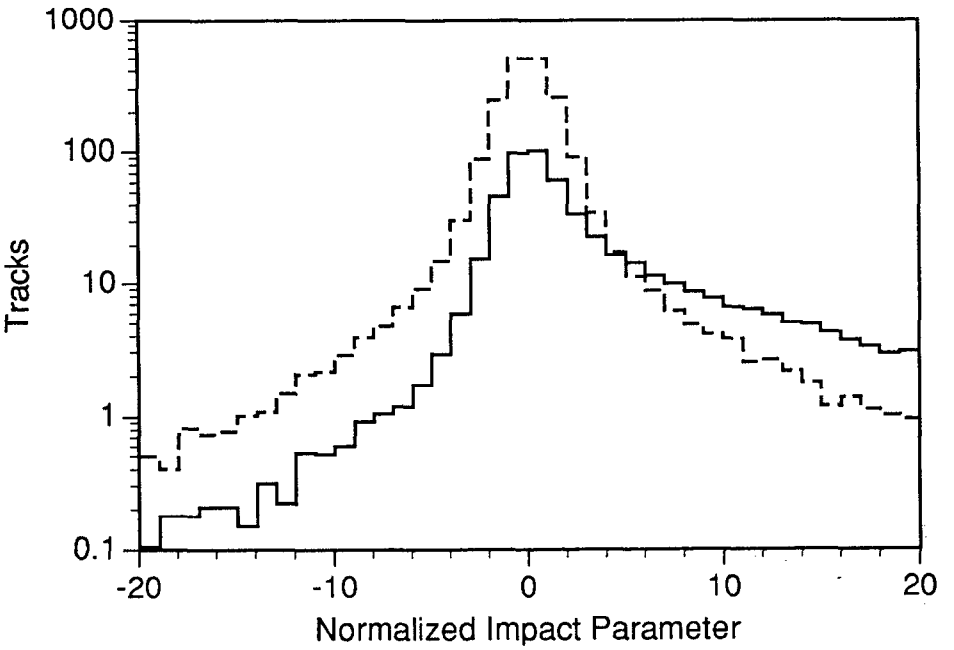

Figure 18 Expected normalized impact parameter distribution for events containing b quarks (solid) and events containing only *udsc* quarks (dashed). The tracking resolution observed in the Mark II is simulated. Both the IP position and B decay direction are assumed perfectly known.

Carlo with that observed in the real data. Chapter 5 begins with a short survey of various methods for identifying the b quark content of the data sample using tracking information. A specific algorithm requiring at least three tracks with normalized impact parameter greater than three is then used to measure R_b and investigate the statistical and systematic errors.

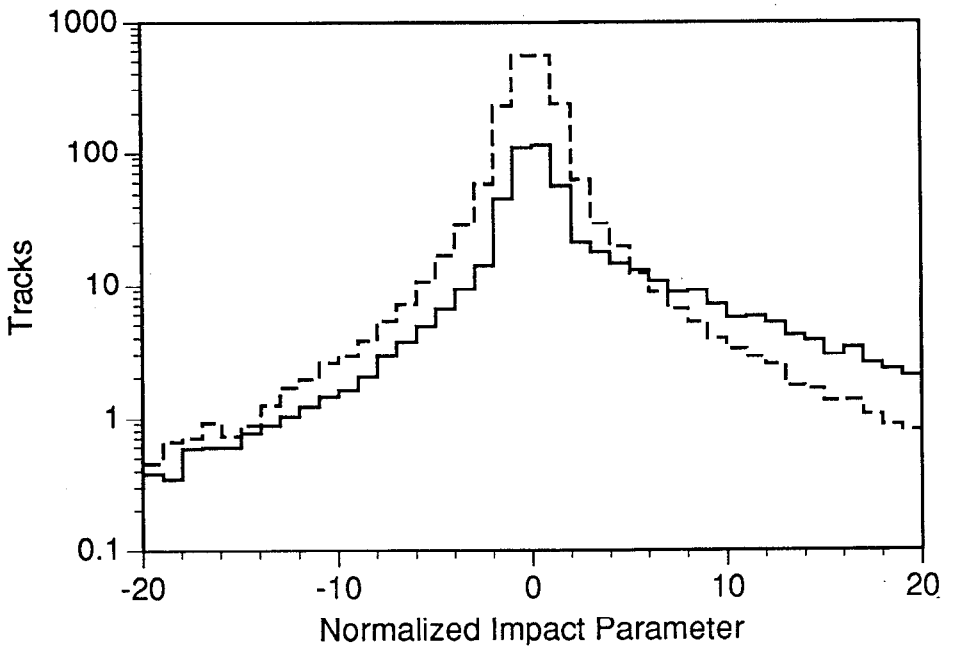

Figure 19 Expected normalized impact parameter distribution for events containing *b* quarks (solid) and events containing only *udsc* quarks (dashed). The tracking resolution observed in the Mark II is simulated. The IP is found in each event, and the thrust axis is used to approximate the B hadron decay direction.

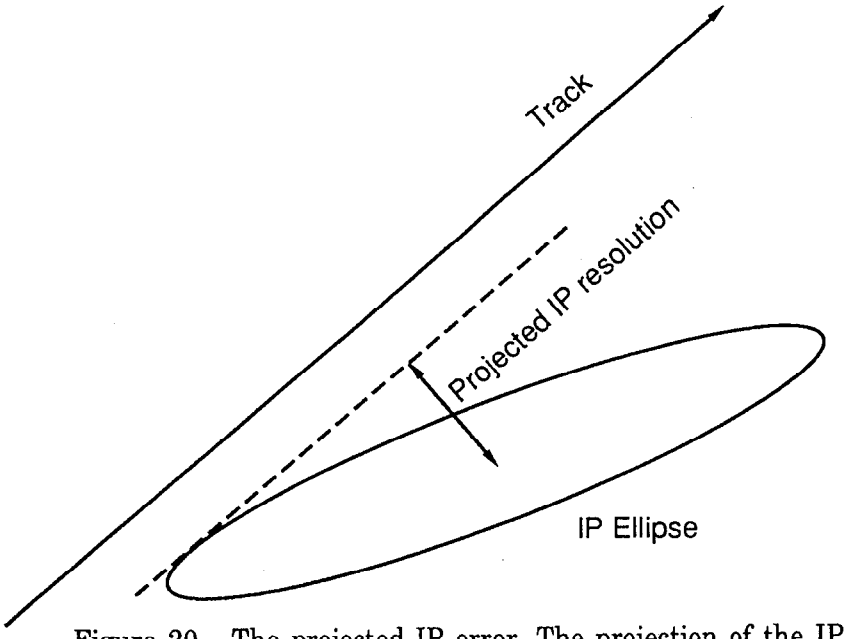

Figure 20 The projected IP error. The projection of the IP resolution ellipse perpendicular to the track forms the IP error, which is then combined in quadrature as part of the total expected impacter parameter resolution.

I never saw a cowboy wearing three guns.

Adm. Arleigh Burke

2 Experimental Apparatus

The present measurement is possible because of two unique pieces of apparatus: the collider that produces the events, and the high precision tracking system of the Mark II detector. The Mark II Monte Carlo event simulation was also important. In this chapter we discuss those characteristics of this apparatus which directly effect our measurement.

2.1 The Stanford Linear Collider

The Stanford Linear Collider (SLC)[27] is the first high energy physics facility of its type. It was built for the express purpose of creating Z^0 bosons using e^+ e^- annihilation. Construction started in 1983 and formally ended in July 1988 at a total cost of approximately $120M.

Figure 21 shows the layout of the SLC. Unlike a circular collider which can recirculate particles for hours, the SLC accelerates bunches of particles, collides them once and then discards them. At the start of each cycle, the injector creates two electron bunches which are accelerated to 1.2 GeV and stored in the north damping ring, where their emittance is "cooled" by synchrotron radiation. During the next cycle, the two electron bunches are injected into the main SLAC linac along with a positron bunch that had been "cooling" in the south damping ring. One of the electron bunches is diverted onto a target at the 33 GeV point, where it produces positrons which are transported and stored in the south ring for the next cycle. The remaining electron bunch and the positron bunch reach the Beam Switch Yard at a typical energy of 45.55 GeV, where the beam profiles are matched to the Arcs for

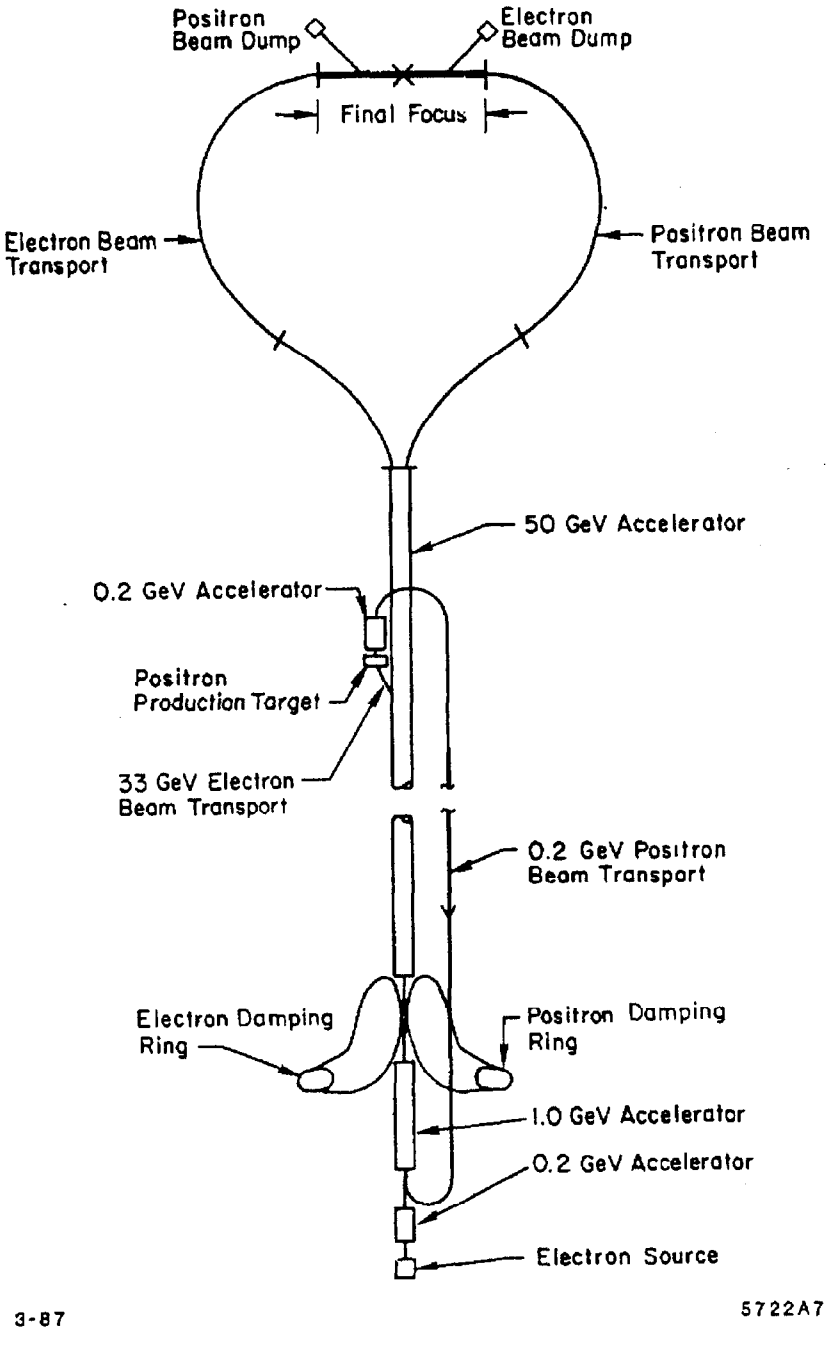

Figure 21 The layout of the SLC. East is toward the top.

transport one kilometer to the Final Focus System. Eighty-three optical elements on each side of the Final Focus demagnify the beams, achieving measured spot sizes of less than 5 microns at the Interaction Point. After collision, the beams are extracted and dumped.

The SLC produced its first Z^0 in April 1989. During the summer and fall of 1989 the SLC intermittently achieved luminosities equivalent to approximately one Z^0 per hour. A total of 528 Z^0 decays were seen during this period. The accelerator complex was then shut down for upgrades to the collider and detector. The new vertex detectors were installed in the Mark II during this time. The Loma Prieta earthquake[28] of October, 1989 caused minor damage and delayed until January 1990 the start of a vertex detector engineering test run. The Mark II recorded 37 Z^0 decays during an integrated two weeks of running during this test run. After another shutdown, a physics run was started in June of 1990. Luminosity was provided intermittently (Figure 22) until November, when the combination of dedicated running and accelerator improvements over the summer allowed accumulation of 40% of our data sample in the last three weeks of the run. A total of 298 Z^0 decays were detected during 1990, of which 220 events pass our cuts as hadronic decays. The SLC center-of-mass energy for these events was 91.0±0.3 GeV.

2.2 The Mark II Detector

The Mark II detector traces it's ancestry back to the original Mark I at SPEAR[29]. Much like George Washington's hatchet*, it has been through a number of upgrades since originally taking data at SPEAR during 1978 and 1979, where it was one of the first detectors to use a large tracking drift chamber.[30] It was upgraded and moved to PEP for running in 1981 through 1984, including pioneering work on using vertex detectors. [31] With the advent of the SLC, the Mark II was upgraded to include an improved Central Drift Chamber.[32] It took 30 pb^{-1} of data in it's new configuration at PEP in the winter of 1985 - 1986, then moved to the SLC interaction hall to be ready for initial SLC turn-on in the summer of 1987. After a first data run in 1989, the Mark II received new vertex detectors for the final run in 1990. The Mark II turned off, perhaps for the last time, on November 21, 1990.

Our measurement of R_b primarily relies on the charged particle tracking and the data acquisition trigger, which we describe in the following subsections. The

* It's had a few new handles and a few new heads, but it's the same hatchet.

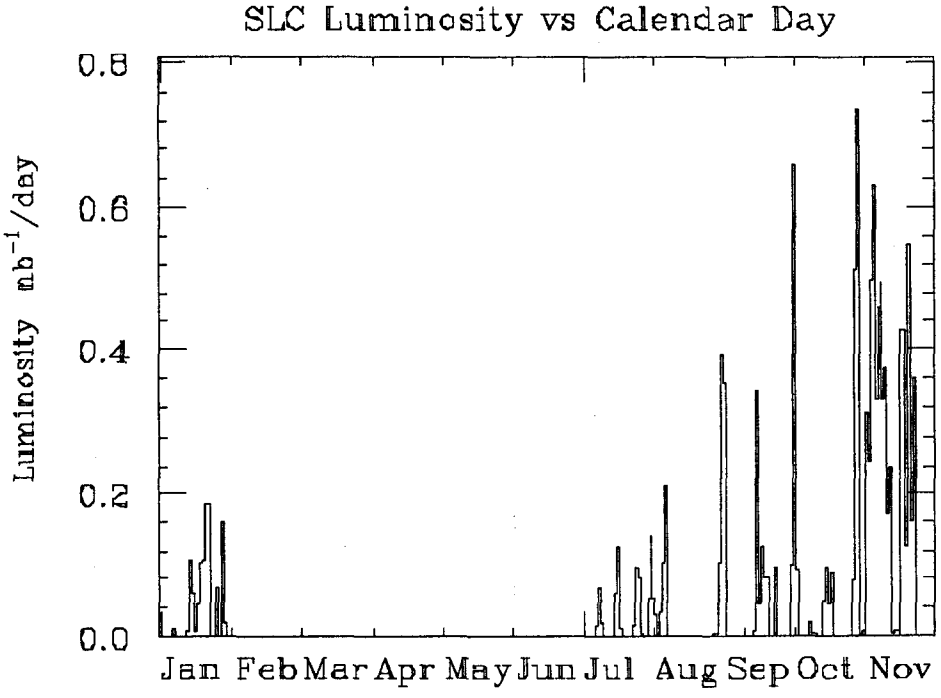

Figure 22 SLC luminosity versus calendar day. Luminosity was calculated from SLC machine information including corrections for detector live-time.

rest of the detector is discussed briefly. A complete description of the detector can be found in Reference [32].

The tracking system consists of three separate detectors which record independent sets of track position measurements. The method of combining the information to find tracks and fit track parameters is described in Chapter 3.

2.2.1 The Central Drift Chamber

The Central Drift Chamber[33] (CDC) provides the primary charged particle tracking in the Mark II detector. It consists of 12 layers of jet-cells, each containing 6 sense wires. The sense wires are staggered ±380 microns to provide local left-right ambiguity resolution. The tracking volume is 2.3 m long and extends from 18 to 151 cm in radius. The detailed cell layout is shown in Figure 24. Six layers of cells are inclined at ±3.8° to the axis to provide stereo information, which is the only measurement of charged track z position in the Mark II. Our data sample was collected while the CDC was in a 4.75kG magnetic field provided by a solenoidal coil.

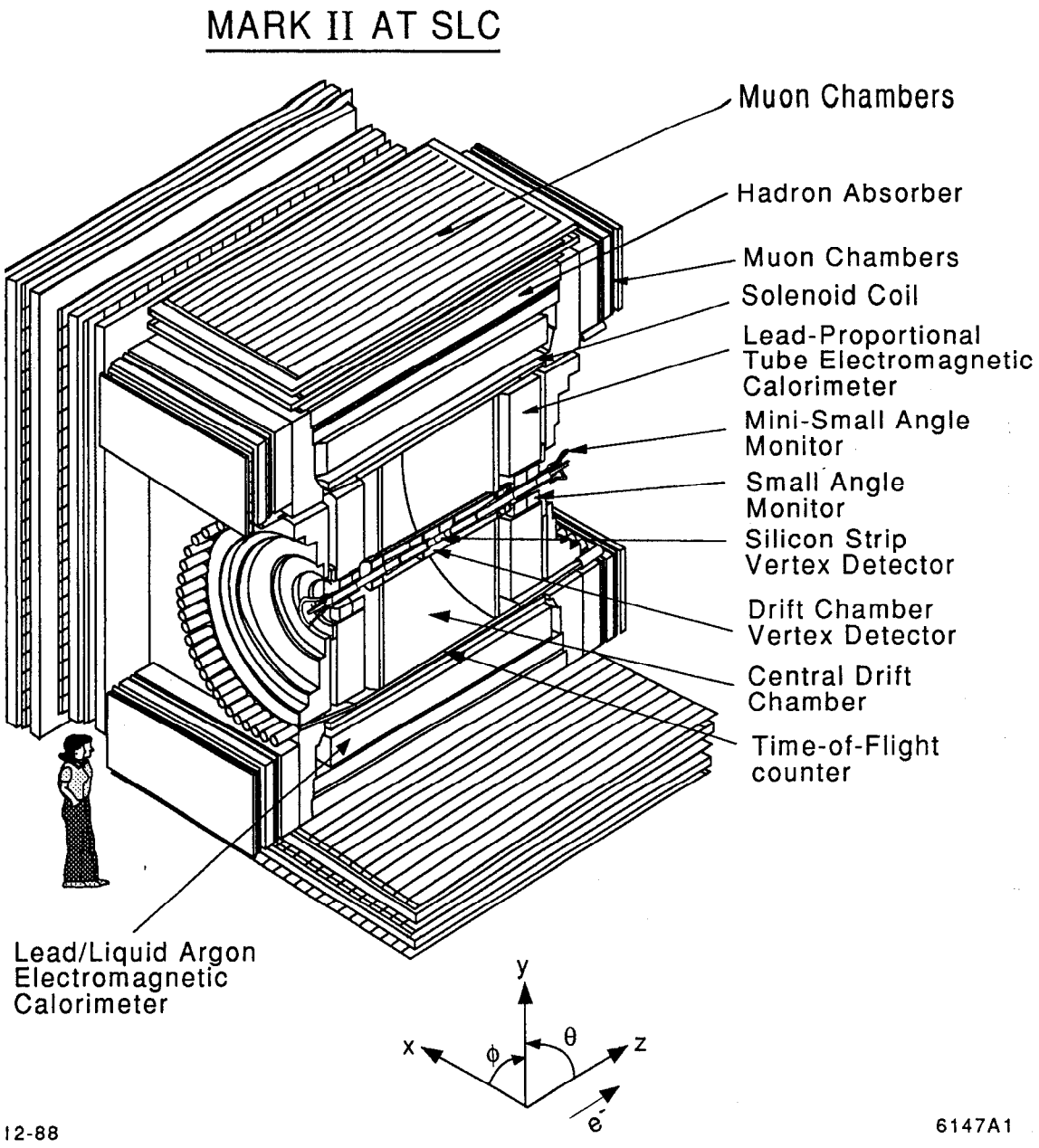

Figure 23 The Mark II Detector in cut-away view.

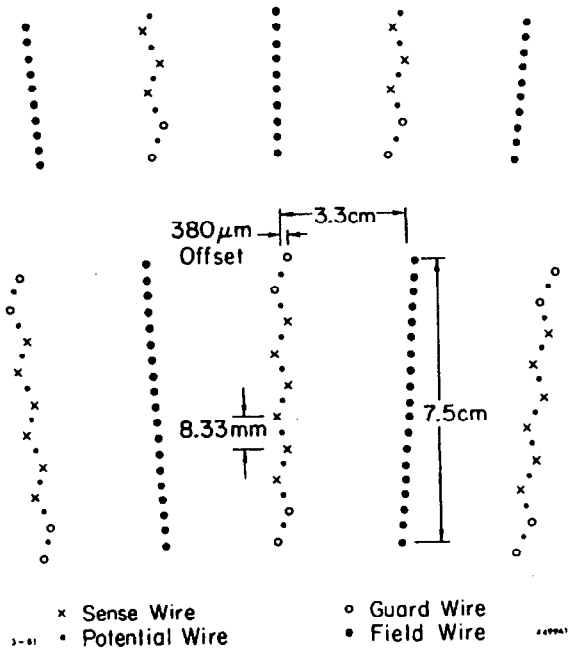

Figure 24 Cell design of the Central Drift Chamber. Each superlayer contains 10 more cells than the superlayer just inside it, resulting in variable staggering between layers.

The signals are read-out after amplification through LeCroy 1879 TDCs and SLAC-designed FASTBUS digitizers (FADCs). Data from the two systems are combined during reconstruction. Pulse position calculated from the FADC data using a correction for time-slewing due to pulse amplitude is preferred to TDC information when both are available. The FADC information is also used for dE/dx particle identification, which is not used in our measurement. Track position resolution averaged about 170 microns (Figure 25) and varied with drift distance.

The efficiency of the CDC has been studied several times.[34] The efficiency for finding hits on found tracks in the data is modeled in the Monte Carlo simulation for each superlayer (Figure 26) and each wire layer (Figure 27). Efficiency for resolving adjacent hits is modeled based on detailed simulations (Figure 28).

The efficiency of the track finding algorithms has been extensively studied[35] in simulation and by comparing the efficiencies for finding tracks using just subsets of the layers. It remains above 97% up to $|\cos\theta| \approx 0.8$, as determined using Bhabha events at PEP and Monte Carlo studies with SLC data (Figure 29). The detected charged multiplicity observed in the data is approximately flat below $|\cos\theta| \approx 0.8$ in agreement with the Monte Carlo (Figure 30). The loss in multiplicity at low

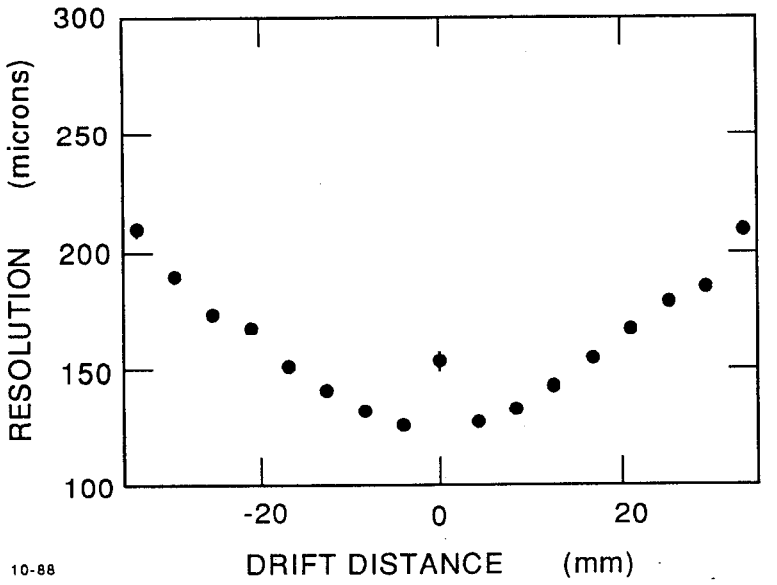

Figure 25 Central drift chamber resolution as a function of drift distance.

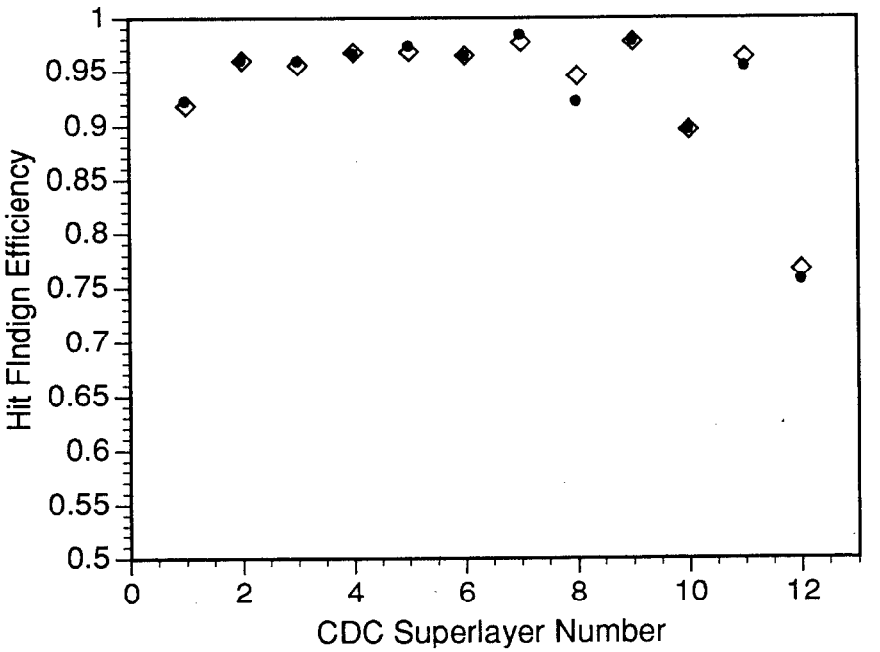

Figure 26 Central drift chamber hit finding efficiency versus superlayer number. The dots are the data and the open diamonds are the Monte Carlo simulation.

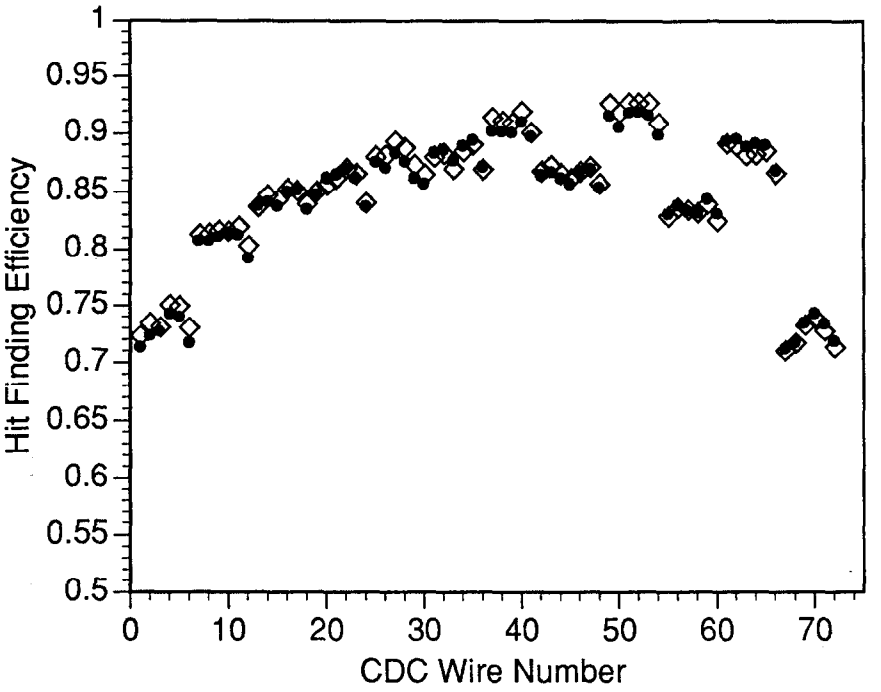

Figure 27 Central drift chamber hit finding efficiency versus wire layer number. The dots are the data and the open diamonds are the Monte Carlo simulation.

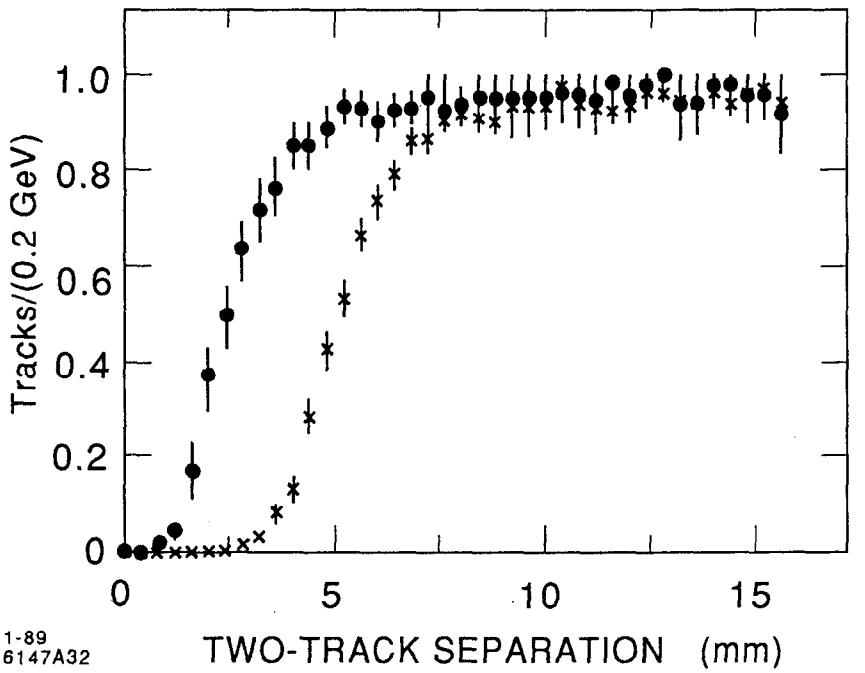

Figure 28 Efficiency for separating two tracks as a function of their distance apart in the Central Drift Chamber. The X's are using TDC information and the circles are using pulse reconstruction in the FADC information.

momentum is well modeled (Figure 31). We will be using only tracks with $|\cos\theta| \leq 0.8$ and $p_{xy} > 0.15$ GeV/c to avoid these regions of reduced efficiency.

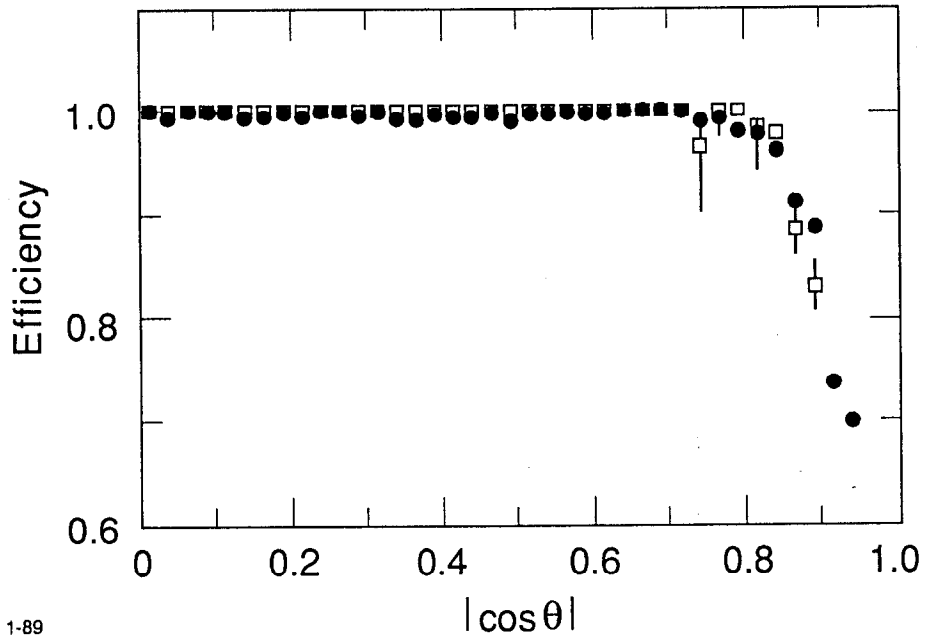

Figure 29 Tracking efficiency in the Central Drift Chamber as a function of polar angle. The dots are a sample of Bhabha scattering tracks from PEP and the boxes are a hadronic Monte Carlo study.[32] See also Figure 30.

2.2.2 The Drift Chamber Vertex Detector

Just inside the radius of the Central Drift Chamber is the Drift Chamber Vertex Detector (DCVD).[36][37] It consists of 10 identical axial cells (Figure 32 and Figure 33) each containing 38 sense wires between 5 cm and 17 cm radius. The wires are positioned within their planes to better than 3 microns, and the planes are believed to be positioned to an accuracy of about 20 microns. The chamber contains CO_2/ C_2H_6 at 2 atmospheres pressure, which is a "cool" gas. Careful pressure and temperature control are required to achieve the desired resolution.

The signals on the wires are read-out by FADCs and the pulse processing is done before the data is written to tape. The time-distance relation was determined using cosmic ray data, and includes a correction from an electrostatic computation and a correction due to track angle with respect to the drift direction. An additional empirical correction is applied as a function of drift distance and wire number (radial position). This correction is about 50 microns on average (Figure 34).

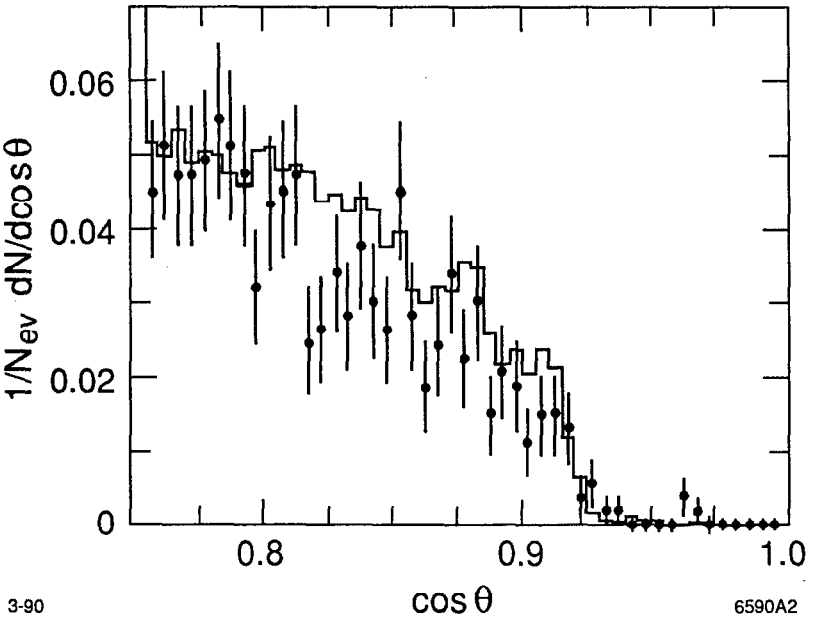

Figure 30 Charged track multiplicity at high polar angle in the central drift chamber.[34] The data used (points) is from the 1989 run. The Monte Carlo simulation (line) is normalized to the total number of events.

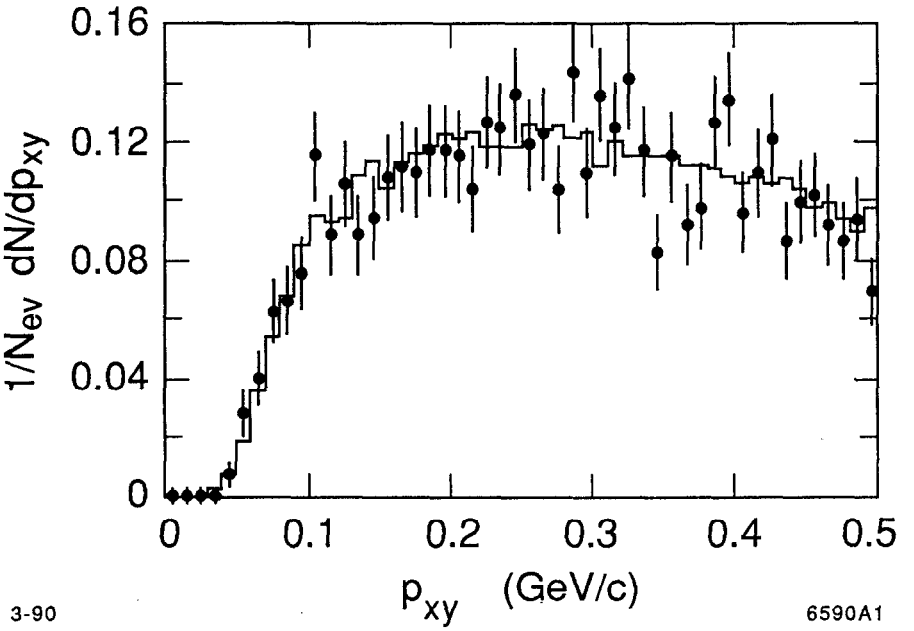

Figure 31 Charged track multiplicity at low momentum in the central drift chamber.[34] The data used (points) is from the 1989 run. The Monte Carlo simulation (line) is normalized to the total number of events.

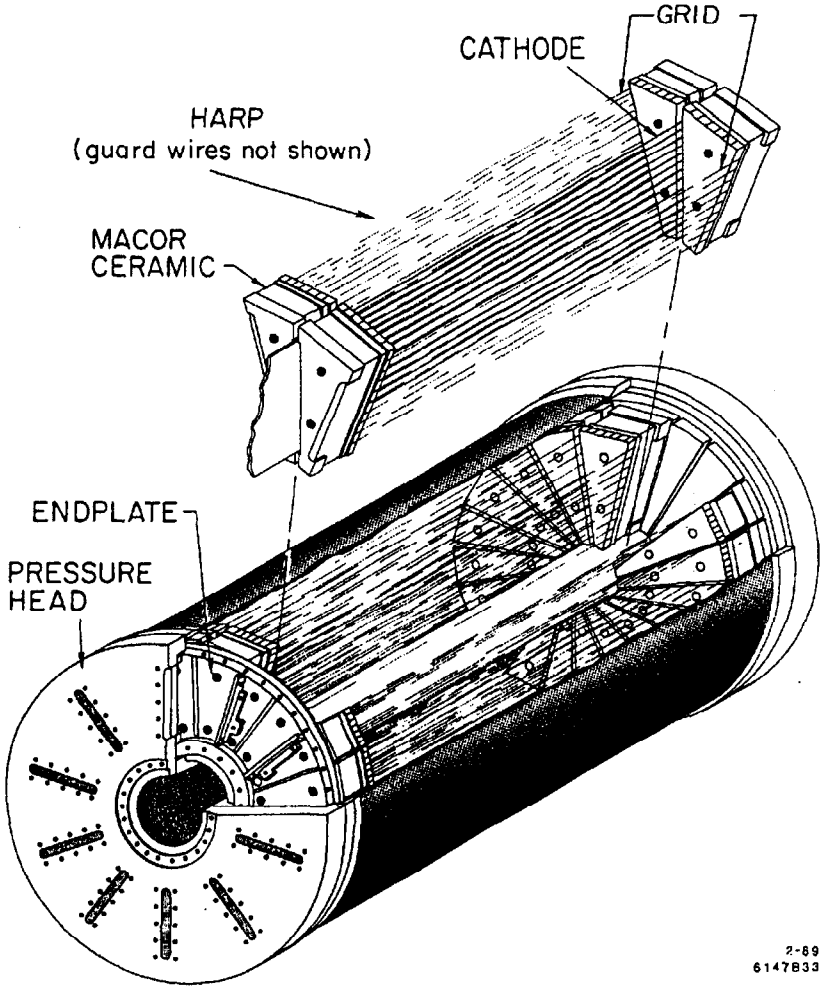

Figure 32 Cut-away view of the drift chamber vertex detector.

The two track separation capability of the DCVD has been studied in simulation (Figure 28). It shows nearly full efficiency for separations as small as 400 microns. The "fake" hit fraction close to a real track is shown in Figure 36. Studies using tracks from hadronic Z^0 decays of closely spaced tracks extrapolated from the CDC show compatible results.

The position resolution of the DCVD was expected to be solely a function of the drift distance and this was confirmed in cosmic ray data. As seen in Figure 37, however, studies of tracking residuals indicate that the resolution is also a function of radial wire number in tracks from hadronic Z^0 decays. This is understood to be due to the properties of the beam-related background present in the detector.[38][39] Random beam crossings show significant occupancy in the DCVD (Figure 37).

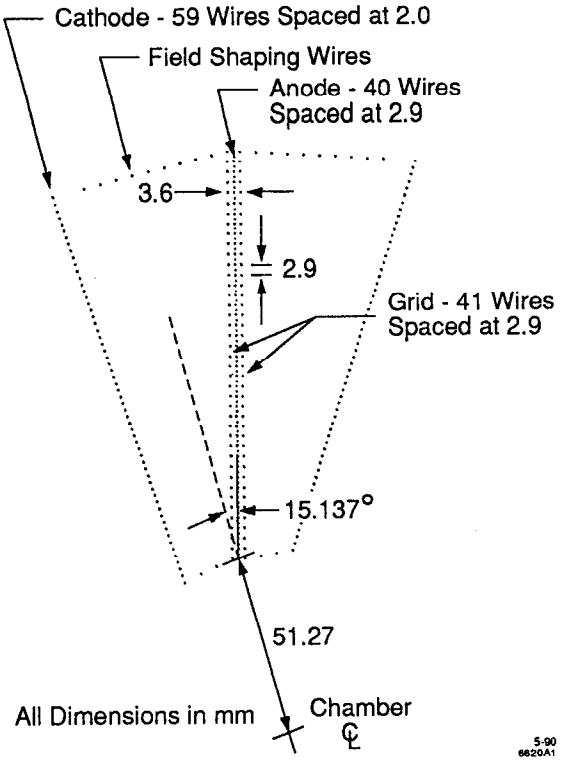

Figure 33 The cell layout of the DCVD.

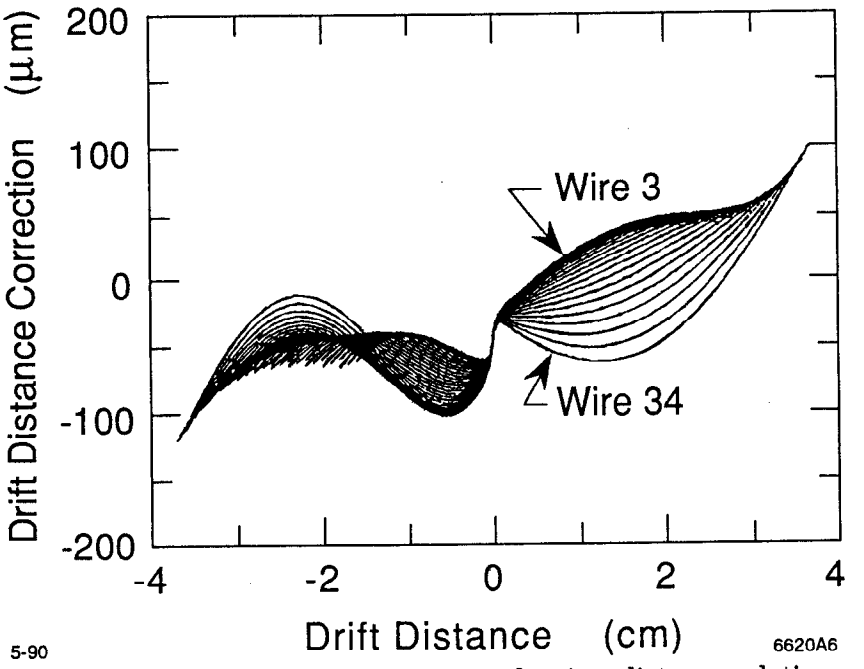

Figure 34 Empirical correction to the time-distance relation found using cosmic rays.

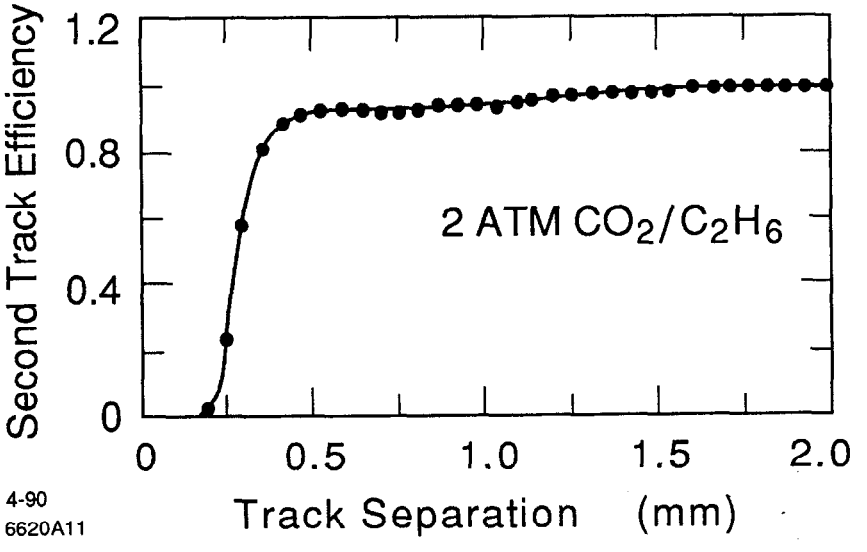

Figure 35 Efficiency to detect a second track as a function of track separation.

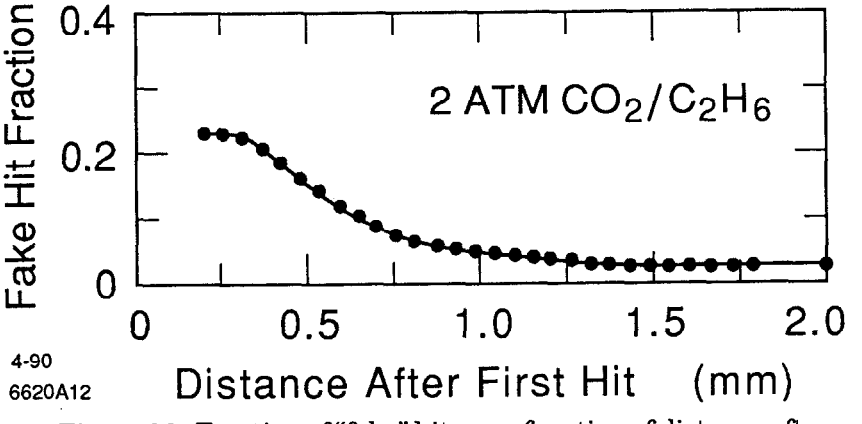

Figure 36 Fraction of "fake" hits as a function of distance after the first hit. Many of these are attributed to real track hits whose position has been perturbed by the first pulse.

Several components are visible. Small, isolated spots are attributed to conversion of low energy photons, with the resulting electron curling up tightly in the magnetic field. The "looping particles" have transverse momenta up to about 5 MeV/c and are almost always overlapping with the beampipe. The remaining "hash" is not well resolved, but is thought to be the result of a large number of low energy particles

from a small electromagnetic shower. All these background components are thought to be due to the loss of less than 100 particles (of 10^{10}) per beam pulse near or in the Mark II detector. Operating the SLC so as to limit these backgrounds to 15% DCVD occupancy, the level desired for least impact on tracking, was not always possible. When conditions were particularly bad, the DCVD would start to draw enough current to trip off its high voltage system, resulting in a few minutes delay while the system was reset.

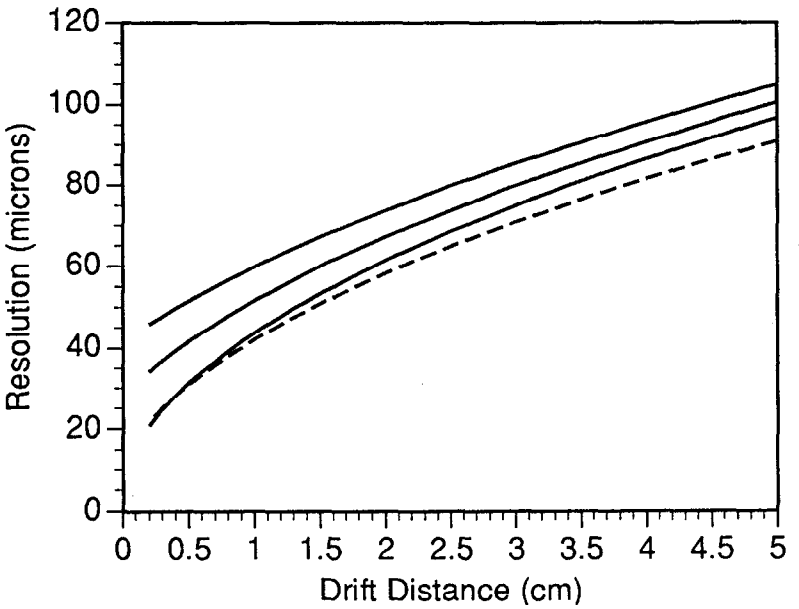

Figure 37 The DCVD resolution as a function of drift distance. The dashed curve is from cosmic ray data. The solid lines are for the innermost wire (upper line), center wire and outer-most wire (lower line).

During the extended periods of bad backgrounds, one or more of the DCVD cells would sometimes be temporarily unable to hold high voltage. When this happened, the afflicted cell would have its high voltage lowered for several hours while data taking continued. No data was recorded from the cell(s) with lowered high voltage. Since this is somewhat correlated with backgrounds, we model this in the simulation by suppressing Monte Carlo generated tracks in cells where the corresponding random trigger had a cell turned down.

Studies of the DCVD/CDC tracking resolution using cosmic ray events indicate that the tracking performance is somewhat worse than expected. For high momentum tracks (P_{xy} > 5 GeV/c), the distance between the two halves of a cosmic ray track found in opposite halves of the chamber was found to be approximately 50

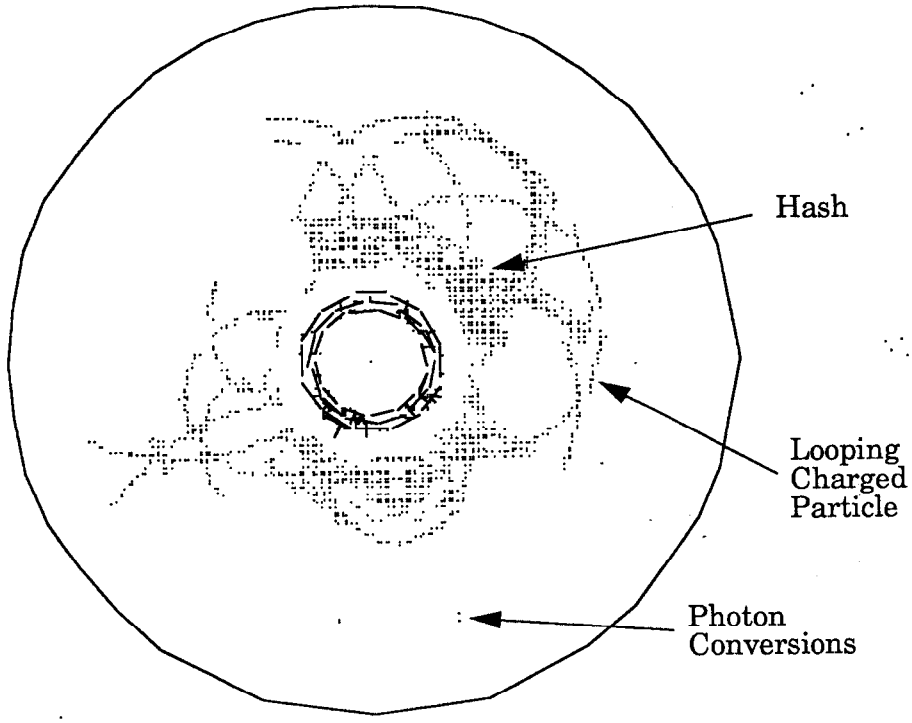

Figure 38 Beam related backgrounds in the DCVD. This event corresponds to 10% occupancy. The outer circle is the radius of the DCVD outer wall. The three concentric rings near the center are the SSVD modules. Each DCVD hit is displayed twice due to the left right drift ambiguity. See text for discussion of the background.

microns RMS, where 40 microns was expected from Monte Carlo simulation studies. Similarly, the acoplanarity of cosmic ray halves, which is a measure of angular resolution, was 0.7 milliradians RMS where 0.40 milliradians was expected. The discrepancy is smaller for lower momentum tracks where multiple scattering dominates.

2.2.3 The Silicon Strip Vertex Detector

Located between the DCVD and the beampipe, the Silicon Strip Vertex Detector (SSVD)[40][41] has three layers of Silicon Detector Modules (SDMs) at radii of 29 mm, 33 mm and 37 mm. Each layer consists of twelve SDMs, each of which contains a 300 micron thick silicon detector with readout via 512 detector diodes arranged as strips (Figure 40). The pitch of the strips in each layer are 25, 29 and 33 microns,

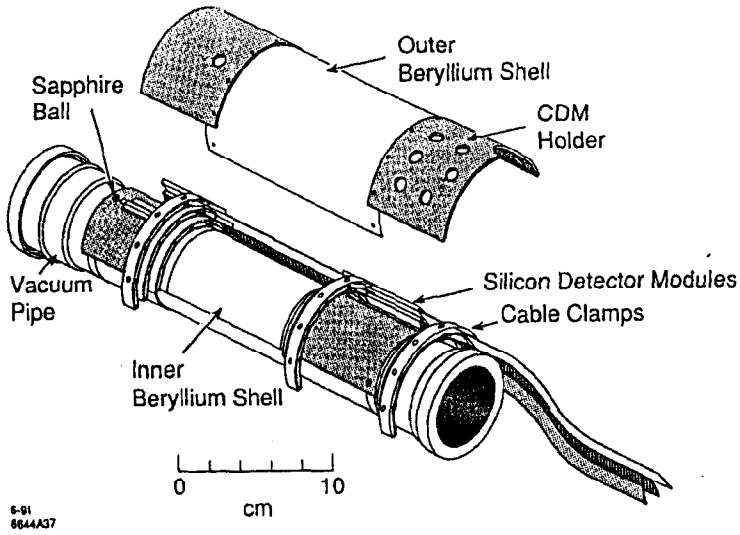

Figure 39 Perspective view of the Silicon Strip Vertex Detector.

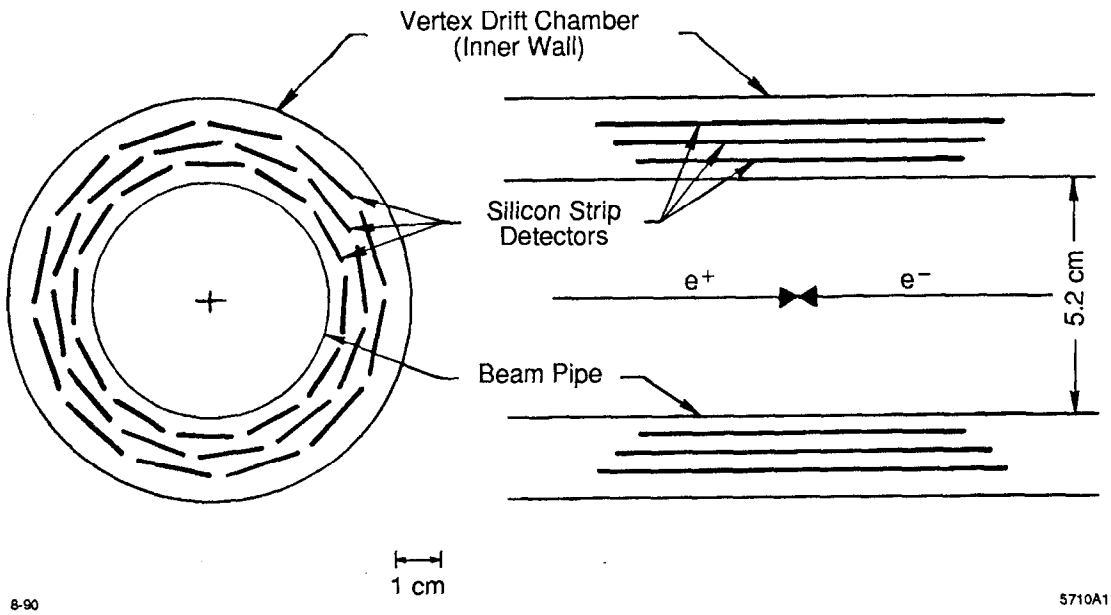

Figure 40 The layout of the SSVD.

respectively. Each SDM, including a small cable underneath the silicon detector, corresponds to 0.55% of a radiation length.

The signals from the detector diodes are amplified and stored by Microplex[42] chips. When Mark II trigger commands readout of an event, the stored signals are transferred to Brilliant Analog-to-Digital Converters[43] (BADCs) which have been modified to support the Microplex interface. The BADC does pedestal subtraction, reformats the data into physical strip order and sparsifies the data by removing strips that are not within 3 strips of a "readout cluster", defined as three strips with a total pulse height over a threshold. The total pulse height in three strips is used as a criteria to keep the SSVD efficient for tracks that penetrate the module at an angle from normal, and thus pass through several strips. The sparsified data are then transferred to the Mark II VAX for recording on tape.

During off-line reconstruction, the data are searched for single strips with a signal greater than 5 times the strip electronic noise. (The most probable energy deposition for a minimum ionizing particle is 16 times the single strip electronic noise.) All neighbors of this strip with pulse height above 1.5 times the electronic noise then form a cluster. The signals in each strip in the cluster are used to form a weighted centroid, which is used as the position of the track at the detector midplane. Studies have indicated that the efficiency for recording a cluster is in excess of 99%. Two track separation is expected to be complete for spacing exceeding 150 microns. Two closely-spaced clusters that have merged into one are resolved by finding two strips with signal greater than 5 times the strip noise, separated by one or more strips with signal less than 5 times the strip noise. This algorithm is expected to function down to 75 microns separation with slightly worsened resolution.

For tracks crossing an SDM at normal incidence, the expected position resolution is about 4 microns for the inner layer.[44] The resolution is expected to scale with the larger strip pitch of the outer layers. Tracks at an angle from the perpendicular also have worse resolution when they extend through several strips. The largest angle for a high momentum particle from the IP is 0.2 radians, which implies that a particle can pass through up to three strips in a single SDM. The increased electronic noise from including more strips in the centroid calculation, plus the uncertainty in the position of the center of charge due to Landau fluctuations in ionization along the particle track, increase the error of the track

position measurement about 20%. We assume resolutions of 5, 6 and 7 microns for the inner through outer layer.

A Capacitive Displacement Measurement (CDM) system[45] was used to monitor the position of the SSVD with respect to the inner wall of the DCVD. Motions of approximately 10 microns are seen on both diurnal and longer time scales.

One of the SDMs in the outer layer failed during installation, probably due to a cable fault. A second SDM failed during the run, and was not functioning for the last half of the events. There were several occurrences of large pedestal shifts in a single SDM, which prevented use of the data from that SDM for typically 5 hours until the next calibration of the detector. These regions were temporarily marked as bad for those runs. Additionally, about 1% of strips were permanently marked as bad due to poor signal-to-noise performance. Clusters which contain one or more bad strips are not used in the analysis. The same bad strip map is used during simulation.

Backgrounds in the SSVD were in general not a limiting factor. Occupancy on random beam crossing were generally below 4%, which did not significantly degrade the matching of hits to tracks. The total radiation dose received by the SSVD was measured by dosimeters to be about 100 rads, including exposure during accelerator studies and tuning.

2.2.4 The Beam Pipe

The Mark II beam pipe is 25 mm in radius inside the SSVD (Figure 41). The section of the pipe extending 4.8 cm on either side of the collision point is aluminum of 410 microns thickness and has a nominal 25 micron thick internal coating of copper to suppress scattered synchrotron radiation. This is nominally 0.65% of a radiation length.

Two mechanisms are provided for inserting forks carrying thin (4 micron) carbon fibers[46] into the beams. These fibers are used for measuring the beam profile and position. Due to excessive scattering of synchrotron radiation, they can only be inserted while the Mark II detector is off. The forks are made of 750 micron thick aluminum. They occupy approximately 11% of the SSVD fiducial solid angle. We simulate the additional material of the forks in detail in the Monte Carlo. We do not have sufficient low momentum tracks to empirically map the extra material of the forks, although that is possible in principle, so their position is approximated in the track reconstruction.

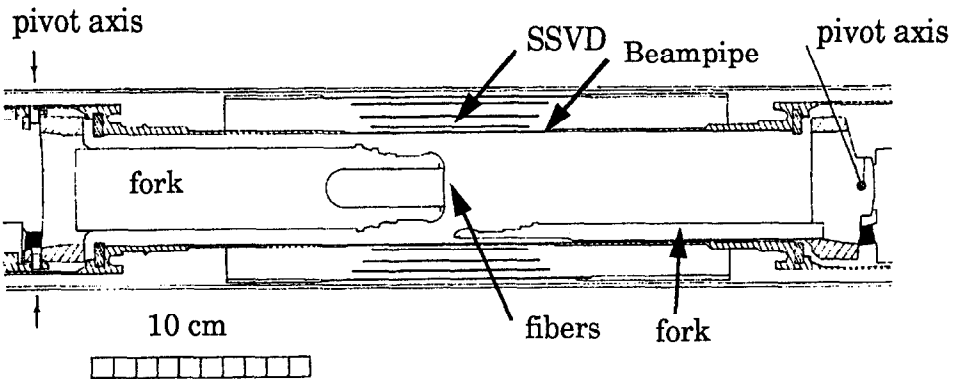

Figure 41 The beam pipe and wire flippers. The two forks carrying the profile-measuring fibers are shown. The mechanisms for inserting the forks surround the two pivot axes.

2.2.5 Other Systems

As shown in Figure 23, there are a number of additional detector systems. As this measurement does not depend critically on these, we only briefly survey them in this subsection. More complete descriptions are available elsewhere.[32][34]

The time-of-flight system (TOF) is found at radii between the central drift chamber and the solenoid. It consists of 48 counters arranged in a cylinder with photomultiplier readout at each end. Some of the light guides were damaged during the earthquake, resulting in decreased transmission and degraded resolution. Its resolution before the earthquake averaged 220 psec.

Outside the solenoid is the Liquid Argon Calorimeter (LAC). It is organized as eight independent electromagnetic calorimeter modules. Each contains 18 layers of lead strips ganged into 6 interleaved readout layers. There are 326 channels per module. The calorimeter has a total solid angle coverage of 63.5% of 4π. The 3° gaps between the modules are covered by scintillation counters to detect energy leakage. The LAC achieves a resolution σ/E of 4.6% for Bhabha electrons at PEP (14 GeV).

The outermost layer of the Mark II is the muon system. It consists of four planes of proportional tubes interleaved with steel hadron absorber. There are approximately 7 nuclear interaction lengths of material between the outermost layer of the muon system and the Interaction Point. The muon system covers 45% of

the 4π solid angle. An upgrade to extend this coverage to 60% of 4π was installed before the summer 1990 running.

Each end of the CDC is covered by an Endcap Calorimeter (EC). These are lead/ proportional tube electromagnetic calorimeters. Each consists of 36 layers of 0.5 X_0 thickness lead, each of which is followed by a plane of 191 proportional tubes. Together with the liquid argon calorimeter, the coverage is 86% of the total solid angle.

A number of very-small-angle monitors on the beampipe were removed during the vertex detector installations. The MiniSAMs are the lowest angle detector remaining. There is one on each end of the beampipe covering polar angles from 15 to 25 milliradians. Each MiniSAM consists of six layers of scintillator interleaved with a total of 15 X_0 of tungsten slabs. They were used as luminosity monitors despite high occupancy from low radius machine backgrounds.

The primary luminosity monitor was the Small Angle Monitor (SAM). It was a combined tracking detector and calorimeter covering from 50 to 160 milliradians. The tracking section consisted of nine layers of drift tubes followed by a calorimeter with six layers of lead and proportional tubes.

2.2.6 The Trigger and Data Acquisition System

The Mark II data acquisition was started by the logical OR of three independent triggers of interest to the present analysis:

1. The CDC data from each beam crossing was searched for charged tracks. A cell was considered hit if at least four of the six wires have had their TDC fire. The list of hit cells was transferred over a serial bus into a group of 'curvature modules', which were dedicated hardware which searched for a coincidence of cells hit with a predefined pattern which represented a track (Figure 42). This trigger requires at least two tracks be found.
2. The SSP-based Software Trigger used a computer on a FASTBUS module (SLAC Scanner Processor, SSP) to search signals from the LAC and EC for 'towers' indicating localized energy deposition. A tower over 2.2 GeV (3.3 in the Endcap) triggered the detector.
3. The total energy in each calorimeter (LAC, EC, SAM and MiniSAM) was compared to thresholds. The sum of the energy in the LAC and EC exceeding threshold caused the Total Energy Deposition trigger (TED) to trigger the detector.

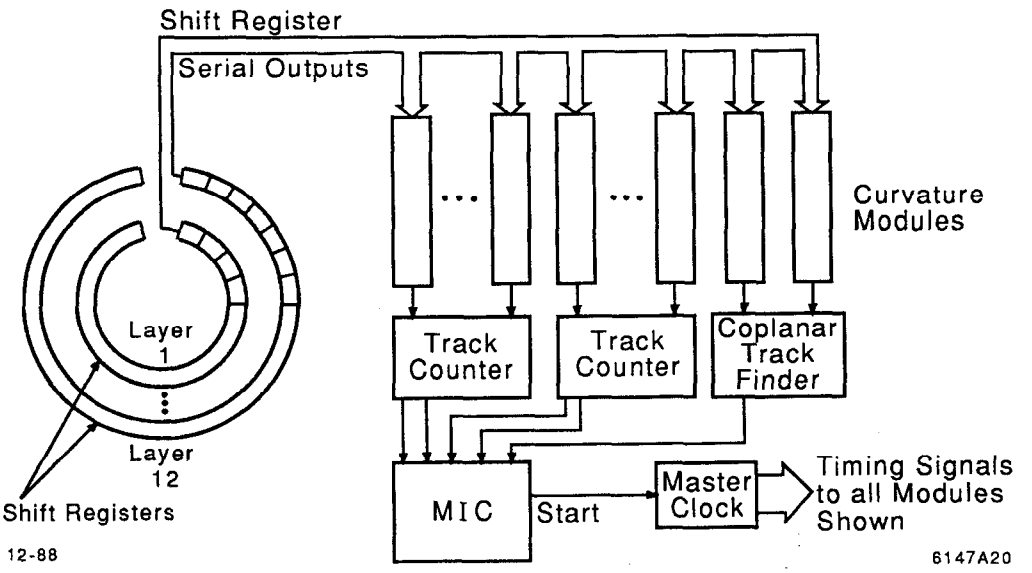

Figure 42 Structure of the charged track trigger. The list of hit cells in the CDC (left) was transferred to hardware curvature modules which matched it against predefined patterns which represent tracks.

Unlike at PEP, where a primary trigger was needed to reduce rate, the entire central drift chamber trigger and liquid argon calorimeter trigger examined each beam crossing. Separate timing was used to allow cosmic-ray data-taking between SLC beam crossings. Random beam crossings were also recorded during normal operation for background studies. Studies of the overlapping trigger components indicate that the trigger is approximately 99.8% efficient for events passing hadronic decay selection cuts.[47]

The data acquisition system is a hybrid of CAMAC and FASTBUS. The liquid argon calorimeter and muon systems were read out through BADCs similar to the ones used by the SSVD. BADC and other CAMAC data was read into the VAX computer in its entirety before the detector was enabled for another beam-crossing. This took typically 20 milliseconds, resulting in the loss of 3 beam crossings at 120Hz.

The CDC and DCVD system's FASTBUS information was processed in parallel with acquisition. The FASTBUS FADC and TDC data were read into SSP processors for pulse processing. The results were then recorded to tape by the Mark II VAX computer. Especially in the DCVD, this process could not keep up with

backgrounds observed in early running, and additional processors had to be added to the system.

2.3 The Monte Carlo Simulation

We must simulate the process by which Z^0 boson decay is recorded in our detector. This process has six steps:

1. The Z^0 decays into quarks. The probability of each type occurring and their angular distributions are given by electroweak theory calculations.
2. The quarks may radiate gluons and/or other quarks, which creates the jet structure of the event.
3. The quarks and gluons give rise to hadrons through a fragmentation process.
4. Weak interactions decay the long-lived hadrons, including the ones containing b quarks.
5. The resulting particles interact with the material of the Mark II detector, eventually producing electrical signals which are recorded by a computer.
6. The generated data is written to tape in a format which can be processed by the standard reconstruction code used on data tapes.

The first four steps are simulated using the JETSET 6.3 code,[48][49] commonly referred to as "Lund with parton-shower fragmentation".[50] This has been tuned at both PEP[51] and SLC[34] energies to faithfully recreate the data. Figure 43 through Figure 45 show the level of precision possible using the earlier sample of 538 Z^0 decays. Additionally, data from LEP experiments, where available in a suitable form, has been used to check the simulation's parameters.[24] The remaining uncertainty in some of these parameters will be discussed as systematic errors in Chapter 5.

The model used for the fragmentation process is flavor dependent. Hadrons containing heavy quarks such as the b quark are expected to contain a larger fraction of the event energy than hadrons containing only light quarks.[52] For the fragmentation of c and b quarks, it is customary to use a different formulation than the string fragmentation used for lighter quarks.[53] Experiments at LEP have investigated this form using semi-leptonic B hadron decays and find no disagreement.[26] A parameter sets the fraction of B hadrons that are baryons, with the default value being 10%.

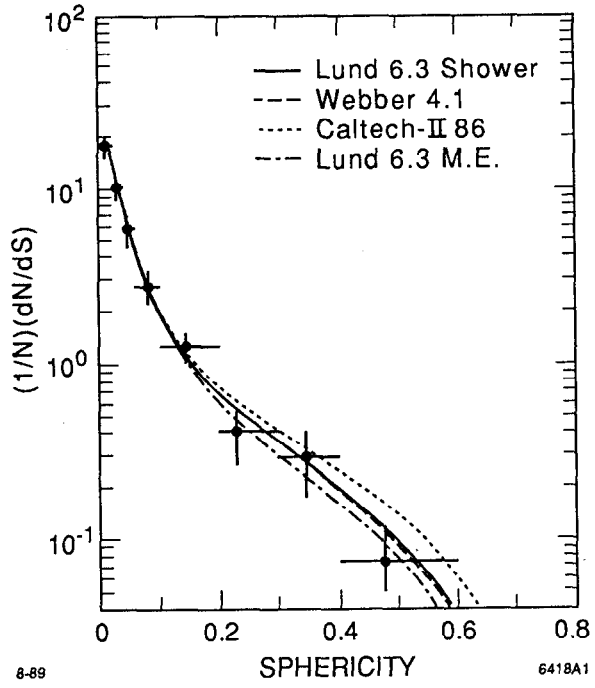

Figure 43 The distribution of event sphericity. The solid line is the result of the Mark II simulation.

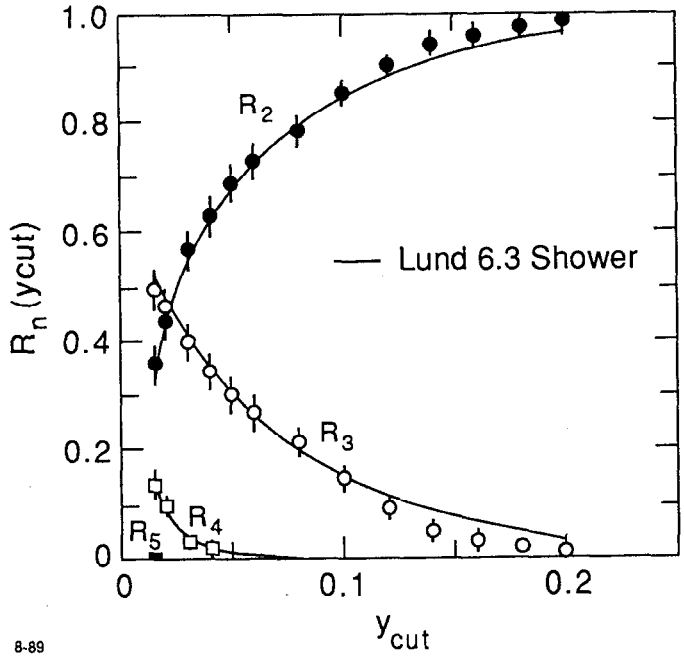

Figure 44 The distribution of jet multiplicities as a function of the separation parameter. The solid lines are the result of the Mark II simulation. Y_{cut} is an input parameter to the JADE jet clustering algorithm.[54]

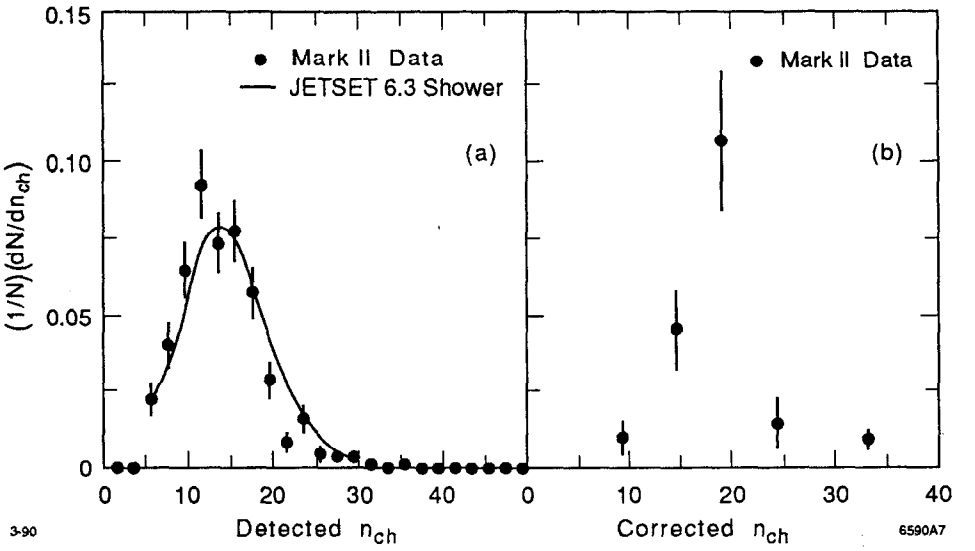

Figure 45 Charged multiplicity as observed in the Mark II and after correction for acceptance.

The decay of B hadrons is mediated by a simulated W boson. The spectator quark remaining from the B hadron is immediately combined with the c or u quark from the b quark W vertex to form a meson, with the W decay products then being passed through the same hadronization code as the original event. This process is tuned to recreate PEP and CLEO data on the decay properties of the B mesons.

The generated particles are passed through a simulation of the detector. The signals in each subsystem are generated using known resolutions and inefficiencies. Scattering in the material of the detector is included by varying the angle of the particle track as it passes through the material. The largest source is Coulomb scattering, which is modeled using a full Moliere distribution.* Since the angular smearing is done in layers of much less than 1% of a radiation length, the non-Gaussian tails on the distribution are important for obtaining both the correct core and tail in the total track scattering distribution (Figure 46). Elastic nuclear scattering is simulated using a P_T distribution and cross-sections evaluated in terms of "carbon-equivalent material", which should be accurate to the 10% level. Inelastic nuclear scattering is simulated as an entirely absorptive effect - the probability to inelastically scatter is determined at each layer, and a suitable fraction of particles are stopped there. No daughter particles are produced.

* The distribution is generated by the MLR subroutine in the CERNLIB library.

Approximately 1% of Monte Carlo charged tracks terminates in a nuclear scatter before the inner radius of the DCVD is reached.

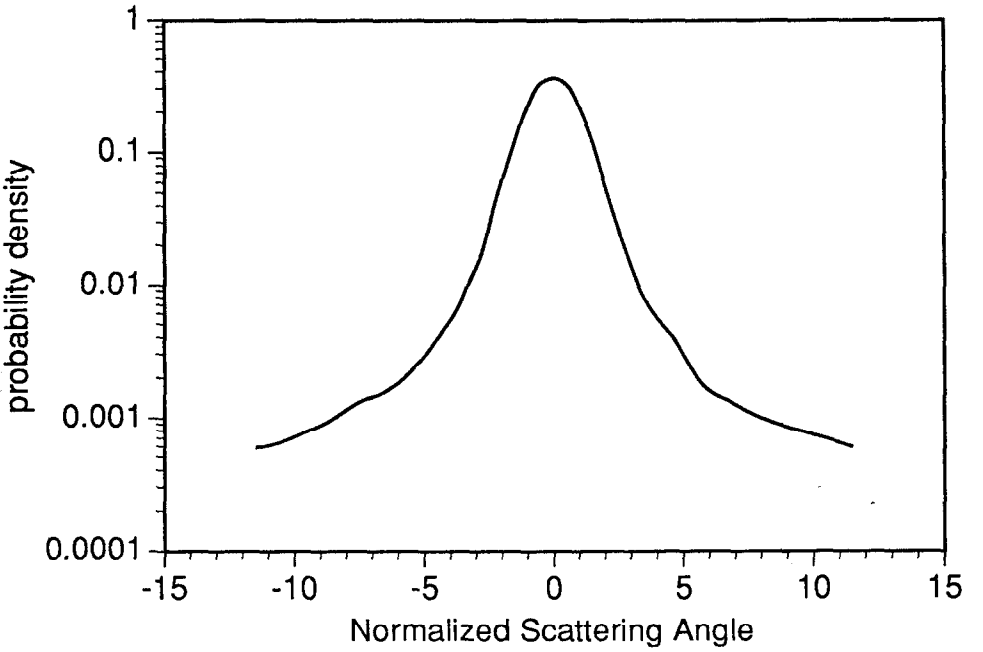

Figure 46 Typical Moliere distribution used for generating Coulomb scattering due to transiting a single Silicon Detector Module in the simulation. The horizontal axis has been normalized to the Particle Data Book approximation formula. The exact shape is a function of the material thickness.

We include the effect of beam-induced backgrounds by mixing the Monte Carlo simulation output with the data from actual background events. These were recorded on random beam crossings during the same time period as recorded Z^0 decays.

The reconstruction code used for the Monte Carlo simulation is the same as that used for the data. Constants such as wire positions, gains, etc., are maintained in separate files because numbers appropriate to the detector are specific to a certain time interval. In the case of the constants specifying the SSVD geometry, which are critical to the precision of the tracking, the values used for reconstruction are generated using Monte Carlo data and the same alignment process used for the actual detector. The accuracy of this process is discussed in Chapter 3.

It has long been an axiom of mine that the little things are infinitely the most important.

Arthur Conan Doyle

3 Precision Tracking Method

The track position measurements made by the three detectors of the tracking system must be processed to obtain tracking information. This processing includes deciding which hits should be taken together to form a track and then fitting the hits to a track hypothesis. The result is a set of values for the five track parameters and expected errors of those parameters, both of which are important for the physics measurement.

In this chapter we first discuss the sources of error in the track reconstruction. We then examine the fitting process in each tracking system. In the case of the SSVD, we also describe the process used to determine the positions of the individual detector modules, as the accuracy of this process is crucial to the SSVD's measurement accuracy. We finish by describing the algorithms used for reconstructing the position of the IP. Comparison of the tracking results for data and Monte Carlo simulation is done in Chapter 4.

3.1 Track Reconstruction Errors

There are two main sources of error in the parameters calculated for a track. The detector makes imperfect track position measurements outside the beam pipe. The best attainable resolution is limited by the precision of the individual measurements. At low momenta, a large additional effect comes from random fluctuations in the scattering that a charged particle undergoes while moving through matter. This adds to the uncertainty of the backward extrapolation of the charged particle's path from the measurement region to the IP.

In the remainder of this section we examine these two sources of error. An alternate, graphical explanation is given in Appendix A, and additional mathematical detail can be found in Appendix B.

3.1.1 Multiple Scattering

Coulomb scattering in a material layer changes the direction of a track in a probabilistic manner. Multiple scattering, the largest contribution, can be approximated[55] as a Gaussian distribution of width

$$\phi_{ms} \approx \frac{0.0136\sqrt{L}}{\beta P} f(L) \tag{13}$$

where L is the thickness of the material along the flight path in radiation lengths, P is the magnitude of the particle momentum in GeV/c and $f(L)$ is a function used to compensate for non-Gaussian tails (Figure 46 on page 47), which force ϕ_{ms} to scale differently from $\sqrt{L}$. f is often approximated by the form

$$f(x) \equiv 1 + \frac{\log(x)}{9}. \tag{14}$$

In a cylindrical geometry like that of the Mark II, this scattering degrades the tracking resolution at the IP by a term of the form

$$\frac{R}{\sin\theta} \times \phi_{ms} \approx \frac{R}{\sin\theta} \times \frac{0.0136\sqrt{L/(\sin\theta)}}{P} f(L/(\sin\theta)) \equiv \frac{\sigma_{ms}}{P_{scat}} \tag{15}$$

where R is the radius of the scattering layer and L is the nominal thickness of the layer, so that $L/(\sin\theta)$ is the thickness actually traversed by the particle. The $\sin\theta$ factors have been conveniently collected by defining

$$P_{scat} \equiv P \sin\theta^{3/2}. \tag{16}$$

We ignore the $\sin\theta$ in $f(L/(\sin\theta))$ as f is only logarithmic in its argument.

3.1.2 Intrinsic Tracking Resolution

In the Mark II, the resolutions of the individual track position measurements vary between less than 10 microns in the SSVD and greater than 250 microns in the CDC. This is an example of a tracking system with a 'vertex detector' backed up

by an 'outer tracker'. In a simplified model, the intrinsic tracking resolution of this system has two independent contributions

$$\sigma_I = \sqrt{\sigma_t^2 + R^2\sigma_\phi^2} \tag{17}$$

where σ_t is the resolution of the vertex detector's measurement* of the track's transverse position, σ_ϕ is the angular resolution achieved by the outer detector, and R is the radius of the vertex detector measurement. The two terms correspond to the uncertainty in the track position at the point where it is best measured (at the vertex detector measurement) and the uncertainty in projecting that position to the IP. Note that both these terms are independent of momentum, so this is still the intrinsic resolution.

3.1.3 Total Tracking Resolution

If scattering inside the tracking volume can be ignored, we can approximate the tracking resolution by combining the intrinsic and multiple scattering errors in quadrature as

$$\sigma_T \approx \sqrt{\sigma_I^2 + (\sigma_{ms}/P_{scat})^2}. \tag{18}$$

This is the traditional[56][57] formula for the momentum dependence of tracking resolution.

More realistic systems have more complex behavior because of details we have neglected above. The Mark II tracking system, with three sets of measurement points and significant material between them, has a much more complicated tracking resolution function (Figure 47). Although tracks receiving any combination of SSVD hits haven intrinsic tracking resolution of about 10 microns for high momentum tracks, the resolution at lower momenta depends on which SSVD layers provide the tracking information.

This is due to several factors. We have so far ignored the effect of material outside the first measurement layer. Although it's contribution to the multiple scattering term is not as large as material inside the first layer, it cannot be ignored. For tracks that only receive one SSVD measurement, the amount of material preceding and following the first measurement depends on which layer contains the first hit. This has the effect of increasing the multiple scattering term, and thus the slope in Figure 47, for single hits in the outer layers of the SSVD.

* If the vertex detector makes multiple measurements, we consider them combined into a single transverse measurement of higher precision.

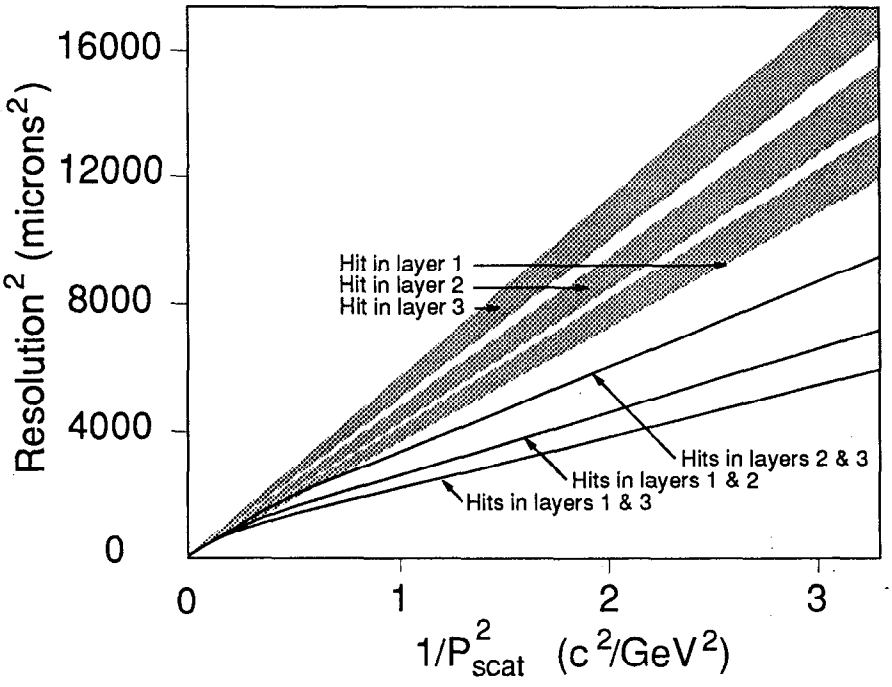

Figure 47 Calculated tracking resolution of the combined tracking system as a function of P_{scat}. The calculation uses a model of all layers of material in the tracking system. The labels indicate the SSVD layers that contributed measurements to the track fit.

For track momenta greater than about 3 GeV/c, this model also describes tracks with more than one SSVD measurement. For momenta less than about 3 GeV/c, another effect enters to improve the track resolution relative to the simple model prediction - the SSVD can measure the track angle. The DCVD and CDC measure the track angle outside the material of the SSVD, whose scattering limits their achievable accuracy. The SSVD is itself capable of measuring the track angle, but it's geometry is far from optimal. The SSVD has only 2 or 3 measurements and a maximum measurement length of 6 millimeters. This implies a σ_ϕ of one milliradian, corresponding to a contribution to the intrinsic resolution of 30 microns. Nevertheless, there is a track momentum below which the multiple scattering in the SSVD degrades the DCVD/CDC angular measurement so much that the SSVD makes a better measurement of the angle (Figure 48). This causes the track resolution function to improve. Different pairs of SSVD hits have different spacing, which causes different intrinsic contributions. Additionally, a track that is measured by SSVD layers 2 and 3 suffers from multiple scattering in layer 1, resulting in a larger slope, as seen in Figure 47.

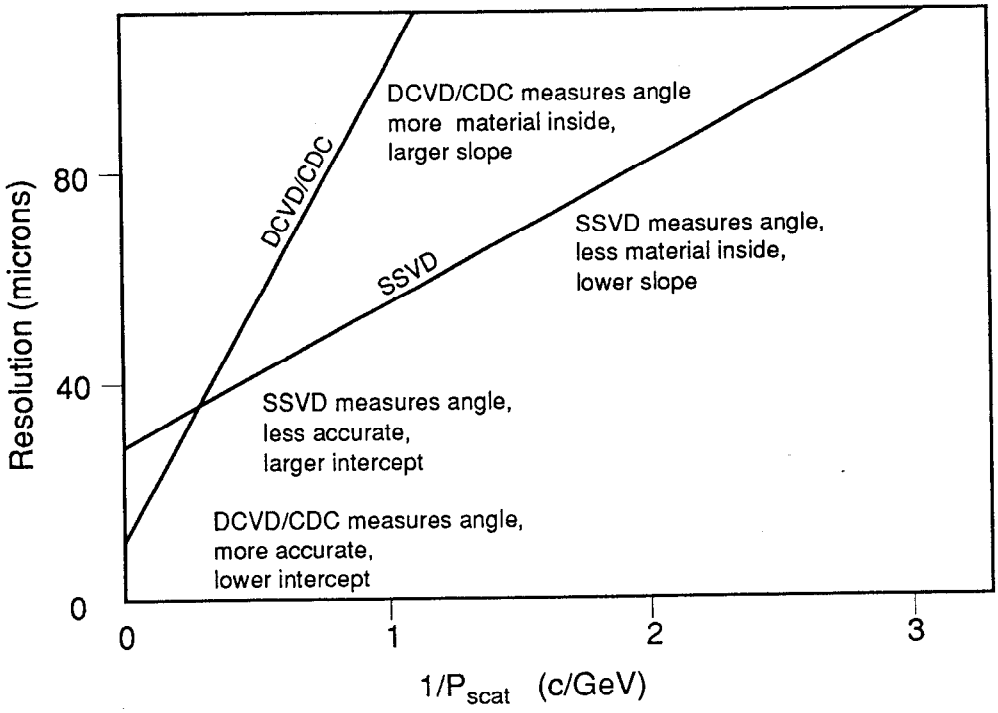

Figure 48 Model tracking resolution for two different track angle measurements.

This qualitative understanding is incorporated explicitly in the calculation of the impact parameter error during track reconstruction. The mathematics involved is described in some detail in Appendix B.

3.2 Track Reconstruction Overview

In outline, the Mark II track reconstruction is done sequentially in the CDC, DCVD and SSVD. In each step, hits are grouped onto tracks and then a fit is done to determine optimal values for the track parameters. Least-squares fitting techniques are extensively used during track reconstruction,[58][59][60] so we will first discuss some details of the fit process. We will then provide a short overview of the steps needed to reconstruct tracks.

3.2.1 General properties of least-squares fits

A least-squares fit is used to find 'optimal' values of a set of parameters. Formally, one typically starts by defining a variable

$$\chi^2 = \sum_{i=1}^{n} \frac{(x_i - f_i(V))^2}{w_i^2} \tag{19}$$

where V is a unknown (possibly multiple) variable, and the w_i and x_i are known or measured values. A least-squares fit then finds the value of V that minimizes χ^2.

This definition can be interpreted as involving n equations of the form

$$f_i(V) = x_i, \tag{20}$$

each of which expresses a condition that is nominally true, except for statistical errors. The w_i are then the relative weights applied to these equations, and the purpose of the least-squares fit is to find the 'best' value(s) for V such that these conditions are satisfied.

In the specific example of track fitting, the x_i would be the positions of hits in the i^{th} detector layer, V would be the track parameters, $f_i(V)$ would be the position the track is calculated to have in layer i given track parameters V, and w_i would be the measurement resolution of the i^{th} hit. Equation (20) then simply says "the track should go through this hit". A least-squares fit finds the set of track parameters (V) that does the best possible job of simultaneously going through all the hits.

A slightly more complex form is used when some of the quantities are correlated. In this form, both $f_i(V)$ and x_i are multiple-component vectors (in the linear algebra sense of the word). The n equations are each written as

$$(x_i - f_i(V))\, C_i^{-1} (x_i - f_i(V))^T = 0 \tag{21}$$

where C_i is the covariance matrix describing the variances and correlations of the elements of x_i.

Least-squares fits have a number of valuable properties. When errors are distributed according to a Gaussian distribution, it can be shown that least squares fitting is equivalent to the maximum likelihood method. Regardless of the error distribution, least-squares fits can be shown to be "un-biased", which formally states that in the case of a large number of repeated fits (on independent data), the mean result will be the true result. More importantly, with the correct choice of weights the Gauss-Markoff Theorem states that

> "... among the class of estimates which are unbiased estimates and which are linear functions of the data, the least squares estimate has the smallest possible error."[61]

The Gauss-Markoff theorem does not rely on any particular probability distributions, so Gaussian errors are not required. It just requires that the weights w_i be proportional solely to the standard deviation (root-mean-square about the mean) of the individual x_i values.

In addition to the values of V, a least-squares fit generates a covariance matrix C' containing the expected variance and correlations of the elements of V. C' is calculated from the weights w_i or C_i, and is generally much more sensitive to their value than is V.

It is often the case that the distribution of the individual x_i contains a sizable Gaussian 'core', with additional non-Gaussian 'tails' (Figure 49). Under most circumstances, the Central Limit Theorem of statistics implies that distributions become more Gaussian as they are combined. So long as they are not highly correlated, the tails in the individual distributions of hit positions will tend to average out when 32 (DCVD) or 72 (CDC) hits are combined to calculate the position of a single track. In cases like this, it is important to avoid using for the weight an indicator, such as the width of a Gaussian fit, which does not capture the variance of the entire distribution.

The best value of χ^2 found by the fit obeys a well-defined distribution[62] and is often taken as an indicator of the fit quality. Specifically, when fitting for m parameters using n pieces of information, χ^2 obeys the 'χ^2 distribution with n–m degrees of freedom (DoF)'.

3.3 CDC Tracking

The algorithms for finding[35] and fitting[58] tracks in the Central Drift Chamber have been described in detail elsewhere. Briefly, track segments are found in each cell. The segments found in the axial layers are combined into tracks by grouping segments consistent with the same values of track ϕ and curvature. Segments in stereo layers are then added by the same matching procedure using z and $tan\theta$ as variables. Ambiguities at each level are resolved by doing a simplified fit for the track parameters and retaining the assignment that gives the smallest total χ^2.

As a final step, the hits and approximate track parameters are used as input for a piece-wise-helical fit program (SARCS6) which takes dE/dx energy loss and non-

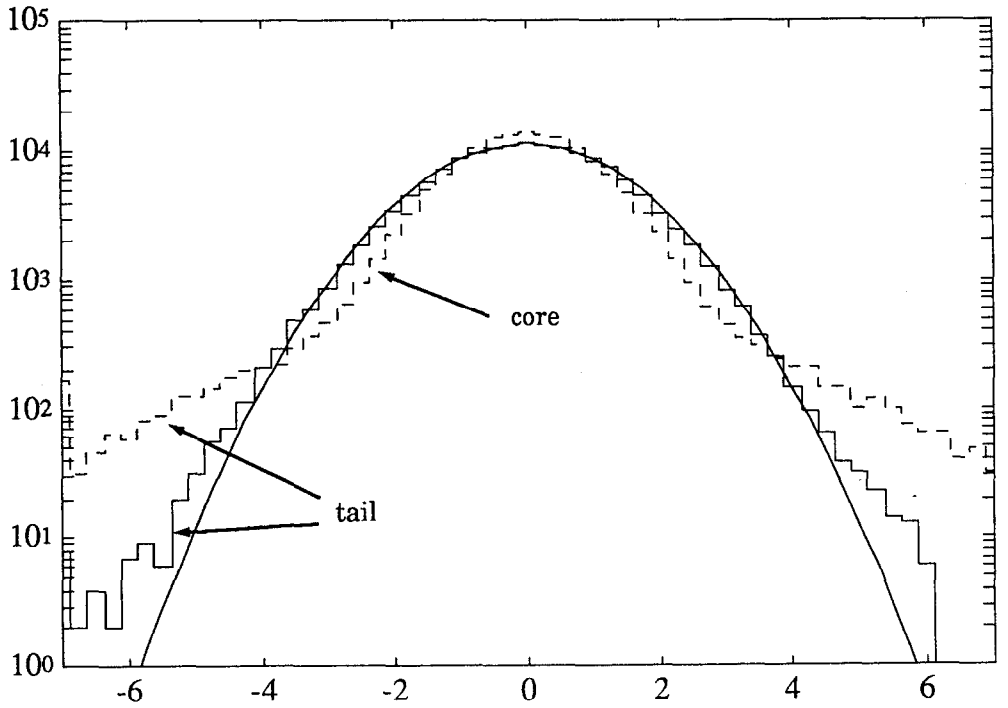

Figure 49 Several sample distributions. The solid curve is a true Gaussian of width 1.35. The dashed bar plot is a Gaussian with a unit-width 'core' and wide 'tail', resulting in a standard deviation of 1.35. The solid bar plot is the result of combining 16 samples of the dashed distribution, and also has standard deviation of 1.35.

uniform magnetic field into account. The effect of multiple scattering in the gas and wires of the CDC is included by inflating the covariance matrix which results from the fit according to the formalism of Gluckstern.[63]

3.4 DCVD Tracking

After track finding and fitting in the CDC, the DCVD is independently searched* for hits that form track segments. The search is done by a software procedure similar to the hardware 'curvature modules' of the trigger, where preset patterns of locations in the chamber are checked for a sufficient number of hits present. The patterns are chosen to be fully efficient for tracks passing within 4 mm of the origin in the xy plane and having $p_{xy} > 250$ MeV. Hits that appear in more

* The DCVD hit finding is done by the NEWADDVX subroutine, developed by Don Fujino.

than one track segment are assigned to the segment that already contains the larger number of hits. Hits are then added and subtracted from the segments in a 'polishing' process while fitting the segment to an arc of a circle in the xy plane.

Next the collection of polished segments is compared to tracks found and fit in the CDC. Hits from a segment that is a sufficiently close match in position and angle to a CDC track are assigned to the track. Only one segment can contribute DCVD hits to a track. Segments that do not match are discarded and their hits are marked as unused.

Tracks found in the CDC which have not been assigned any DCVD hits are next directly extrapolated into the DCVD. At each DCVD layer, the nearest unused hit is assigned if it passes a χ^2 cut. This process is not used for all DCVD hit matching because it has a higher probability of confusing the hits from closely spaced tracks. It is efficient at assigning hits to those low momentum tracks that the prior algorithm did not find as segments.

The SARCS6 fitter is then used to generate new track parameters and a covariance matrix from the entire set of DCVD and CDC hits assigned to the track. Multiple scattering in the wall between the CDC and DCVD is explicitly included in the fit by allowing a kink angle as a additional (sixth) fit parameter. Scattering in the gas and wires is again added to the results of the fit using the Gluckstern formalism. The formalism does not explicitly allow for nonuniform wire spacing or resolution, but Monte Carlo studies indicate that this is not a significant effect in a chamber with a large number of wires.

Figure 50 shows the distribution of χ^2/DoF for the data and Monte Carlo. The data is slightly broader than the Monte Carlo prediction, but the agreement is satisfactory.

3.5 SSVD Tracking

SSVD tracking starts with the positions of track crossings found in the SSVD by the clustering algorithms (Section 2.2.3). Tracks that have already been found and fit in the outer chambers are then compared to different combinations of clusters, and the best match determines which clusters are assigned to the tracks. A final fit is then performed to get the track parameter values.

3.5.1 Hit Finding

Trial and error is used to match SSVD clusters onto tracks found in the DCVD and CDC. The combinatorics of this is quite manageable, as there are at most three

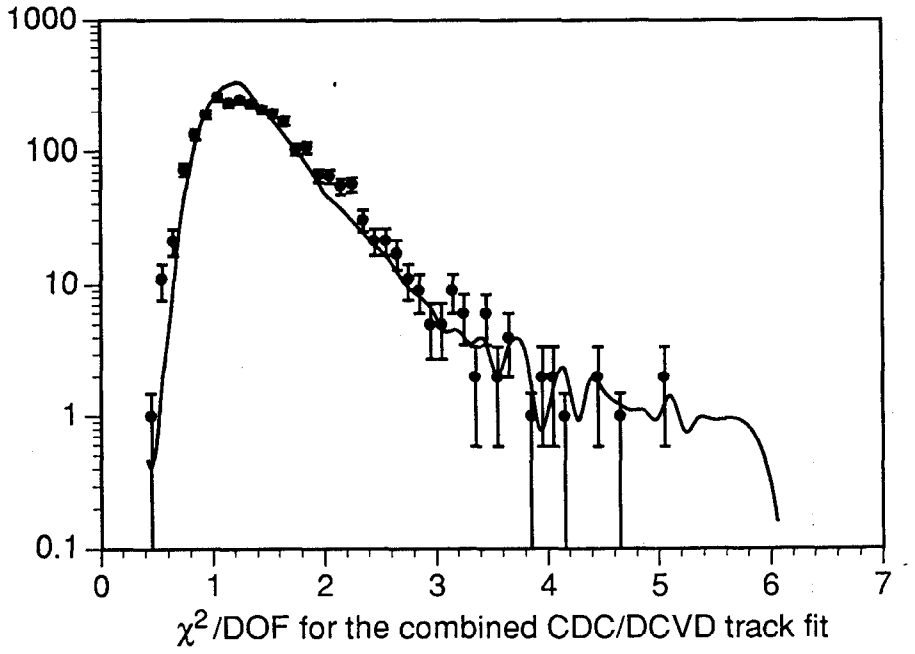

Figure 50 The χ^2 per degree of freedom for the track fit in the CDC and DCVD. The Monte Carlo prediction (curve) and data (points) disagree near a χ^2/DOF of 1.5, but the overall agreement is good.

SSVD layers to consider and the roads that must be searched are only about a millimeter wide. Each combination of clusters within the road is used to tentatively refit the track. Clusters that contain one or more strips which are marked as bad are not used.

The final set of hits is selected on the basis of best χ^2 from the track fit. Fits using three, two and one hit(s) have three, two and one degree(s) of freedom, respectively. The set of three clusters with the lowest χ^2 is used so long as the χ^2 is below 15. If there is no such set of three, the pair with the best χ^2 is retained, but only if it's less than 10. If no acceptable pairs or triplets are found, a single cluster found with χ^2 less than 5 is retained. Clusters may not be attributed to more than one track - in case of ambiguity, the track with the higher momentum is assigned the cluster.

The distributions of χ^2 are shown in Figure 51 for the case of one, two or three assigned SSVD hits. The agreement between data and Monte Carlo is quite good for tracks receiving one or two SSVD hits, but is slightly worse for tracks receiving three hits. The agreement for one and two hits indicates that the SSVD and outer

trackers are correctly aligned, although this is not a very sensitive measure. The internal alignment of the SSVD modules is a large contribution to the χ^2 for tracks receiving three SSVD hits and, as described below, it is not precisely known.

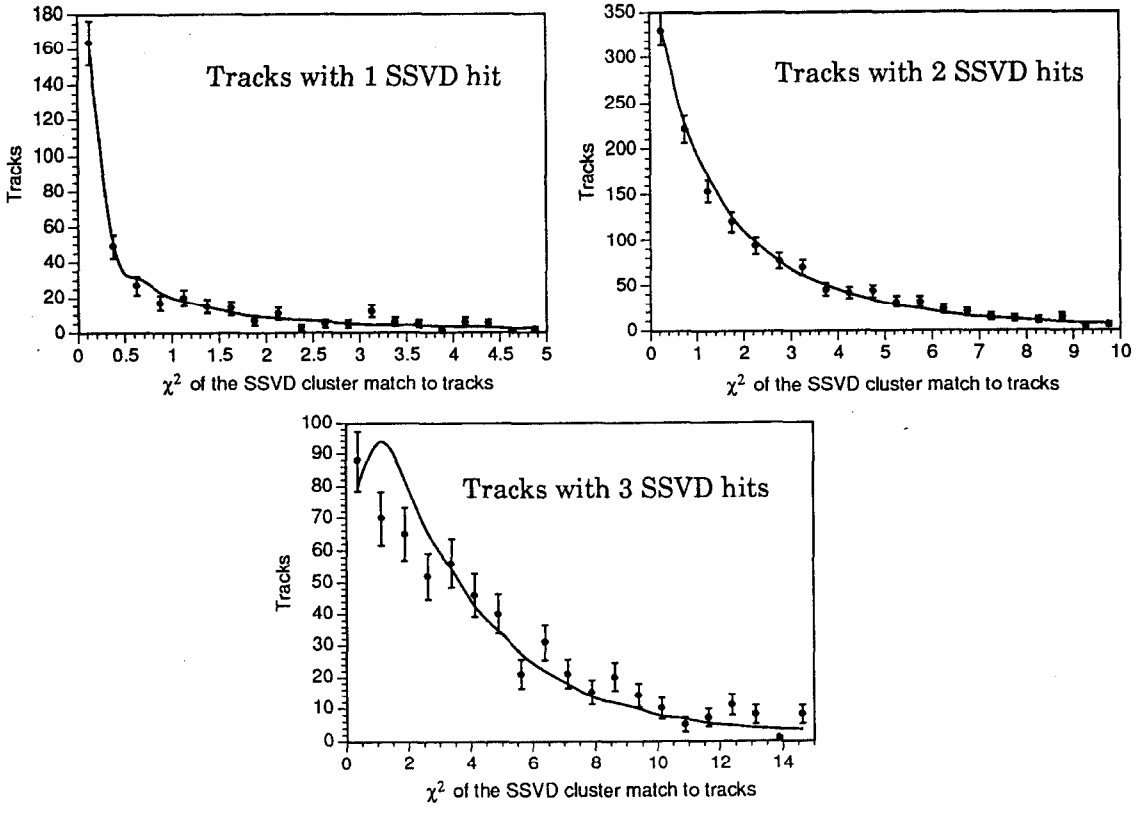

Figure 51 χ^2 of matching SSVD hits onto tracks. The points are data and curves are Monte Carlo predictions. See text for discussion.

The value of the χ^2 cut must balance tracking efficiency with quality. A theoretical χ^2 distribution using correct resolutions would erroneously reject 2.5% of single-hit fits, 0.7% of double-hit fits and 0.2% of triple-hit fits. The presence of clusters damaged by background, gaps in the SSVD coverage due to bad channels, and poorly measured tracks from the outer chambers complicates the calculation of how many hits should typically be matched. A Monte Carlo simulation, taking into account background, bad strips and outer chamber tracking, shows agreement with the data (Table 3). Approximately 6% of tracks found in the outer chambers cannot be matched to SSVD clusters. Study of corresponding tracks in the Monte Carlo simulation indicates these include tracks with several hits missing due to bad

channels or corrupted hits due to background, spuriously found tracks and tracks from photon conversions.

	data	simulation
1 hit	17±3%	15%
2 hits	58±2%	59%
3 hits	26±3%	26%

Table 3 Fraction of tracks assigned 1, 2 or 3 SSVD hits. The data does not sum to 100% due to rounding.

3.5.2 Track Fitting

Track parameters from the DCVD and the CDC are combined with SSVD hits using a least-squares fit. The process is described in detail in Appendix B. The inputs to the fit are the 5 track parameters from the outer chambers, plus the transverse position of the 1 to 3 selected SSVD hits. A total covariance matrix is formed from the 5x5 covariance matrix provided by the outer track fit, plus the assumed SSVD measurement resolution. Multiple scattering terms are added for each material layer between the first SSVD layer and the DCVD inner wires. These correlate the SSVD hits to each other and to the outer chamber track parameters (see "The Mathematics of Precision Tracking" on page 137). Standard least-squares fit techniques then are used to calculate the best track parameters and a new track parameter covariance matrix. Because of the strip geometry, the fit has little effect on the z intercept, dip angle and momentum track parameters, although they are allowed to vary.

3.6 SSVD alignment

Although each of the 35 SDMs in the SSVD is characterized by 8 geometric constants, it is convenient to parameterize these in terms of 6 global alignment constants for each of the two SSVD halves, plus 7 local alignment constants for each SDM.

The global constants are just the 6 positions and angles of a rigid body $\overline{d_X}$, $\overline{d_Y}$,$\overline{d_Z}$,$\overline{\alpha_X}$, $\overline{\alpha_Y}$, and $\overline{\alpha_Z}$, where the bar indicates global alignment values. These quantities are specified in the Mark II coordinate system, in which y is up and z is along the electron beam direction of travel (Figure 23). $\overline{d_X}$, $\overline{d_Y}$ and $\overline{d_Z}$ are translations along the positive x, y and z axes respectively, while $\overline{\alpha_X}$, $\overline{\alpha_Y}$ and $\overline{\alpha_Z}$ are right-handed rotations around those axes. Global alignment is used to set these

constants so as to position a rigid-body SSVD with respect to the outer tracking chambers. Three sets of constants are used to compensate for the motions of the SSVD described with the CDM above.

The seven local constants for each SDM are the bow and twist shape parameters, plus five displacements and rotations d_X, d_Y, α_X, α_Y, and α_Z from the design module position. These are specified in a local coordinate system which varies from module to module (Figure 52). In it, the z axis is parallel to the axis of the SSVD assembly, y is radially outward from the nominal design position and x is across the surface of the SDM.

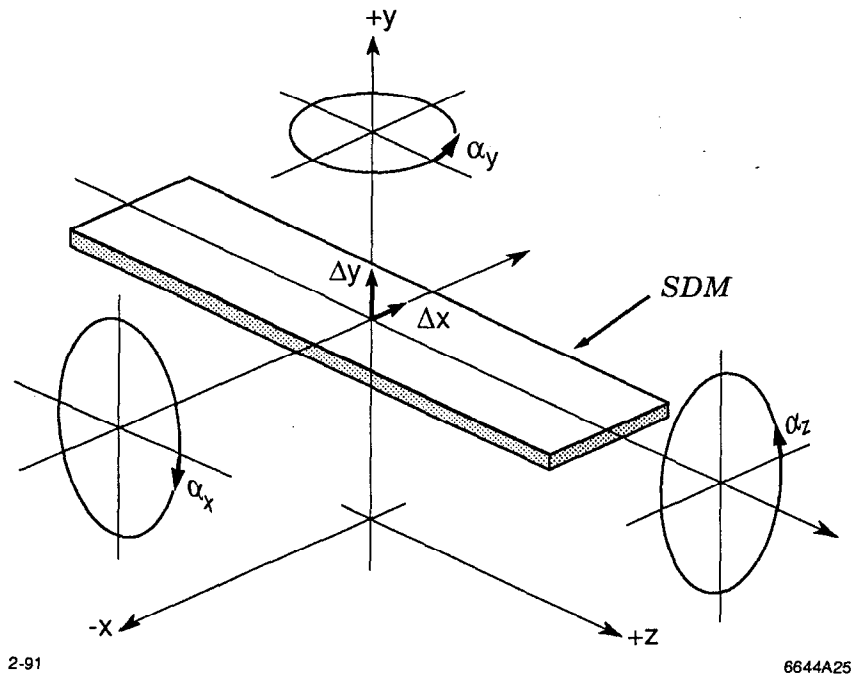

Figure 52 The local alignment coordinate system.

Note that there is no local d_Z constant. The detector strips are so parallel that Z translation of the detector strips corresponds to a choice of where the other parameters are specified. The global $\overline{d_Z}$ serves to specify the ends of the active region of the detectors.

Both X-ray[64] and optical[65] alignments were performed on the SSVD before it was installed in the Mark II, so a global alignment to survey the SSVD with respect to the Mark II coordinate system was expected to be sufficient. When tracks became available it was apparent that these alignments* did not position the SDMs to the

* The X-ray alignment, empirically corrected by a 50 micron increase in radius for each SDM, was used for the early look at the data. The optical alignment information has not been extensively used.

needed accuracy with respect to each other, as will be shown below. It is not known whether this is due to problems with the previous alignments or due to motions of the SDMs during the installation of the SSVD assembly in the Mark II. The only available solution was to do both global and local alignment using tracks.

3.6.1 Use of the CDM

The Capacitive Displacement Measurement system functioned well for the summer run. Except for two discontinuities, it provided a continuous readout. One of the discontinuities was between the end of the January running and the beginning of the summer running, where the long time span and system modifications prevent us from accurately comparing positions. The other discontinuity was on October 20^{th}, 1990 when a number of motions and system changes were made simultaneously. We consider the zero reference of the CDM data to be reset at the beginning of the run and before each of these discontinuities. Since the detector motions seen by the CDM were found to be below the sensitivity of the global alignment procedure, the run-to-run CDM offsets were used and the global alignment was partitioned to generate a set of global constants for each CDM zero.

3.6.2 The global alignment technique

Alignment is done with a least-squares fit using as input the observed distances between tracks fit in the outer chambers and their hits in the SSVD. Because hits must be selected by the track matching, which uses the SSVD alignment, the procedure is iterative. The excellent cluster separation in the SSVD and the tracking precision of the DCVD, especially at the 30 mm radius of the SSVD, guarantee that the process converges quickly.

For use in alignment, a track was required to pass geometric acceptance and $P_{xy} > 500\text{MeV/c}$ cuts. At least 15 DCVD hits, 25 CDC hits and 2 SSVD hits were required. There were 2100 acceptable tracks and approximately a third of them had three SSVD hits.

We proceed by transforming to new variables

$$\Delta_{b12} \equiv \frac{(x_1 + x_2)}{2}, \Delta_{b13} \equiv \frac{(x_1 + x_3)}{2}, \Delta_{b23} \equiv \frac{(x_2 + x_3)}{2}, \Delta_{b123} \equiv \frac{(x_1 + x_2 + x_3)}{3}, \quad (22)$$

$$\Delta_{\phi 12} \equiv x_1 - x_2, \Delta_{\phi 23} \equiv x_2 - x_3, \Delta_{\phi 13} \equiv \Delta_{\phi 123} \equiv x_1 - x_3, \quad (23)$$

and for tracks with three hits

$$\Delta_{\Delta} \equiv \frac{x_1 + x_3}{2} - x_2, \quad (24)$$

where x_n is the distance in layer n between the track as fit by the outer chambers and the assigned SSVD hit. Each track will have only one of the Δ_b variables and one of the Δ_ϕ variables defined, depending on which layers in the SSVD were hit (i.e. which of x_1, x_2 and x_3 are defined). The Δ_b variables emphasize the transverse distance between the track as fit by the outer chambers and as measured in the SSVD. Similarly, Δ_ϕ is the difference between the track angle as fit by the outer chambers and as measured by the SSVD. There is some correlation between the Δ_b and Δ_ϕ values for a given track, but we average over that in the fit. Δ_Δ is the distance that the three hits are acolinear, and is relatively insensitive to global alignment.

The Δ variables depend on the x_i, which are directly dependent on the SSVD hit positions and thus the alignment constants. Perfectly positioned SSVD hits and an exact track position would make all these variables zero. We fit to find the set of alignment constants that minimize the sum of the squares of the Δ variables.

Cuts are applied at approximately three standard deviations on each of these variables. Approximately 80 of 2100 tracks passing the earlier quality cuts were excluded by these criteria. The variables are weighted in the fit by the standard deviation observed in the data. Table 4 shows the applied cuts and contrasts the standard deviations seen in the Monte Carlo, the data after global alignment, and after local alignment. The Δ_ϕ and Δ_Δ variables are seen to contain more accurate information about *relative* module placement than is available from just the individual hits.

For global alignment, the $\overline{d_Z}$ variable is set by inspecting tracking efficiency as a function of where in z the track crosses the module. This is accurate to about 2 mm, which is sufficient given that we perform a local alignment. The other 10 global alignment constants are fit from the tracks in each of the three blocks of runs. The derivatives needed for the fit, such as $\partial x_i / \partial d_X$, are evaluated numerically.

Variable	Cut	S. D. data before local align	S. D. data after local align	S. D. Monte Carlo
x_i	250	81	77	69
$\Delta_{\phi 13}$	100	33	29	25
$\Delta_{\phi 12}$	100	28	21	19
Δ_{b13}	250	76	76	63
Δ_{b12}	250	79	78	65
Δ_{Δ}	100	22	9	9

Table 4 Cuts applied to typical alignment variables and standard deviations observed. The first data column is after global alignment but before local alignment. The second data column is after both global and local alignment. The Monte Carlo simulation column assumes perfect SSVD alignment.

About 15%, 35% and 50% of the tracks are in the January, early summer and late summer blocks, respectively. The fit finds a final χ^2/DOF value within about 0.1 of 1, which is expected given that observed standard deviations were used as weights.

3.6.3 The need for local alignment

The Δ_{Δ} variable is predominately sensitive to the local alignment of overlapping modules. Like triplet resolution in wire chambers, this 'triplet delta' is very sensitive to intrinsic resolution and local alignment. It also enters into the track matching, as it appears in the χ^2 when matching 3 hits onto a track. Since the SDMs are staggered around the SSVD, there are three different geometries for tracks crossing three layers (Figure 53). We number the regions for each of these sequentially in ϕ around the SSVD. Figure 54 shows that the mean Δ_{Δ} is noticeably offset in some of these regions. The RMS Δ_{Δ}, which the beam tests and Monte Carlo indicated should be about 9 microns, was 22 microns after global alignment.

Figure 54 shows an unsatisfactory alignment. Inspection of the plot shows that SDMs 2-4 and 2-5 have large radial displacements, but the situation is quite confused in regions 20 to 36, which correspond to the lower detector half. A local alignment was clearly required.

3.6.4 The local alignment procedure

For local alignment, the most significant constants are d_X, d_Y, and α_Y. Because all tracks of interest come from within 2 mm of the origin, α_Z has no real effect. The

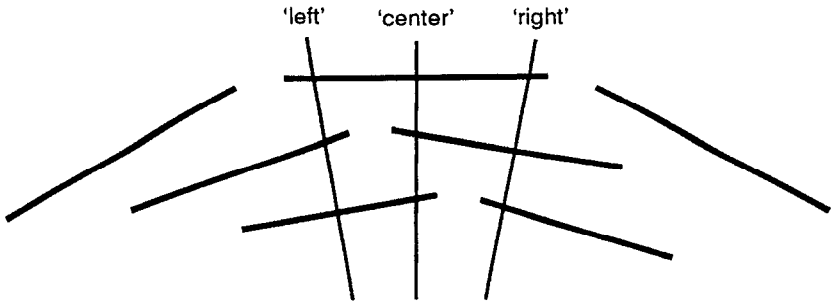

Figure 53 The three types of tracks which hit all SSVD layers. Note that radial misalignments effect each track differently.

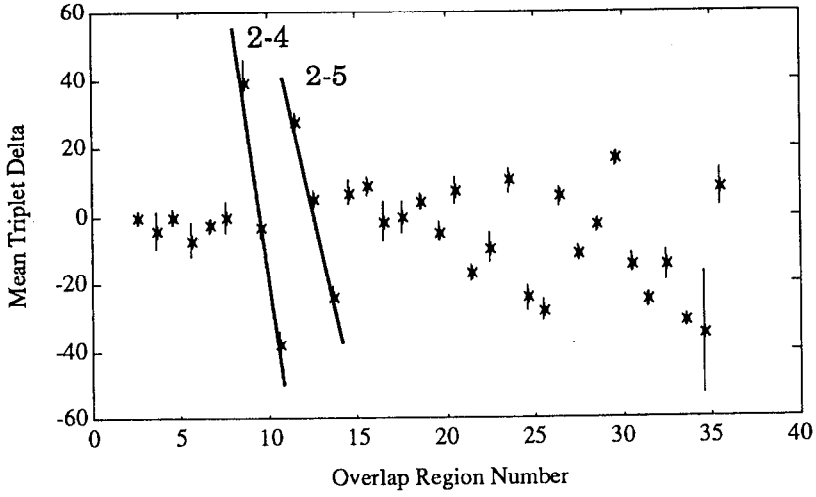

Figure 54 Triplet delta before local alignment. The horizontal axis is described in the text on page 64. The misplaced 2-4 and 2-5 modules are marked.

α_X constant is marginally significant - alignment statistics allow us to put only loose constraints on α_X, but that is equivalent to saying that tracking is not very sensitive to it. We do not include it in alignment except as a cross check.

Local alignment was done by using all 105 d_X, d_Y, and α_Y constants in a fit to all the tracks, using previously found global and CDM offsets to correct for any detector motions. Again the χ^2/DOF is within 0.1 of 1, indicating there are no significant, but unexpected, correlations in the data.

Based on the observed standard deviations, the fit calculates that local alignment will find d_X to 5 microns, d_Y to 25 microns and α_Z to 0.1 milliradian. Since an SDM is a precision rigid body extending over about 25° of ϕ, one would naively expect that local alignment would produce a relatively 'rigid' result which strongly constrains relative positions of modules. In reality, the correlations between modules are surprisingly weak. Typical correlation coefficients are 0.6 to 0.8 between maximally overlapping modules and 0.05 to 0.1 for adjacent modules in a layer. Modules neither adjacent nor overlapping were in all cases had correlation coefficients less than 0.02, which indicates that their alignment was for all practical purposes independent.

This can be understood in terms of the large number of alignment constants required. If the transverse positions of the SDMs were the only alignment constants permitted to vary, tracks extending through three modules would serve to rigidly pin the modules together as seen in Figure 55. The position of module A is coupled, with only about 4 microns of flexibility, to that of B which in turn is coupled to C, etc.

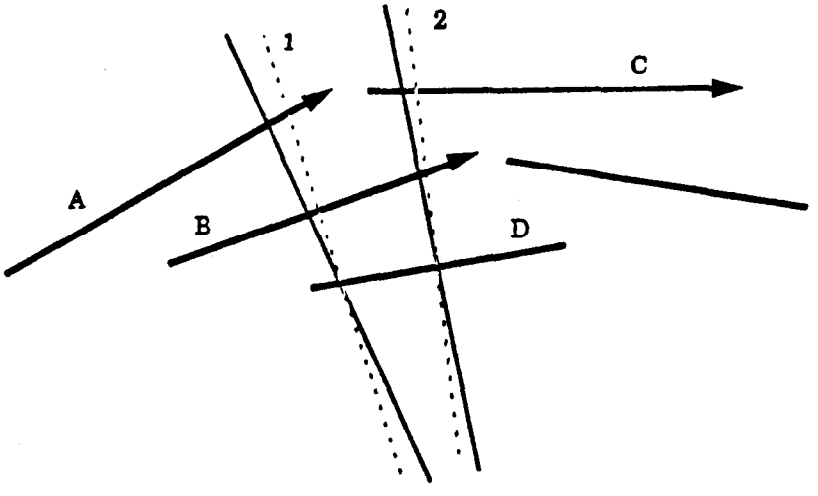

Figure 55 Modules pinned together, if only transverse motion is allowed. If module A is moved, module B moves to keep a hit on track 1. This moves a hit on track 2, resulting in module C moving. Motion of module D, neglected here, has the same result.

Permitting changes in radial alignment changes this. In Figure 55, module A is now coupled to a linear combination of the transverse and radial position of B. The alignment of A is completely decoupled from C, as B can match the motion of A by

translating along the direction of track 2 (shown by the arrow) without effecting the position of hits on the tracks passing through C.

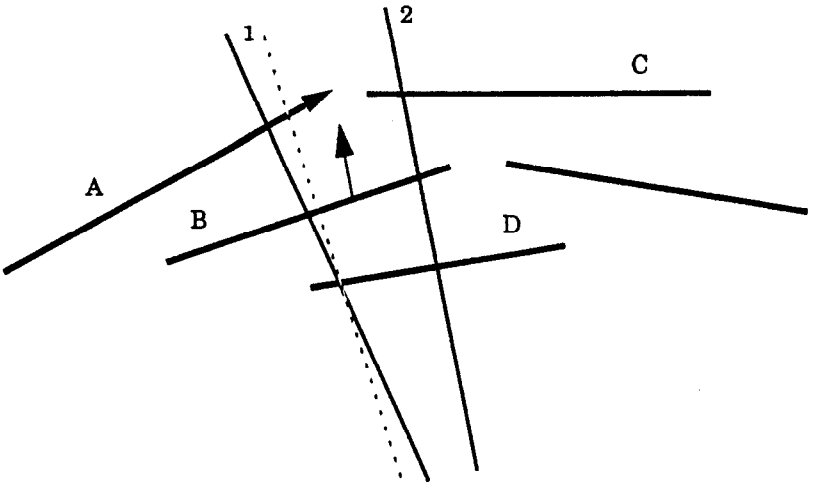

Figure 56 Modules no longer closely coupled due to radial degree of freedom. Motion of module A again moves the track 1 hit in module B, but module B now can move radially parallel to track 2. Neither C or D need move to keep hits on the tracks.

The real situation is complicated by the cylindrical geometry and the missing module(s) in layer 3, but the conclusion remains the same - alignment with tracks is a local operation.

After the local alignment, the Δ_{Δ} distribution is greatly improved. Figure 57 shows that the scatter has been held below 5 microns, which is satisfactory. Figure 58 shows the data distribution agrees quite well with the Monte Carlo. We see in Table 4 on page 64 that the angle and position, given by the $\Delta_{\phi xx}$ and Δ_{bxx} variables, remain marginally worse than expected from the Monte Carlo. The size of this discrepancy is consistent with the larger-than-expected cosmic miss distance (Section 2.2.2), so we attribute it to errors in the track parameters from the outer tracking chambers.

3.6.4.1 Division into subsamples and cross checks

Although statistics were limited, subsets of the data were checked for systematic alignment errors and motions. Separate global and local alignments using just the odd numbered and just the even numbered events gave consistent results. Separate local alignments using just the first half and just the second half of the data showed no indications that any of the SDMs moved locally during the running. Partitioning

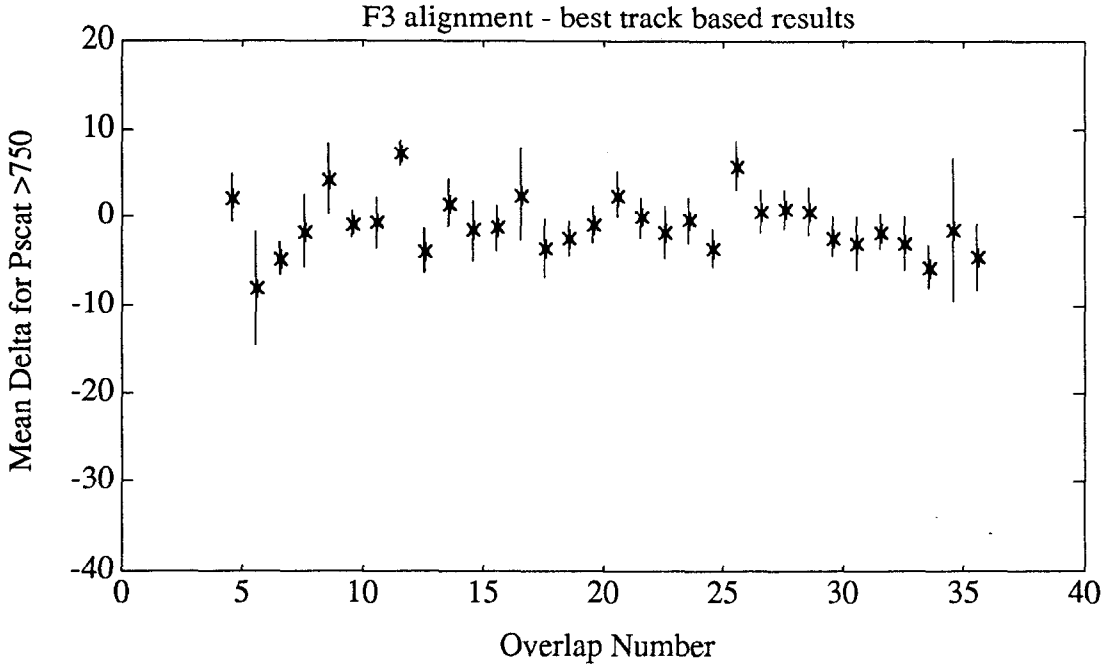

Figure 57 Triplet delta by geometric overlap region after local alignment. Compare to Figure 54, which has a coarser vertical scale.

the tracks into high momentum and low momentum subsamples showed no systematic difference.

3.6.5 Systematics

As we have seen, the SSVD alignment is free to adjust to possible large-scale systematic geometry defects in the outer chambers. Problems such as (un-expected) twists in the outer chambers would cause incorrect track positions at the SSVD, which the alignment procedure would erroneously 'correct' by moving the SSVD modules. This makes it extremely difficult to check for systematic errors by using internal (SSVD and outer chamber) alignment consistency. Significant effort was expended on removing this type of effect in the outer chambers, both during construction and after installation, so as to have a properly aligned system.

The SSVD alignment cannot completely adapt to defects on a smaller angular scale. Each SDM extends across a 30° region of ϕ, so systematic measurement errors that vary at or below this scale should survive the alignment and be visible.

In an aligned detector without systematic measurement errors, the mean of the distance between tracks as measured in the outer chambers and the SSVD hits they

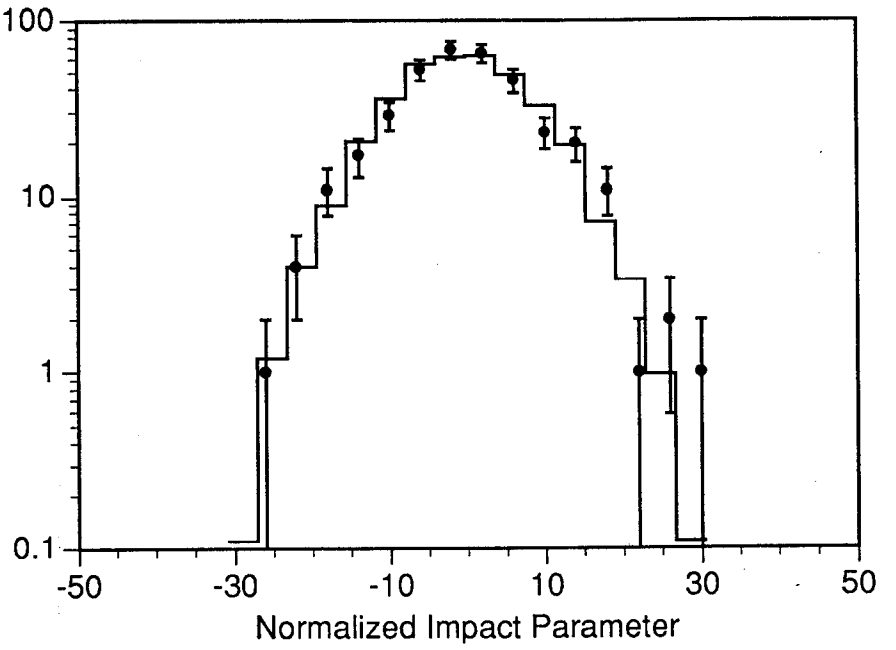

Figure 58 The triplet delta distribution after alignment. The solid curve is the Monte Carlo prediction. The 350 tracks included have $P_{scat} \geq 1$ GeV/c to reduce increased width due to multiple scattering.

match (x_i in the alignment procedure) will be zero. For all tracks taken together, the alignment process forces the mean x_i to zero. Examining the mean x_i versus another variable such as z would be expected to show misalignments if present. The only significant variation from zero mean was found when displaying the data as a function of the angular position within each DCVD cell (Figure 59). Due to the simple cell structure of the DCVD, this is highly correlated with both drift distance and the angle between the track direction and the drift direction. Corrections are already applied for both of these effects, but it is believed that the track angle correction may be underestimated. This systematic has not been corrected in the tracking.

This systematic effect is visible because it is confined to a single SSVD module. Figure 60 shows that the individual SDMs extend across at least half of a DCVD cell, so the local alignment is unable to position a rigid body SDM so as to remove the effect in Figure 59.

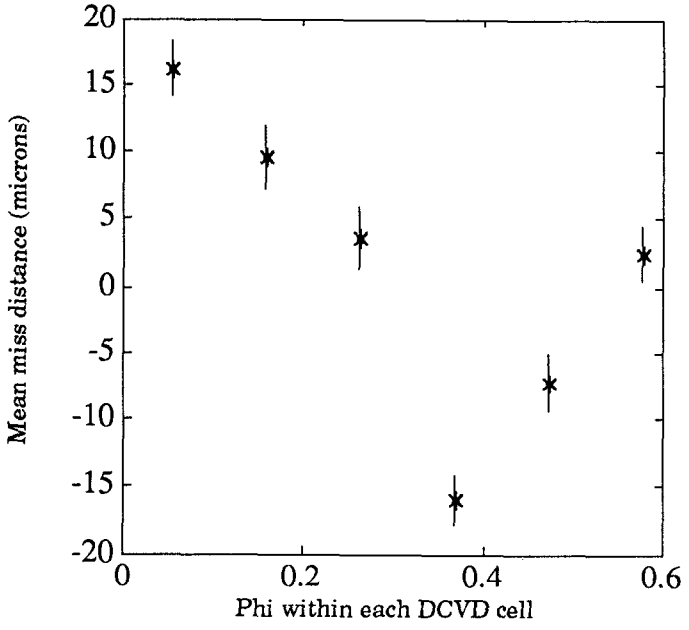

Figure 59 Mean distance tracks in the outer chambers miss their hits in the SSVD before refitting, as a function of angular position within a DCVD cell. The nonzero values are the signature of a systematic position error.

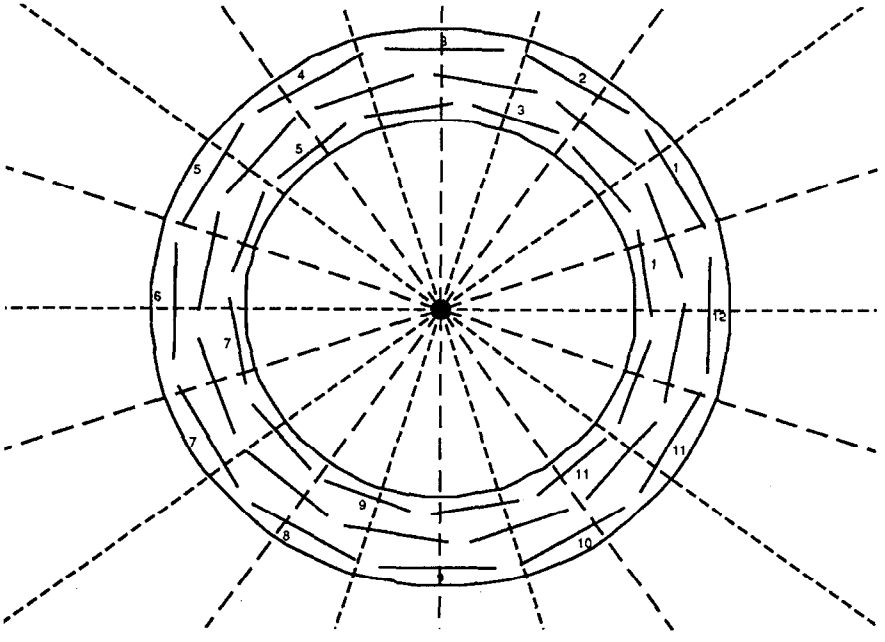

Figure 60 SSVD modules versus DCVD half cells. The two types of dashed lines separate left and right halves of DCVD cells.

3.7 Monte Carlo Verification

We use the Monte Carlo to check for errors in the tracking algorithms, using our knowledge of the correct values of the track parameters and which tracks have been effected by particle decays and other kinks.

We select tracks that we expect we can track well. The cuts are:

1. The track originates at a Monte Carlo vertex within 1 mm of the IP.
2. The tracked particle does not decay or radiate a photon within the detector.
3. The track passes geometric acceptance cuts of $|\cos\theta| \leq 0.8$, closest approach to the origin in z less than 10 mm and closest approach in the $r\phi$ plane less than 2 mm.
4. The track is found in the outer tracking chambers, defined as at least 15 of 32 possible hits in the DCVD and at least 25 of 72 possible hits in the CDC.
5. The multiple scattering is acceptable, defined as $P_{scat} > 150$ MeV/c.

Background mixing is used to simulate the correct tracking conditions. The SSVD alignment is exact. These studies were done using a Gaussian approximation for generating the Coulomb scattering so that the expected resolution would be exactly Gaussian.

Comparing the error between the fit track parameters and the known origin of the track, we see in Figure 61 that the core distribution is a unit Gaussian, but there are noticeable non-Gaussian tails. We expect that most of the tails are due to fitting the wrong hypothesis - the algorithm fits the track to one or more wrong SSVD clusters. Figure 62 shows that this is in fact the case - if we examine only tracks with no incorrectly associated SSVD hits, the resolution is overwhelmingly Gaussian. This indicates that the fitting code is performing properly. Most of the incorrectly associated hits are due to the algorithm picking up a background hit(s) in either the SSVD or the inner layers of the DCVD.

3.8 IP Finding

We need a method to define an IP in each event. We can either use an IP found directly in each event when computing impact parameters, or we can combine tracks from several consecutive events with the SLC beam position information to calculate a 'mean IP' with better statistics.

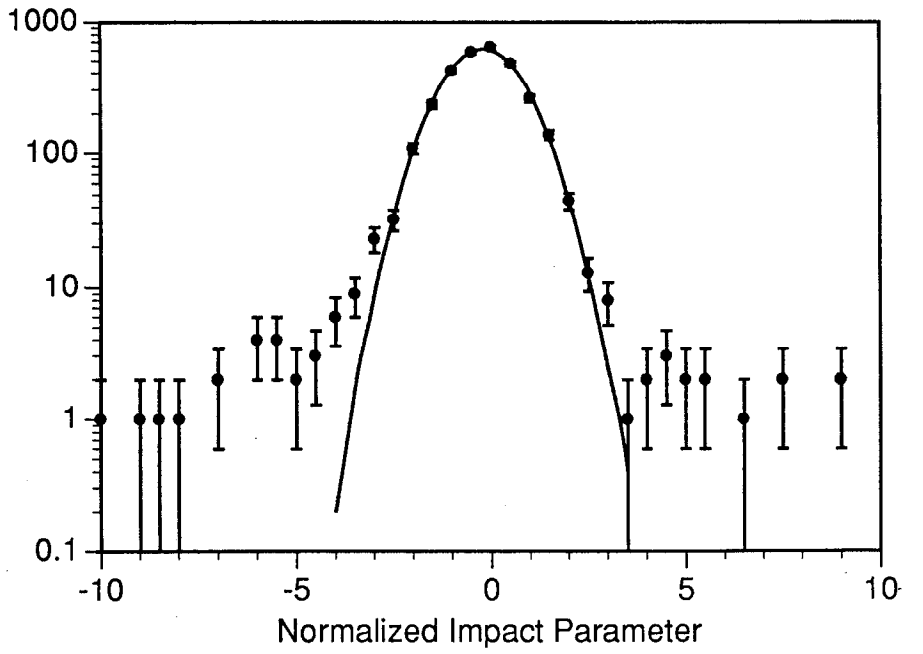

Figure 61 Monte Carlo impact parameter resolution. See text for details of track selection. Unlike Figure 62, this plot includes some tracks with incorrect SSVD hit assignments.

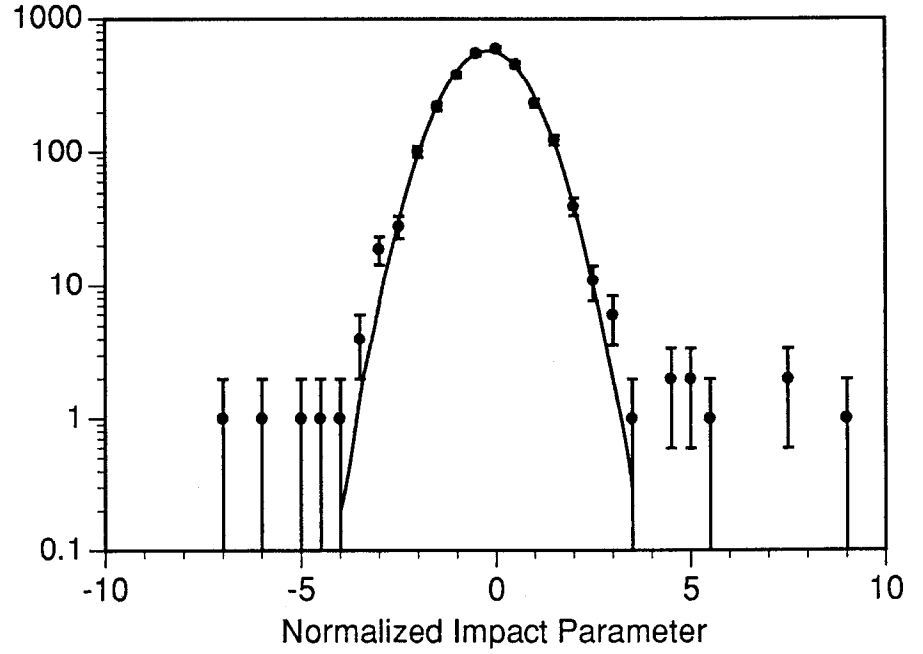

Figure 62 Monte Carlo impact parameter resolution. See text for details of track selection. Unlike Figure 61, this plot does not include tracks with incorrect SSVD hit assignments.

To find a mean IP in a group of events, we start by correcting each track position for relative beam motion predicted from the SLC steering magnets. This gives us a set of track angles and impact parameters in a consistent coordinate system. We fit all those tracks in the *xy* plane to find a single best vertex, and then correct back for the predicted beam motions (previously applied to the tracks) to get an IP position in each event. Although some of these tracks will come from secondary vertices not near the IP, this procedure introduces no bias on average.

We find an IP in a single event by building it up from a starting point,* the mean IP position for that event. We take the 4 tracks that pass closest to the starting point. All vertex fitting is done only in the *xy* plane. If the closest three form a vertex with greater than 1% probability, we keep that vertex. If not, we try each of the other three combinations of these tracks looking for a vertex probability greater than 1%. The Monte Carlo predicts that approximately 0.2% of events will not contain an acceptable initial vertex, in which case vertex finding fails. These events are typically *b* quark or *c* quark events in which there are few tracks from the primary vertex and the heavy quark mesons decayed far from the IP with few tracks consistent with the original IP. Vertex finding did not fail in our data sample.

We then try to add each remaining track to the vertex. If the largest probability is greater than 1%, we keep that track permanently in the new vertex. We iterate this process until no more tracks can be found that pass the 1% probability cut when added to the vertex.

The final collection of assigned tracks is fit to a common vertex to provide a position and error ellipse for the IP. The error ellipse is calculated from the covariance matrix of the individual tracks. Figure 63 shows the Monte Carlo distribution of the error in the IP position, in the direction of the minor axis of the covariance ellipse, normalized by the expected error from the vertex fit. The minor axis direction is chosen because it is by definition the best measured, thus the most sensitive to problems with the algorithm. Track resolution in this study has been smeared to agree with the data as described in Chapter 4, which significantly increases the size of the non-Gaussian tail in the resolution function from that seen in Figure 61.

For Monte Carlo *uds* quark events, where a single primary vertex is a reasonable model, the algorithm performs noticeably better than for events

---

* The algorithm was developed and tested by Steve Wagner. It can be found in the Mark II software library as VTXUP, a replacement for the older PRIVTX.

containing *b* quarks. Events with *b* quarks do not always have an unambiguous primary, and the error in the IP location is not well described by the error ellipse. Events where the Z^0 decayed to *c* quarks are intermediate in accuracy. Table 5 quantifies this by listing the results of a Gaussian fit to the error and the standard deviation of the error.

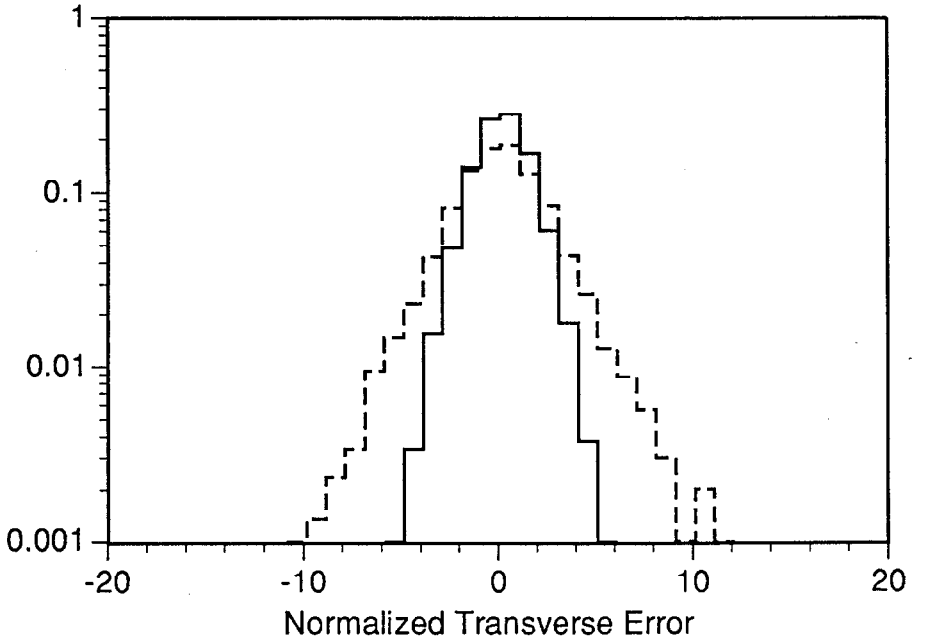

Figure 63 Normalized IP position error along the covariance ellipse minor axis. The solid line is events with only *uds* quarks. The dashed line is events containing *b* quarks. Events with c quarks are intermediate between these.

Even in *udsc* events, the error ellipse underestimates the IP scatter. Most of the discrepancy comes from the improper assumption of a pure Gaussian distribution for the resolution of the individual track measurements. The presence of non-Gaussian tails in the resolution means that some fraction of tracks, and thus the vertices they are included in, are farther from the IP than the resolution calculation predicts using errors appropriate for the core of the resolution function.

As we have discussed in regard to assigning hits to tracks, one way to handle this is to use the standard deviation as weights in the least-squares vertex fit. There are several problems with that, however. First, the algorithm discriminates against tracks that are significant because they are in the resolution tail. These tend to not be included in the constructed IP, so a straight-forward use of the

event type	fit Gaussian width	standard deviation
uds	1.40	1.43
c	1.75	1.85
b	2.23	2.79

Table 5 Normalized accuracy of the IP finding algorithm. The center column is the result of fitting a Gaussian to the curves of Figure 63. The right column is the standard deviation of the same curves. The agreement between fit Gaussian width and standard deviation indicates the distribution does not have large non-Gaussian tails.

standard deviation of the track error instead of the core width would be an overestimate. Further, the number of tracks in the final vertex is quite small, typically less than 10, so our earlier arguments using the Central Limit Theorem are not as compelling. The effects of a noticeable tail remain visible when combining four or five tracks to form a vertex; by comparison, they are completely masked when assembling 100 hits onto a track.

Finally, we don't actually know the standard deviation for a given track *a priori*. Our tracking calculations give the width of the core distribution. Since much of the non-Gaussian tail of the resolution function arises from an unknown cause (Chapter 4) or from assignment of the wrong SSVD hits to a track, a calculation based on residual widths will give the wrong answer.

Given these difficulties, we have chosen not to directly correct the error ellipse calculated for the IP position measurement. In the next chapter we will add 15 microns in quadrature to the assigned impact parameter resolution. Some part of this can be attributed to the underestimate of IP error by this finding method. It is not a problem for the R_b measurement, however, as will be discussed in Section 5.2.

3.9 Impact Parameter Signing

As described earlier, we need an approximation to the B hadron flight direction in order to properly sign impact parameters in events. We have chosen the thrust axis from among many possibilities.

The thrust axis $\hat{T}$ is a unit vector chosen so as to maximize

$$T = \max \frac{\sum_i |\vec{p}_i \cdot \hat{T}|}{\sum_i |\vec{p}_i|} \tag{25}$$

where the sum is over all particles in the event. As seen in Figure 64, the thrust axis approximates the B hadron flight direction with a resolution of about 120 milliradians in ϕ. This resolution is important, as a large enough angular difference between the B hadron flight path and the thrust axis can result in changing the sign of measured impact parameters. Figure 65 shows the size of this effect for events containing b quarks. Some tracks are reflected from the positive S half of the plot to the negative S side when the thrust axis is sufficiently different from the B direction so as to change the sign of the track. The logarithmic plot scales make the effect look much larger for negative S than for positive S.

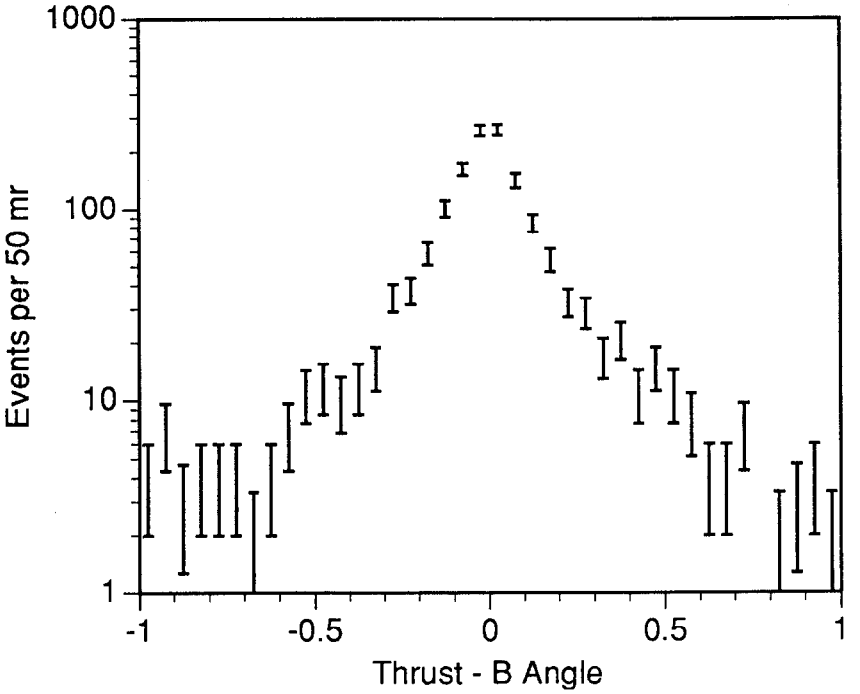

Figure 64 Angular error in ϕ when using the thrust axis to estimate the B hadron axis. This plot was made using the Monte Carlo generated B hadron direction.

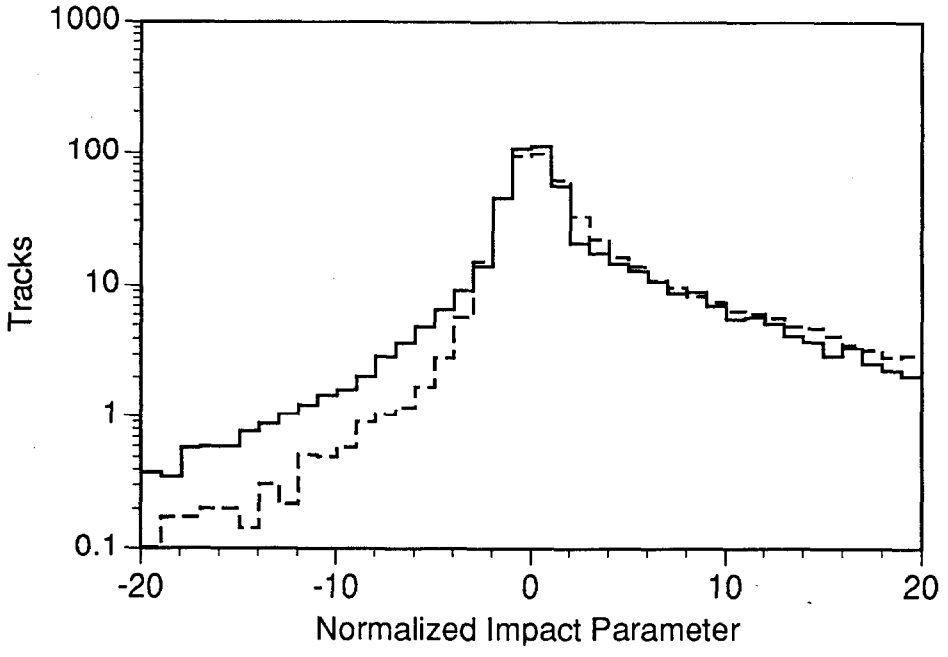

Figure 65 The effect of using the thrust axis to sign the normalized impact parameter. The solid line is tracks from *b* quark events signed using the thrust axis, while the dashed line is the same tracks signed using the Monte Carlo B hadron direction.

The popular mind, in all times and countries, has always tended to go by numbers in estimating the weight of evidence.

Wigmore on Evidence

4 Tracking Performance

In this chapter we examine the tracking system's actual performance for reconstructing tracks. This will provide information needed to calibrate the b quark tagging algorithms, and allow us to set limits on systematic errors due to tracking imperfections.

We will separately check the resolution and efficiency of the tracking, and place a limit on our ability to find a mean IP position. We also study various systematic errors along the lines of those shown in "Systematics" on page 68.

4.1 Resolution

As discussed in Chapter 3, many factors contribute to the resolution of the tracking system. We want to ensure that these are properly modeled in our Monte Carlo simulation, so we compare the normalized impact parameter distribution in the data and simulation.

4.1.1 Normalized Impact Parameter

Unlike in the Monte Carlo resolution studies of Chapter 3, a comparison with the data must allow for an imperfectly known IP position. Here we will be using the IP found in each event to determine the impact parameter, and determine its sign using the thrust axis as described earlier.

The tracking resolution used to normalize the impact parameter has three components added in quadrature. The first component is the track impact parameter resolution calculated as part of the track fit, which we examine using a

'high precision' sample consisting of tracks with a calculated resolution of better than 25 microns.

The second component is the projected IP error from the vertex ellipse. This is taken directly from the result of the procedure defined in "IP Finding" on page 71. If the track in question is included in the primary vertex by the vertex finding algorithm, we remove the track from the vertex before calculating the error ellipse. This makes the found location of the primary vertex independent of the track in question. The Monte Carlo IP position is generated with a 30 micron Gaussian distribution to model the motion of the SLC beams, which we will quantify in Section 4.3.

The final contribution is a constant (taken to be 15 microns) which brings the core of the normalized impact parameter distribution closer to unit width. It partially compensates for the effect of underestimation of the IP position error (Section 3.8) and remaining alignment uncertainty in the SSVD. It should not be taken as the actual size of the alignment uncertainties, which were discussed in Section 3.6.4.

To summarize, the normalized impact parameter S is defined as

$$S \equiv \frac{b}{\sqrt{\sigma_{\text{track}}^2 + \sigma_{\text{IP}}^2 + (15\mu)^2}} \tag{26}$$

4.1.2 Cuts

We select tracks using the same cuts as will be used for measuring the branching fraction:

1. The track must have been assigned at least 25 of 72 possible hits in the CDC.
2. The track must have a measured $|\cos\theta| \leq 0.8$.
3. The z offset of the point where the track is closest to the IP in the xy plane must be less than 15 mm, i.e. $|ZM| \leq 15\text{mm}$.
4. The measured momentum in the xy plane must be greater then 150 MeV/c, i.e. $P_{xy} \geq 150\text{MeV/c}$.

These first cuts select tracks which we expect are very well measured in the CDC, where track finding is initially done. Further cuts are then made:

5. The track must receive at least 15 of 32 possible hits in the DCVD.
6. The track must receive at least 1 hit in the SSVD.

7. The impact parameter resolution of the track must be better than 200 microns.

These cuts are meant to ensure that the track is correctly measured by the vertex detectors and has well understood impact parameter resolution. A last cut is meant to remove many K and Λ decays, along with obvious victims of mistracking and nuclear scattering:

8. The track must pass within 2 mm of the IP in the xy projection, i.e. $|b| \leq 2\text{mm}$

In addition, there are event cuts designed to select hadronic Z decays. To be included, an event must have[47]

1. At least 7 charged tracks which pass the first four cuts above.
2. At least 45 GeV visible energy. Neutral tracks (calorimeter energy clusters) are included. Charged tracks must pass the first four cuts above and are assigned the pion mass.
3. The mass of each hemisphere of the event, defined using the thrust axis, must be greater than 2.2 GeV/c. Charged tracks are assumed to have pion masses and neutral tracks are included.

These cuts remove unwanted di-electron, di-muon and di-tau contamination from the sample.

A total of 220 events containing 2640 tracks pass all cuts. Of these tracks, 641 have a calculated track resolution better (less) than 25 microns and are included in the high precision sample. The effect of the cuts on the bottom quark content of the event sample will be discussed later.

4.1.3 Core and Tail Resolution Comparison

We are now in a position to compare the Monte Carlo predictions with the data. Figure 66 compares the predicted normalized impact parameter distribution (S) with that observed. This plot uses only the highest precision tracks to enhance the effect of a tracking imperfection. Clear Gaussian core and non-Gaussian tail sections are visible, and the tail is more noticeable in the data than in the Monte Carlo simulation.

The tracks from long-lived b quark decays are predominantly found on the right (positive) side of this plot because of the method used to set the sign of the impact parameter using decay length. In the Monte Carlo, Figure 67 shows that the shape and amplitude of the left (negative) side of the distribution are relatively indifferent* to the fraction of events containing b quarks. We will use all the

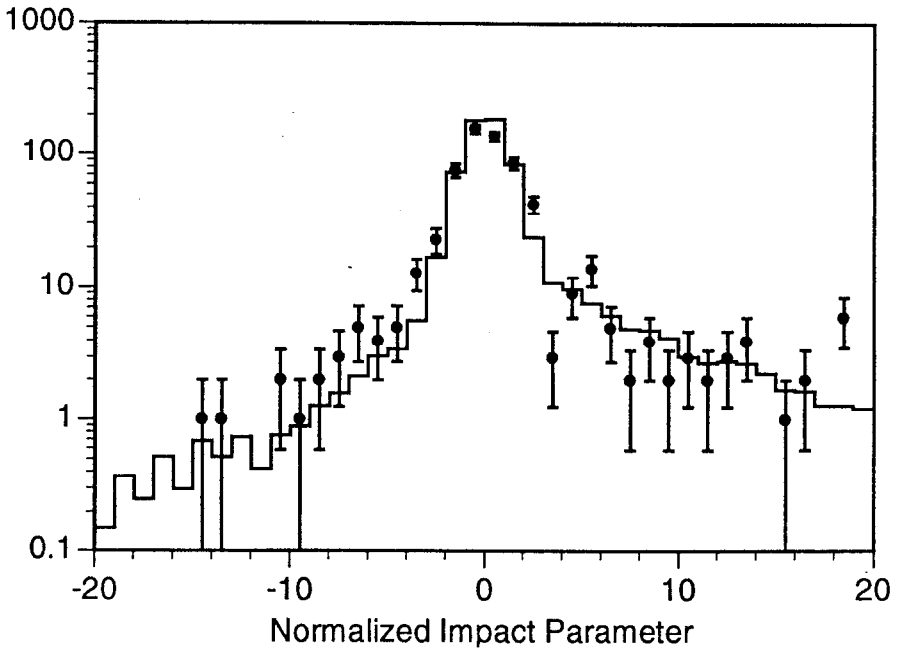

Figure 66 Comparing the normalized impact parameter (S) in the data and Monte Carlo. This plots contains only tracks with calculated track resolution better than 25 microns. There are 624 data entries, shown with statistical error bars. Two tracks underflowed off the plot to the left and 15 overflowed to the right. The Monte Carlo (solid line) is based on 20,000 events.

negative significance tracks as a measure of the tracking resolution function and compare it to a Monte Carlo simulation with an R_b equal to the Standard model prediction of 22.5%. We make the explicit assumption that the resolution function is symmetric about zero.

Inspection clearly indicates that the data tail is underestimated by the Monte Carlo for S from about -12 to -3. As an example of the effect of an increased non-Gaussian tail on the resolution function, Figure 68 compares the original Monte Carlo prediction to one which has had the tail increased by smearing the impact parameter of 15% of the tracks with a 75 micron Gaussian distribution. The difference is in just the same region of the plot, so we can represent the data using this type of smearing. We will now study the properties of the required excess resolution function tail.

* Using the fitting techniques described later in this section, we determine that the change in the fit parameters due to varying the Monte Carlo R_b value from 0.0 to 0.225 is much less than the errors in the fit to the data. We consider this negligible, given that our measured value of R_b is 0.230 is consistent with the value used in the Monte Carlo.

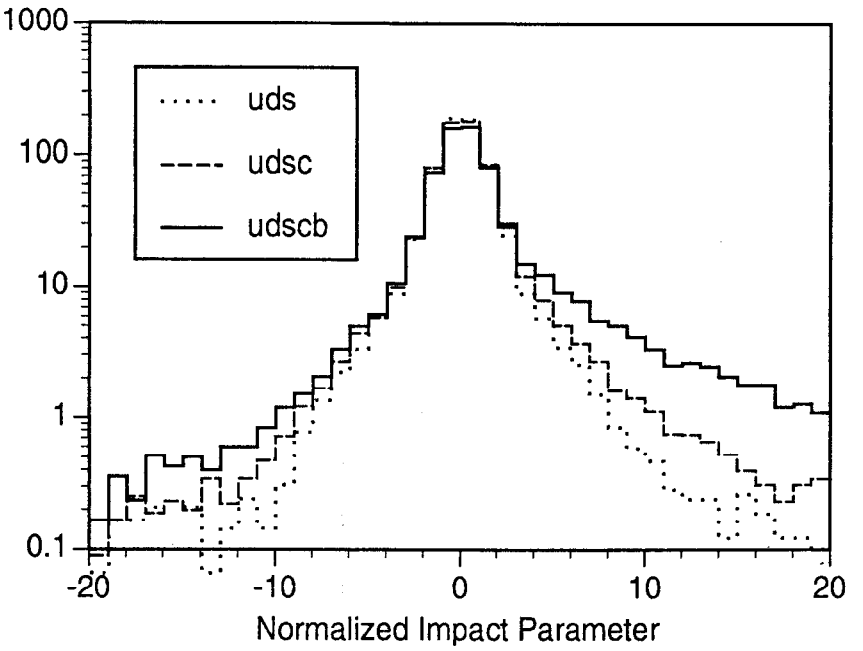

Figure 67 Monte Carlo normalized impact parameter (S) distributions for events containing various types of quarks. The bottom quark fraction varies from 0% to 22.5% in these curves. The differences in the range of normalized impact parameter between -5 and -10 are small.

We need a way to quantify changes in the resolution function on the negative side. We do this by fitting a function consisting of a Gaussian core of variable width and an exponential tail.* We take the exponential tail to be the same on both sides, but fit only on the negative side of the plot:

$$y = Ae^{-\left|\frac{s}{\lambda}\right|} + Be^{-\frac{s^2}{2\sigma^2}}. \qquad (27)$$

* It's perhaps more traditional[57] to use a Gaussian core and Gaussian tail, although there is precedent for exponential tails.[66] As can be seen from the Monte Carlo curves in Figure 66 and Figure 69, however, the existing tail falls off more slowly than a Gaussian distribution. Combined with limited statistics in the tail, a two Gaussian fit is unable to place statistically useful limits on the width of the tail.

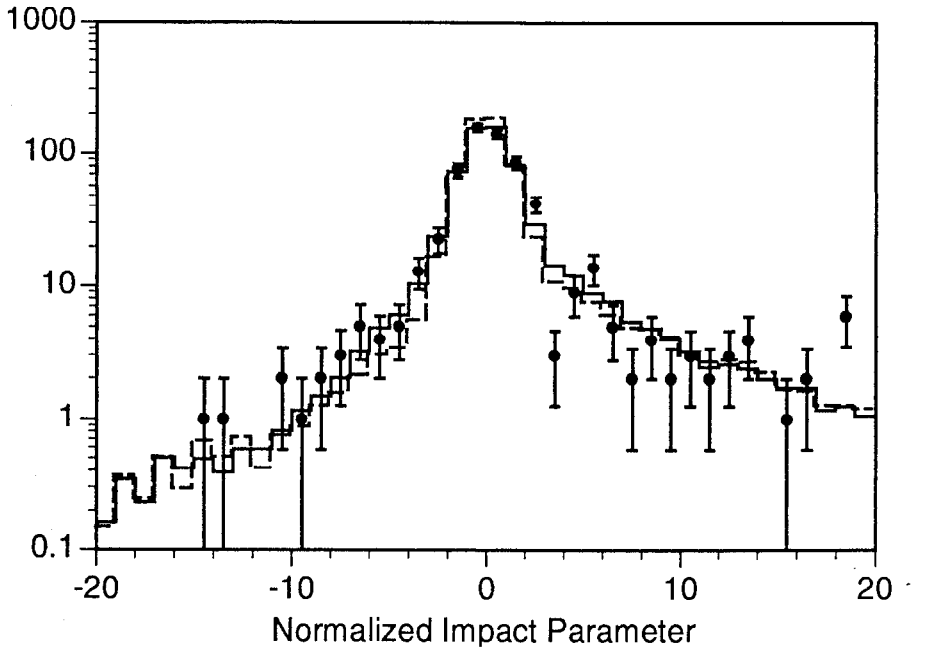

Figure 68 Normalized impact parameter (S) in the data versus Monte Carlo with and without added tail. The solid line is a Monte Carlo in which 15% of tracks have had 75 microns of Gaussian error added. The light dashed line is the original Monte Carlo simulation of Figure 66.

The results of the fit are then the width σ of the Gaussian core, the characteristic length λ of the exponential tail, and the fraction α of the tracks that are found to be in the exponential tail:

$$\alpha \equiv \frac{A/\lambda}{\frac{A}{\lambda} + \frac{B}{\sqrt{2\pi}\sigma}}. \tag{28}$$

Figure 69 shows the fit to the unsmeared Monte Carlo. The exponential tail fits the distribution well for $S > -15$, and the small number of tracks in the data sample with $S < -15$ (Figure 66) limits our sensitivity to the shape of the fitting function there.

Table 6 shows the results of fitting the data and unsmeared Monte Carlo. All Monte Carlo fit results in this chapter have negligible statistical errors. The Monte Carlo is clearly underestimating the tail population. The smaller λ (tail length) in the data indicates that the excess is at S values near zero, and not at large negative S values in the tail. This level of disagreement is unacceptable.

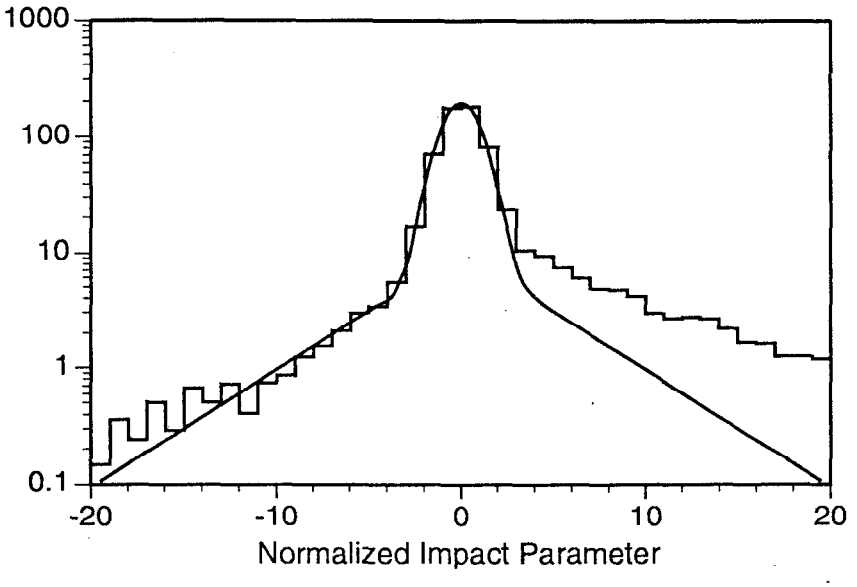

Figure 69 Gaussian and exponential fit to Monte Carlo prediction. This fit to bins with normalized impact parameter (S) less than zero found 92% of tracks in a Gaussian core of width 1.04 and 8% of tracks in a tail of exponential length 4.26. The long lifetime tracks show up clearly on the right.

$\sigma < 25$ tracks	core width σ	tail length λ	tail fraction α
data	1.10±0.034	3.14±0.29	0.173±0.032
unsmeared Monte Carlo	1.04	4.26	0.077

Table 6 Values found by Gaussian/exponential fits. The data includes 641 tracks with calculated resolution better than 25 microns, while the Monte Carlo has about 10,000 tracks. The three fit parameters are defined in the text. The Monte Carlo statistical errors are negligible in all tables in this chapter.

By applying different smearing in the Monte Carlo we can search for a characterization of the difference between the data and the Monte Carlo fits. We choose a 3 dimensional space:

1. We change the width of the core by adding to the impact parameter of every track an error selected from a Gaussian distribution of width C. We call this the 'additional core smearing'.

2. Some fraction of tracks are randomly selected to be in a tail. This fraction F is typically 0 to 25%.
3. The tracks selected to be in the tail then have another Gaussian distributed offset added to their measured impact parameter. The width of this 'tail excess error', M, is typically about 100 microns.

Table 7 and Table 8 show examples of the effects of each of these parameters on the resulting fits in the Monte Carlo. The interaction between the three smearing parameters C, F and M and the three fit parameters σ, λ and α is quite complex because of the non-linearity of the fit. Narrow tails, those with M less than 50 microns, tend to show up strongly as increased core width σ. They effect the fit tail width λ and fraction α much less than smearing with M in the 75 to 100 micron range.

$\sigma < 25$ micron tracks	core width σ	tail length λ	tail fraction α
unsmeared Monte Carlo	1.03	4.26	.077
+5 microns	1.09	3.98	.061
+10 microns	1.14	4.60	.074
+15 microns	1.22	4.35	.075
+20 microns	1.32	4.18	.080

Table 7 Effect of core smearing on fits to the normalized impact parameter distribution. The most consistent change is in the 'core width' itself.

Table 8 shows the effect of an additional tail smearing on each of the three fit parameters. In general, as you add more of a medium size (M of 75 to 100 microns) tail, the fit tail width λ tends to decrease. This is again because these smeared tracks tend to populate regions of the distribution near $S = 0$, with most of the 'naturally occurring' tail at larger values of negative S. Note that the upper and left edges of Table 8 all correspond to the same case: no extra tail smearing.

We have explored the relevant section of the entire $C/F/M$ space and relegate the set of fit results to Table 21 through Table 23 in Appendix C.

σ	data = 1.10±0.034	*F*, fraction in added tail				
	0	5%	10%	15%	20%	25%
M, tail excess error 0	1.09	1.09	1.09	1.09	1.09	1.09
25	1.09					
50	1.09	1.10	1.12	1.16	1.19	1.23
75	1.09	1.08	1.08	1.11	1.15	1.16
100	1.09	1.09	1.07	1.08	1.10	1.11
150	1.09		1.08	1.09	1.11	1.09
200	1.09					
300	1.09					

λ	data = 3.14±0.29	*F*, fraction in added tail				
	0	5%	10%	15%	20%	25%
M, tail excess error 0	3.98	3.98	3.98	3.98	3.98	3.98
25	3.98					
50	3.98	4.05	3.57	3.56	3.54	3.35
75	3.98	3.89	3.26	3.27	3.18	3.08
100	3.98	4.16	3.78	3.49	3.43	3.32
150	3.98		4.13	4.47	4.33	4.53
200	3.98					
300	3.98					

α	data = 0.173±0.032	*F*, fraction in added tail				
	0	5%	10%	15%	20%	25%
M, tail excess error 0	0.061	0.061	0.061	0.061	0.061	0.061
25	0.061					
50	0.061	0.083	0.100	0.108	0.120	0.134
75	0.061	0.096	0.137	0.158	0.189	0.218
100	0.061	0.100	0.136	0.180	0.211	0.254
150	0.061		0.144	0.174	0.210	0.244
200	0.061					
300	0.061					

Table 8 Effect of tail smearing on fit parameters. Values in this table are from fits to the Monte Carlo with 5 microns additional core smearing. See the text for further discussion. This table is a duplicate of Table 22 in Appendix C.

We define a χ^2 for the match between the data and Monte Carlo fit values as

$$\chi^2 = \frac{(\sigma_{data} - \sigma_{MC})^2}{\sigma_\sigma^2} + \frac{(\lambda_{data} - \lambda_{MC})^2}{\sigma_\lambda^2} + \frac{(\alpha_{data} - \alpha_{MC})^2}{\sigma_\alpha^2} \quad (29)$$

where the subscripts on the resolution parameters indicate results from the fit to data or Monte Carlo, and the σ_α, etc., are the statistical errors from the fit to the data. This formula ignores the cross terms as their coefficients are not well defined in a non-linear fit such as this one and a Monte Carlo study indicates that their effect on the final χ^2 is small. A more mathematically rigorous procedure would use a maximum likelihood fit to the full distributions, but the extra computation is neither practical nor justified.

We use this χ^2 to decide which smearing models are consistent with the data and which are not. Table 10 shows the $\chi^2$of the match between the Monte Carlo fits shown in Table 21 through Table 23 and the data, shown in Table 6. A χ^2 that is more than one larger than the minimum is sufficient to statistically exclude a given smearing combination, but we conservatively include adjacent combinations when the χ^2 is less than 3. The highlighted regions are the allowed range of Monte Carlo smearing that we will use in Chapter 5 to bracket the systematic effects of tracking on our physics measurement. Note that the original unsmeared Monte Carlo with $C = F = M = 0$ has $\chi^2 = 28$, which rules it out.

We select 5 microns additional core smearing and an added tail of 75 microns in 15% of tracks to match the Monte Carlo simulation to the data. Table 9 shows that these values, which were also used for Figure 68, generate quite acceptable fit parameters.

σ < 25 tracks	core width σ	tail length λ	tail fraction α
data	1.10±0.034	3.14±0.29	0.173±0.032
smeared Monte Carlo	1.11	3.27	0.158

Table 9 Fit results for best match Monte Carlo smearing, which is 5 microns additional core smearing plus a 15% tail with 75 micron width. Others are very similar.

We will see in Section 4.3 that this tail is still qualitatively present in the normalized impact parameter with respect to a mean IP, which indicates that it is not an artifact of our procedure for finding the IP within the event.

C = 0 microns	*F*, fraction in added tail					
M, tail excess error	0	5%	10%	15%	20%	25%
0	28.15	28.15	28.15	28.15	28.15	28.15
25	28.15		26.10	24.70	28.29	
50	28.15	12.54	5.16	4.05	6.70	13.70
75	28.15	10.04	2.82	0.43	1.43	4.39
100	28.15	12.37	3.10	2.56	3.14	7.76
150	28.15		26.43	21.68	24.12	
200	28.15					
300	28.15					

C = 5 microns	*F*, fraction in added tail					
M, tail excess error	0	5%	10%	15%	20%	25%
0	20.73	20.73	20.73	20.73	20.73	20.73
25	20.73					
50	20.73	17.76	7.75	9.34	11.65	16.63
75	20.73	12.82	1.78	0.51	2.43	5.13
100	20.73	17.66	6.99	1.85	2.41	6.88
150	20.73		12.82	21.12	18.26	27.98
200	20.73					
300	20.73					

C = 10 microns	*F*, fraction in added tail					
M, tail excess error	0	5%	10%	15%	20%	25%
0	36.30	36.30	36.30	36.30	36.30	36.30
25	36.30					
50	36.30		16.36	22.33	14.40	
75	36.30		7.48	7.52	9.00	
100	36.30		12.05	8.44	4.79	9.69
150	36.30				24.84	
200	36.30	67.85	79.24		99.90	
300	36.30					

Table 10 χ^2 of the match between Monte Carlo and data fit parameters for high precision tracks. The three sections of the table are for 0, 5 and 10 microns additional core smearing *C* respectively. The allowed region is enclosed in a double box.

4.1.4 Leptonic Z Decays

Events where the Z^0 decays to a pair of electrons or muons are advantageous for studying intrinsic resolution because they provide two high momentum tracks known to come from a single point. The distance between the tracks then becomes a simple indicator of tracking performance that does not depend on knowledge of the IP position. Unfortunately, we have only 14 events after momentum, acceptance, hit count and acoplanarity cuts. The RMS miss distance of all 14 track pairs is 35±7 microns (Figure 70). This should be contrasted with a Monte Carlo prediction of 35 microns when the smearing determined in Section 4.1.3 is added. The Monte Carlo simulation also predicts 15 microns when the limited SSVD alignment statistics are taken into account and 10 microns for a perfect tracking system. Three of these events have miss distances greater than 50 microns, which is consistent with the 4 expected when the tail smearing is introduced. If those are removed, the RMS miss distance drops to 16±4 microns which is consistent with the Monte Carlo value of 15 microns. The statistics are not compelling, but the results are consistent with the resolution studies earlier in this chapter.

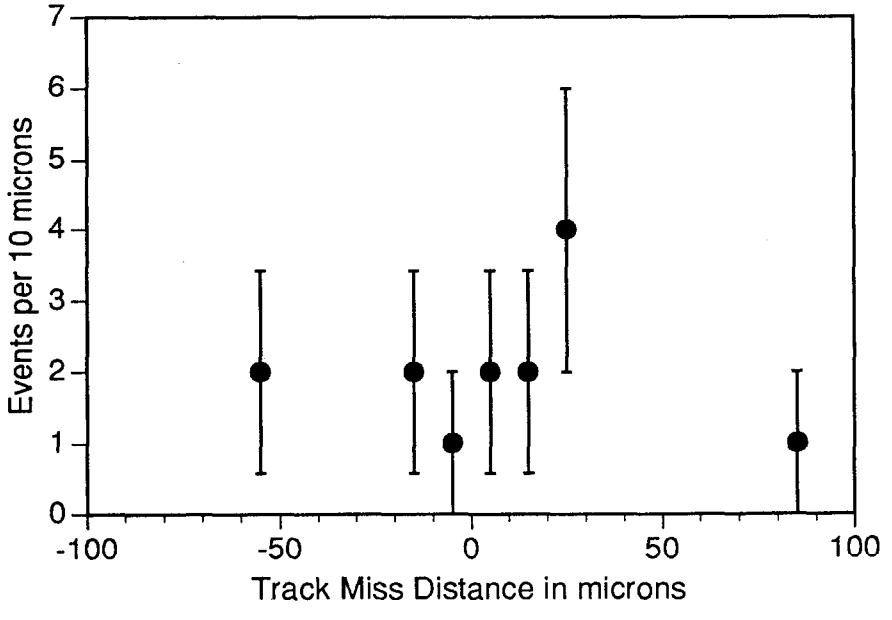

Figure 70 Miss distance in electron and muon pair events. There are 14 events plotted with an RMS miss distance of 35 microns.

4.1.5 Limit on Tracks With Very Large S

The method of "Core and Tail Resolution Comparison" on page 81 runs out of statistical power for $S < -12$. As mentioned in the caption to Figure 66, there are two tracks with normalized error less than –20. The Monte Carlo predicts 1.90 after smearing. Using the Particle Data Book[13] prescription for Poisson confidence limits in the presence of background, the 1 standard deviation limit is 2.4 tracks, which conservatively corresponds to an extra 0.2% tail possible at normalized errors greater than 20.

Possible sources of such large normalized impact parameter include nuclear scattering and photon conversions. Because of the way normalized impact parameter is signed, there is some concerned that these effects will preferentially be given positive signs, so that they could not be characterized by the $S < -20$ tracks. Inspection of the geometry (Figure 71) shows that particles which undergo a large angle scatter at some large radius, for example in the beampipe at 25 millimeters, will be signed positively for two different ranges of the scattering angle. The lower left region is positively signed because the track crosses the thrust axis at a larger radius than where the scatter took place.

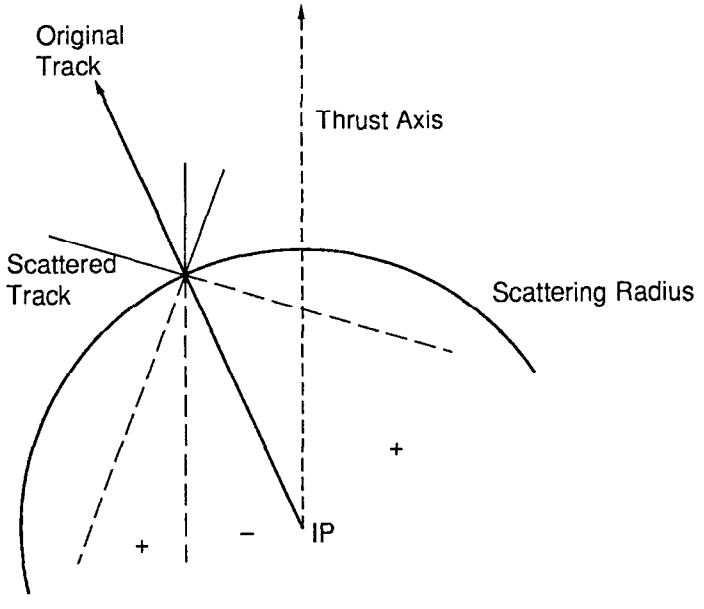

Figure 71 Scattering geometry. The + and – signs label the impact parameter sign given by the decay length algorithm. See text for explanation.

Because we cut tracks with impact parameters larger than 2 millimeters, tracks which scatter more than 2 mm away from the thrust axis will be equally likely* to be given a positive or negative sign. About 68% of all tracks and 46% of tracks in the high precision sample cross the beampipe more then 2mm from the thrust axis. No excess of large S tracks, either positively or negatively signed, is seen. This is consistent the limit of 0.2% found earlier.

4.1.6 Resolution Function for All Tracks

Having used the quarter of all tracks with the highest impact parameter resolution to examine tracking performance, we now turn to the normalized impact parameter (S) distribution for all tracks. Figure 72 shows the overall agreement between data and Monte Carlo normalized impact parameter is quite good. To achieve this we have included the smearing determined in Section 4.1.3 and made adjustments at the 10% level to the thickness of Monte Carlo material layers causing scattering. Table 11 shows the results of Gaussian and exponential fits to the normalized impact parameter for all tracks - the agreement is satisfactory.

Since the smearing is done in terms of 'microns', not in terms of 'sigmas', its effect is much smaller for the lower momentum tracks. The complete set of fits to all Monte Carlo tracks after various smearing combinations is shown in Table 24 through Table 26 in Appendix C. Inspection shows the smearing has some effect; Table 12 shows the χ^2 for the various Monte Carlo smearing combinations. Note that the low χ^2 region in this table is slightly different from that of Table 10, the fits for high precision tracks. The inclusion of low momentum tracks has reduced the sensitivity of the fit, expanding the allowed area in Table 9.

all tracks	core width σ	tail length λ	tail fraction α
data	1.17±0.02	3.66±0.30	0.087±0.015
smeared Monte Carlo	1.16	3.39	0.094

Table 11 Resolution fit values for all tracks. The technique is similar to that of Table 6.

4.1.7 Effect of Thrust Axis Uncertainty

We use of the thrust axis as an approximation to the B hadron flight direction when determining the sign of the normalized impact parameter. This occasionally

* Tracks in the lower left + region of Figure 71 will fail the impact parameter cut.

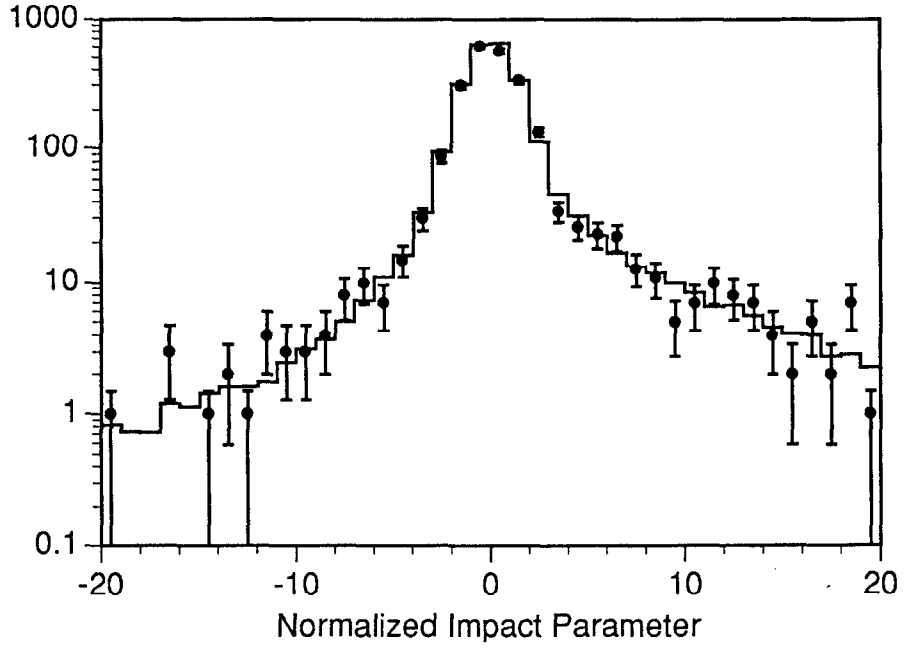

Figure 72 Comparison of normalized error (S) in data and Monte Carlo. This plot includes all 2341 data tracks passing cuts. The Monte Carlo includes 5 micron additional core smearing and a 15% tail of 75 microns width. The Standard Model bottom quark branching ratio of 22.5% is used.

results in the wrong sign determination, as described in Section 3.9. Table 13 shows the effect of this uncertainty on the fit parameters used to examine resolution. As the direction used to approximate the B hadron direction becomes less accurately estimated (lower rows in the table), the tail length parameter λ increases and becomes less consistent with the data. This can be qualitatively understood by examining Figure 69 on page 85. For positive S values the excess above the fit curve is larger at higher values of S. Reflecting some fraction of this to negative S values will then tend to decrease the slope of the fit to negative S region, increasing λ.

4.1.8 Impact Parameter Distributions

As an additional check, we can directly compare the impact parameters found in the data and Monte Carlo after smearing. Figure 73 is the result of partitioning the tracks into six approximately equally populated bins in P_{scat}. The vertical axis is the mean squared impact parameter for comparison with Figure 47 on page 52, but note that the uncertain IP position and the presence of large impact parameters from long-lived particles increase the impact parameters seen in Figure 73. The agreement is satisfactory.

C = 0 microns

M, tail excess error \ *F*, fraction in added tail	0	5%	10%	15%	20%	25%
0	14.16	14.16	14.16	14.16	14.16	14.16
25	14.16		11.28	8.39	7.78	
50	14.16	10.27	4.56	0.79	0.55	2.43
75	14.16	6.16	2.58	1.28	3.38	9.30
100	14.16	7.19	2.78	8.21	10.19	22.12
150	14.16		6.16	12.18	22.94	
200	14.16					
300	14.16					

C = 5 microns

M, tail excess error \ *F*, fraction in added tail	0	5%	10%	15%	20%	25%
0	10.49	10.49	10.49	10.49	10.49	10.49
25	10.49					
50	10.49	7.93	2.88	0.98	1.46	4.22
75	10.49	4.34	2.57	1.28	3.50	9.73
100	10.49	5.03	2.63	10.28	8.64	24.10
150	10.49		4.43	10.09	25.13	40.76
200	10.49					
300	10.49					

C = 10 microns

M, tail excess error \ *F*, fraction in added tail	0	5%	10%	15%	20%	25%
0	8.39	8.39	8.39	8.39	8.39	8.39
25	8.39					
50	8.39		2.36	3.45	2.52	
75	8.39		0.36	1.29	5.56	
100	8.39		0.04	3.10	11.14	27.69
150	8.39				23.69	
200	8.39	4.12	5.77		40.13	
300	8.39					

Table 12 χ^2 of the match between Monte Carlo and data fit parameters for all tracks. The three sections of the table are for 0, 5 and 10 microns additional core smearing *C* respectively. The allowed region is from Table 10.

σ < 25 tracks	core sigma σ	tail width λ	tail fraction α
data	1.10±0.03	3.14±0.29	0.173±0.032
B hadron direction	1.05	3.37	0.062
Thrust Axis	1.04	4.26	0.077
Thrust Error X 2	1.05	4.83	0.096
Thrust Error X 3	1.06	5.01	0.104

Table 13 Effect of B hadron direction uncertainty when signing normalized impact parameter. The lower four rows are the fit results with perfect B hadron direction, the uncertainty due to using the thrust axis, twice and three times the uncertainty due to using the thrust axis. No smearing has been applied to the Monte Carlo.

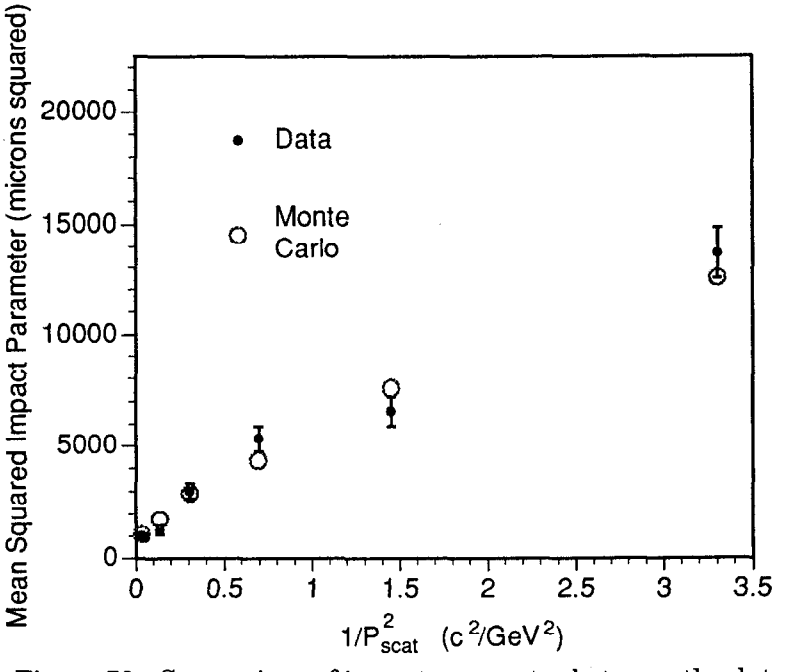

Figure 73 Comparison of impact parameter between the data and smeared Monte Carlo. See text for explanation.

4.1.9 Resolution Summary

The above discussion shows that the system resolution suffers from 5±5 micron excess intrinsic error beyond the Monte Carlo prediction. This is a small number on an absolute scale and we will see later that its effect on the measurement is negligible.

In addition, about 15±5% of the tracks have a resolution that is 75±25 microns worse than predicted by the Monte Carlo. We have not localized this further, although certain possibilities have been ruled out. We checked for the presence of this extra non-Gaussian tail on the resolution function after partitioning the tracks by the track ϕ angle, the thrust axis ϕ angle (which localizes the jet positions), the track and thrust axis θ angles, and both the 2-dimensional and 3-dimensional angles between the track and the thrust axis. Within the very limited statistics available, none of these showed a significant correlation with the presence of the resolution function tail. The data sample was also partitioned by date and time of day without seeing any significant difference. There may be some correlation between detector occupancy from background and the presence of this excess tail, but the evidence is not compelling. We are lead to conclude that, for our purposes, the tail is a random defect.

As we will see in Chapter 5, R_b is determined to be 9% larger when using an unsmeared Monte Carlo resolution function than when using the resolution function determined in this section. The uncertainty in the resolution contributes a fractional systematic error on the R_b measurement of +4% and –10%.

4.2 Tracking Efficiency

Tracking efficiency in the Mark II Central Drift Chamber has been extensively studied[34] in the past. The Monte Carlo has been shown to model the tracking efficiency well. Since we have already shown that the various hit distributions agree, we confine ourselves to checking the overall efficiency of the DCVD and SSVD tracking with respect to the Monte Carlo.

There are 3135 tracks in the data that pass the $\cos\theta$, Z, P_t, $|b|$ and CDC DAZM cuts. Of these, 2341 are assigned at least 15 DCVD hits and 1 SSVD hit and have a calculated track resolution better than 200 microns, thereby passing all our analysis cuts. This percentage of 74.7±1.5% is consistent with the 75.3% seen in the Monte Carlo. The dominant loss of tracks are those not assigned DCVD hits due to lowered DCVD cell high voltage or excessive background.

4.3 Mean IP Finding

Although the SLC's beams are less than 5 microns across, we do not *a priori* know the location of the IP precisely. We have adjusted for the IP motion predicted by the SLC steering magnets, but there may be motions due to thermal expansion and other effects. In Section 4.1 we solved this by using a vertex algorithm to find

the IP position within each event. In this section, we briefly examine the tracking resolution when using the IP that has been found using a number of sequential events, as described in Section 3.8 on page 71.

We again form a normalized impact parameter (S) using equation (26). In this case, σ^2_{IP} is fixed at $(25\mu)^2$. The normalized impact parameter distribution is then fit for core and tails using the technique described in Section 4.1.3. Figure 74 shows the single point from the data, which has a core width of 1.20±0.04. The curve is the result of smearing the IP position in the Monte Carlo simulation with a Gaussian distribution of various widths. The data is consistent with 32±3 microns of IP motion, assuming a Gaussian profile.

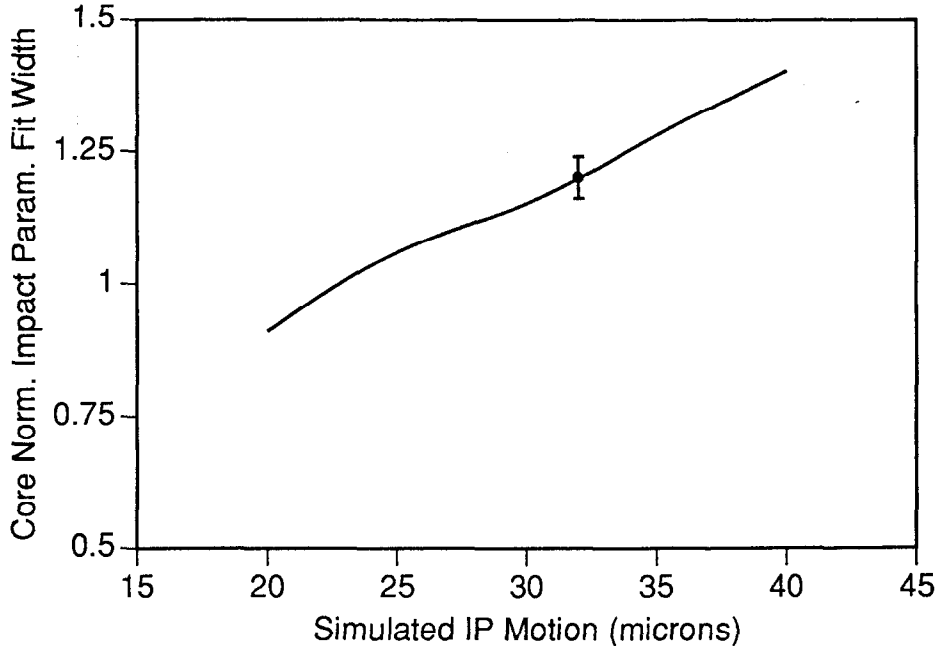

Figure 74 Determining IP motion from the width of the normalized impact parameter distribution. See text for explanation.

Figure 75 shows the normalized impact parameter distribution seen in the data for high precision tracks. The Monte Carlo with 30 microns of IP motion is an acceptable match when the track smearing measured earlier is included, but there is a clear excess of tracks in the data between S values of -1 and -5 when the unsmeared Monte Carlo is used. It is not possible to simultaneously match the core and tails of the data plot by varying the assumed IP motion. Figure 76 is the normalized error distribution for all tracks.

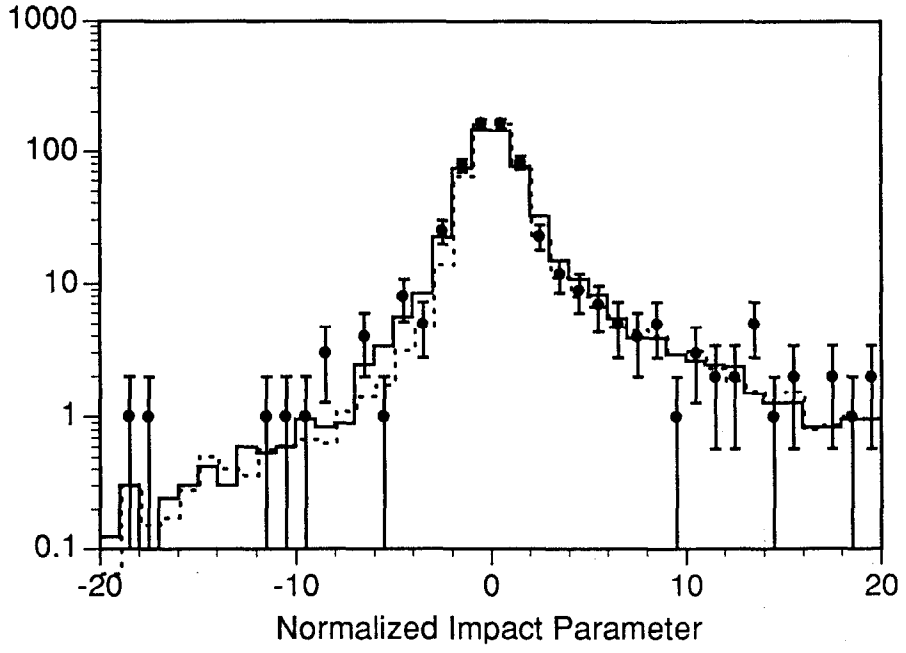

Figure 75 Normalized impact parameter for high precision tracks, found using the mean IP. The solid Monte Carlo curve includes 30 microns IP motion and the best track smearing from Table 9. The dotted curve omits the track smearing and is not preferred.

The Gaussian/exponential fits are consistent with the results from using the IP found in each event. Table 14 shows that the difference is about 1 standard deviation in the α and λ parameters, which correspond to the fraction of tracks in the resolution function tail and its width. Unfortunately, with only 220 events the best limit we can put on an IP position tail introduces a large systematic error on our measurement of R_b. For this reason, we will use the more robust method of finding the IP in each event when extracting R_b.

	core width σ	tail length λ	tail fraction α
data, high resolution	1.06±0.031	3.04±0.29	0.115±0.022
Monte Carlo	1.09	2.50	0.136
data, all tracks	1.11±.020	3.67±0.31	.065±0.011
Monte Carlo	1.15	3.34	.0714

Table 14 Results of Gaussian/exponential fits to the normalized impact parameter found using the mean IP.

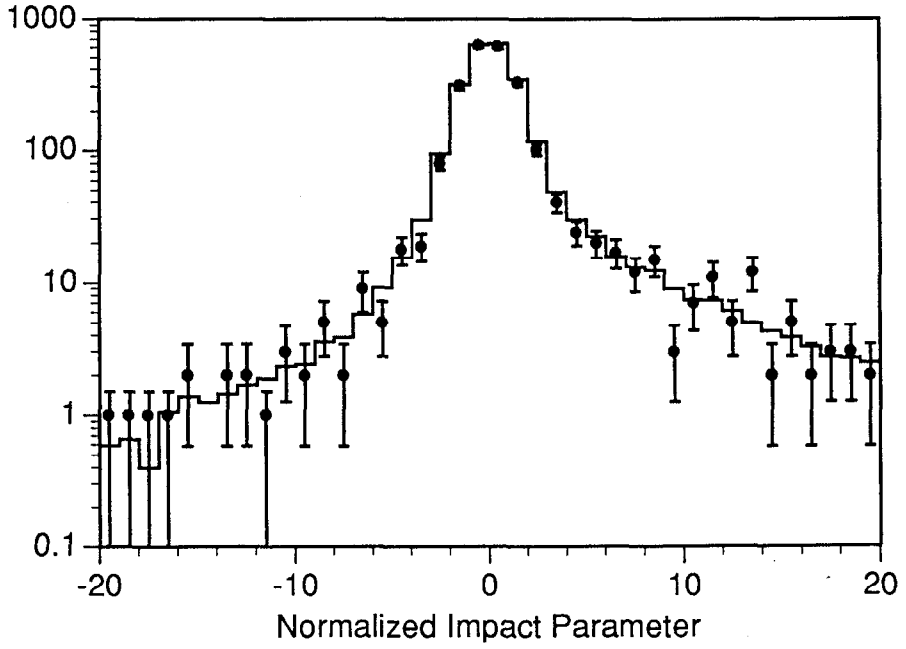

Figure 76 Normalized impact parameter for all tracks found using the mean IP. The Monte Carlo curve includes 30 microns IP motion and the best track smearing from Table 9.

It is not clear whether other methods of monitoring beam position, hopefully with higher statistics, might be able to do better in the future. The goal, of course, is to localize the IP to within the SLC beam spot which is known to be smaller than 5 microns.

4.4 Systematic Tracking Biases

We will be counting Z^0 decays containing b quarks by looking for events that have a number of tracks with large positive impact parameters. We have seen that on the negative side, the Monte Carlo simulation reproduces well the normalized impact distribution.

A systematic bias would be introduced if some fraction of tracks had an offset in their mean impact parameter. We have looked for systematic biases in the tracking in a number of ways. We list the results while omitting the details:

1. The mean of the core was studied by fitting a double Gaussian with unconstrained means to all bins of both the high precision and all track normalized impact parameter distributions. The mean of the core was consistent between Monte Carlo and data, very near zero.

2. This was repeated for smaller samples separately selected by ϕ of the track, ϕ of the thrust axis, or the angle between the thrust axis and the track. No significant variations from zero mean were found.
3. Similar studies in the polar angle θ also found no systematic biases.
4. Comparisons of tracks in different momentum or resolution bins showed the slight resolution differences seen previously, but no shifts in mean normalized impact parameter.
5. Studies of the geometrically signed, i.e. 'right-left', miss distance as a function of track angles and positions found only the signal described in Section 3.6.5. Because the thrust axis is equally likely to fall anywhere within a DCVD cell, this effect does not cause a systematic shift of the mean of the signed impact parameter. The tracks within an event are spread within jets with a typical angular extent wider than a DCVD cell, further randomizing this effect.
6. Studies of tracks in various momentum ranges show no shift of mean impact parameter. Such a shift could be caused by inconsistent alignment between the CDC, DCVD and/or the SSVD, so that as the relative weights of the chambers change with the track momentum, the track would receive differing weighted position information. There is some evidence that the resolution is 5% worse in the 2 GeV/c region. At this momentum, the tracking uses both the SSVD track angle measurement and the DCVD track angle information, resulting in a higher sensitivity to misalignment. Only about 15% of the tracks are in this range and the statistics are not compelling, but we will check the effect of this on the systematic error in Chapter 5.
7. Studies of tracks that receive 1, 2 or 3 SSVD hits show clear differences in their resolution, but most indications are that the Monte Carlo simulation is properly representing the behavior. There have been several hypotheses proposed which, because of background occupancy, give larger impact parameters for tracks that only pick up 1 SSVD hit. Careful examination of these tracks has found no systematically degraded normalized impact parameter and no shifts of the mean impact parameter.

The specific concern was that tracks in some particular 'region' would have anomalously large positive impact parameters, so that events which randomly populated that region would erroneously look like b quark events. One could continue to postulate and rule out different regions forever, but we think the physically likely ones have been checked with no significant signals found.

Just do it.

The Winged Goddess of Victory, Nike

5 Bottom Quark Tagging

We have seen that our precision tracking detector is capable of resolving the large impact parameter tracks present in b quark decays. We now turn our attention to methods for using this information to determine the fraction of events containing b quarks.

We will start with a brief discussion of the desired characteristics and a survey of some possible methods. We will then concentrate on a 'tagging' analysis, where we count events with more than a minimum number of significant tracks. We investigate this algorithm's efficiency and background rejection as a function of it's parameters. We select a parameter set, make a measurement of R_b, and calculate the statistical error.

We then examine some cross-checks on the result. These include several measurements of R_b with different sensitivity to systematic errors. Since these alternate measurements use the same data sample, they cannot be combined to reduce the statistical error but their consistency gives some confidence in the answer. We also look at various properties of the tagged tracks and events to further demonstrate consistency.

We finish by investigating possible systematic errors. These come from identified uncertainties in our understanding of the detector's tracking resolution (Chapter 4), plus uncertainties in several physics parameters used by the Monte Carlo simulation.

5.1 Possible Algorithms

We look for three things in an algorithm:

1. Smallest possible statistical error. This is critical given the small size of our event sample.
2. Measurable systematic errors. It should not be overly sensitive to systematic errors due to causes that are hard to characterize.
3. Simplicity. As we are attempting for the first time to measure R_b using only tracking information, we do not have a large pool of similar experience to fall back on. Subtle arguments about complicated fitting functions should be left for a higher statistics measurement.

The class of algorithms most widely studied was popularized by Hayes.[67][68] In outline, one defines a significance S for each track i using

$$S_i \equiv \frac{b_i}{\sigma_i} \tag{30}$$

where b_i is the track impact parameter and σ_i is the measurement error assigned to b_i. A track is called 'significant' if its significance is greater than a value S_{min}. Events which have one or more jets containing at least N_{min} significant tracks are called tagged events. These tagged events then form a sample enriched in b quark decays. The number of events tagged divided by the total number of events is then used to calculate R_b. Typical values were $S_{min} = 3$ and $N_{min} = 3$.

The original Hayes algorithm had several complications. It did not set the impact parameter sign using the decay length, as we are doing, so there was no asymmetry in the S distribution. This makes the algorithm more sensitive to the amount of non-Gaussian tail in the resolution function. Additionally, a kinematic cut, based on a mass calculated from the significant tracks, was used to reduce the c quark background in the tag.

The subtle point in the Hayes algorithm involves the definitions of b and σ. Neither of them is known precisely, and the errors do not form a Gaussian distribution. In fact, S is the normalized impact parameter we studied in Chapter 4, and its distribution showed tails at the 10% level. The numerical 'significance' of S is then not given by the Gaussian formula, where $S \geq 3$ would only happen erroneously to one track in a thousand. Hence, one must rely on a detailed Monte Carlo simulation to calibrate the efficiency of this algorithm for signal and background events.

Over time the Hayes tagging algorithm has evolved into what we now call a 'hemisphere tagging algorithm' and a 'jet tagging algorithm'. A hemisphere tagging algorithm splits each event into two hemispheres along a plane perpendicular to the thrust axis and selects the event if either hemisphere (or both) contains more than N_{min} significant tracks. A jet tagging algorithm uses the same procedure as the Hayes tag by looking in jets that have been found using some specified procedure. Modern versions of these tags use decay-length-signed impact parameters.

Since a hemisphere tagging algorithm independently examines the two hemispheres of the event, a given event can be tagged zero, one or two times (i.e. each hemisphere can be selected or not, independent of the other). The number of events of each type can then be used to calculate the efficiency of the algorithm without reference to the Monte Carlo simulation. Our data sample is so small, however, that this does not provide any useful information about systematic errors.

A small improvement in statistical error can be gained by counting significant tracks in the entire event. This 'event tagging algorithm' would accept an event with two significant tracks in one hemisphere and a single significant track in the other hemisphere,* which a hemisphere tagging algorithm would not. The event tagging algorithm therefore has an greater probability of selecting a b quark event (for a given N_{min} and S_{min}) than a hemisphere tag. This results in a smaller statistical error for the R_b measurement, and motivates us to use the event tagging algorithm for this measurement. We will describe the details in the next section.

An entirely separate class of algorithms use the track information to search for vertices. Searches for new particles, usually to set null limits, have been made by trying to find separated vertices.[69] Most of these involve vertices well separated from the IP so there is little or no ambiguity as to which tracks should be associated with the separated vertex. Recently Weber[70] improved a method due to Hayes for arbitrating which tracks should be assigned to primary and secondary vertices in an event. He then used the improved algorithm to measure B hadron lifetimes. Although separated vertex searches show great promise, at this stage in their development they fail our simplicity criterion. The increased statistical accuracy that might be obtained comes only at the price of a very complex analysis that depends subtly on the detector resolution. This is because the vertex search must use track parameters and resolutions to make decisions on which tracks to include

* This should not be confused with the positive and negative halves of the normalized impact parameter or S distributions.

in a vertex. This decision process can then introduce additional differences in the result between data and Monte Carlo simulation.

The final class of algorithms takes an entirely different approach. Instead of trying to identify individual events as belonging to a B hadron enriched sample, these define one or more variables in an event which emphasize the impact parameter information. An example is shown in Figure 77, where we plot for each event the variable

$$S^* \equiv \frac{1}{\sqrt{n}} \sum_{i=1}^{n} \frac{b_i}{\sigma_i}, \tag{31}$$

which is the normalized sum of the normalized impact parameters. In the absence of long lived particles, this should be a unit Gaussian distribution. Long-lived b quarks cause the visible asymmetric tail. Schumm[71] has developed a method of fitting this distribution with Monte Carlo predicted distributions to find R_b. The advantage this offers will one day be of value: many of the systematic uncertainties arising from the B hadron lifetime and fragmentation function effect the shape of the S^* distribution but not the amplitude. By fitting for these uncertain parameters it is expected that the systematic errors on the R_b measurement can be driven to quite low values. We shall see, however, that the systematic errors in an event tag are still small compared to the present statistical errors. We again decide in favor of the event tag based on the simplicity criterion.

5.2 The Measurement Algorithm

To summarize, we use an event tag requiring N_{min} or more tracks of significance at least S_{min} in the event. We define the impact parameter using an IP found in each event. We compute impact parameter resolution using the same formula as in Chapter 4, where we combined the calculated track resolution, the IP resolution from the projected IP ellipse, and a constant taken to be 15 microns:

$$S \equiv \frac{b_{\text{(found ip)}}}{\sqrt{\sigma^2_{\text{track}} + \sigma^2_{\text{IP}} + (15\mu)^2}}. \tag{32}$$

We use the track and event cuts described in Section 4.1.2 on page 80.

We now turn to picking the values for the parameters N_{min} and S_{min}. A given choice of these parameters is characterized by the efficiency to tag a b quark event ε_b, and the efficiency to tag a $udsc$ quark event ε_{udsc}. Table 15 lists the efficiency for tagging an event containing b quarks for various choices of the parameters.

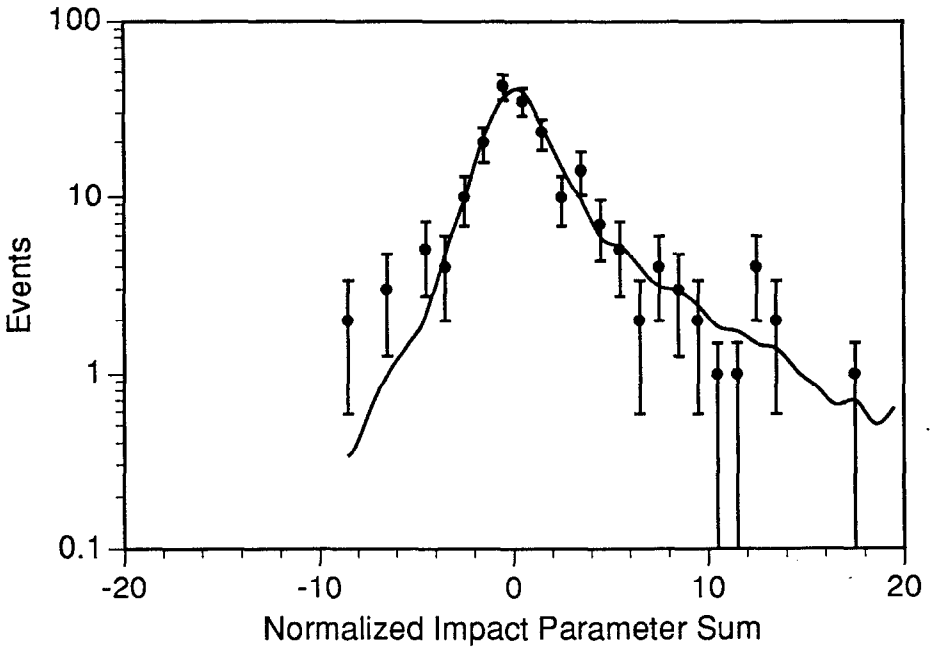

Figure 77 The distribution of S*, defined in equation (31). The curve is from a Monte Carlo with an R_b value of 0.22, and the points are from the data sample.

These numbers were generated by applying the tag to approximately 4400 Monte Carlo events. Every bin was run on the same events. The behavior is as expected - as more tracks or more significance is required, the fraction of events tagged decreases.*

Table 16 is a similar list of the efficiency to tag events not containing b quarks. This table was made from 16,000 events containing *udsc* quarks. Again the behavior is as expected, with a very rapid decrease in the number of events passing the tag when either the number of tracks or the significance is increased.

One measure of the quality of a tagging algorithm is the purity of the events it selects. Purity is defined as the fraction of events in the tagged sample containing b quarks. Table 17 shows this as a function of the parameters. It is a weak function of the fraction of b quarks in the original, untagged sample which we assume to be the

* In this chapter we have a convention to write efficiencies, probabilities and other selections as decimal fractions. For example R_b, which is a fraction of hadronic events, is written as 0.220. Variations, including statistical errors, are written as a absolute decimal number or as a fractional percentage. Thus, for a quantity nominally equal to 0.5, the statements "the error due to ... is ±0.050" and "the fractional error due to ... is ±10%" are equivalent.

Minimum Number of Tracks N_{min}	Minimum Significance S_{min} 1	2	3	4	5
1	0.943	0.892	0.853	0.811	0.765
2	0.868	0.738	0.672	0.603	0.530
3	0.755	0.566	0.482	0.408	0.341
4	0.618	0.399	0.319	0.254	0.192
5	0.477	0.261	0.185	0.136	0.101
6	0.339	0.146	0.101	0.069	0.045

Table 15 Efficiency for an event tag algorithm to tag an event containing b quarks as a function of tag parameters. The event cuts have already been applied. For example, requiring an event to have at least four tracks of significance 2 or more would tag about 0.399 of the events containing b quarks. Monte Carlo statistical errors are 0.005 or less for all entries.

Minimum Number of Tracks N_{min}	Minimum Significance S_{min} 1	2	3	4	5
1	0.819	0.491	0.340	0.261	0.202
2	0.584	0.183	0.091	0.059	0.040
3	0.357	0.058	0.024	0.014	0.008
4	0.186	0.018	0.006	0.003	0.002
5	0.088	0.005	0.001	0.001	0.000
6	0.037	0.001	0.000	0.000	0.000

Table 16 Efficiency ε_{udsc} for an event tag algorithm to tag an event not containing b quarks as a function of tag parameters. The event cuts have already been applied. For example, requiring an event to have at least four tracks of significance 2 or more would tag 0.018 of events not containing b quarks. Monte Carlo statistical errors are less than the larger of 1% or 0.002 for all entries.

Standard Model value of 0.220 for this table. In other words, the untagged sample started with a purity of 0.220, which the tag will then improve.

Minimum Number of Tracks N_{min}	Minimum Significance S_{min} 1	2	3	4	5
1	0.251	0.345	0.422	0.474	0.524
2	0.302	0.540	0.681	0.747	0.795
3	0.381	0.739	0.852	0.896	0.928
4	0.492	0.868	0.937	0.963	0.973
5	0.611	0.937	0.978	0.986	0.992
6	0.725	0.967	0.987	0.988	0.988

Table 17 Purity of the events tagged as a function of tag parameters. For example, requiring events with four or more tracks of significance at least 2 would give a sample in which 0.868 of events contain b quarks. This table assumes R_b = 0.220. Monte Carlo statistical errors are 0.005 or less for all entries.

To evaluate the expected statistical accuracy of each of these parameter choices, we must first develop expressions for R_b and it's statistical error.

We can write the expected number of events passing the event cuts N_{evt} as

$$N_{\text{evt}} = [s_b R_b + s_{udsc}(1 - R_b)]N_{\text{total}} \tag{33}$$

where s_b and s_{udsc} are probabilities for passing the event cuts, 0.819 and 0.795 respectively in this analysis. N_{total} is the total number of produced hadronic events, which we will not need to know.* Similarly, the expected number of tagged events is

$$N_{\text{tag}} = [\varepsilon_b s_b R_b + \varepsilon_{udsc} s_{udsc}(1 - R_b)]N_{\text{total}}. \tag{34}$$

* Although we assume that the Mark II triggered on every produced event, the events failing the event cut include an unknown number of leptonic Z^0 decays which should not be included in N_{total}.

It's convenient to define the fraction of observed events tagged as

$$f \equiv N_{\text{tag}} / N_{\text{evt}} \tag{35}$$

and an event cut efficiency difference using

$$s_b \equiv (1+\Delta_\varepsilon) s_{udsc}. \tag{36}$$

The Monte Carlo simulation indicates that Δ_ε is 0.030±0.015 for this analysis. The equations can then be rewritten in terms of Δ_ε.

We solve the two equations in the two unknowns R_b and N_{total}, finding

$$R_b = \frac{f - \varepsilon_{udsc}}{(1+\Delta_\varepsilon)\varepsilon_b - \varepsilon_{udsc} - f\Delta_\varepsilon}. \tag{37}$$

We will use this equation to compute R_b in our final measurement.

Next we need to calculate the statistical error on the measurement of R_b. We can reduce the algebra associated with s_b and s_{udsc} by first working in terms of

$$R'_b \equiv \frac{R_b s_b}{R_b s_b + (1-R_b) s_{udsc}} \tag{38}$$

which is the b quark fraction after event cuts. R_b and R'_b are 0.220 and 0.225 respectively in the standard Mark II Monte Carlo simulation.

The statistical error in the measurement of R'_b comes from binomial fluctuations between the class of events that are tagged and the class of events that are not. For the statistical error, it doesn't matter whether the event contains b quarks. Any event which has passed the event cuts has a probability $R'_b\varepsilon_b + (1-R'_b)\varepsilon_{udsc}$ of belonging to the class that will be tagged, so the fractional error is

$$\frac{\sigma_{R'_b}}{R'_b} = \frac{\sqrt{\dfrac{(1-R'_b\varepsilon_b - (1-R'_b)\varepsilon_{udsc})\,(R'_b\varepsilon_b + (1-R'_b)\varepsilon_{udsc})}{N_{\text{evt}}}}}{f - \varepsilon_{udsc}} \tag{39}$$

We can change back to R_b using

$$R_b = \frac{R'_b}{1+\Delta_\varepsilon - \Delta_\varepsilon R'_b}, \tag{40}$$

$$\frac{\sigma_{R_b}}{R_b} = \left(\frac{1+\Delta_\varepsilon}{1+\Delta_\varepsilon(1-R'_b)}\right)\frac{\sigma_{R'_b}}{R'_b} \tag{41}$$

We now calculate Table 18, which shows the expected fractional statistical error for our sample of 220 events passing event cuts. We have again assumed that R_b is 0.220 when compiling this table. There is a broad minimum at about 22%.

Minimum Number of Tracks N_{min}	Minimum Significance S_{min} = 1	2	3	4	5
1	87.1%	37.1%	29.2%	26.6%	25.1%
2	50.5%	25.0%	21.6%	21.3%	21.9%
3	37.6%	22.4%	21.9%	23.2%	24.9%
4	31.3%	24.0%	25.6%	28.3%	32.6%
5	29.5%	28.5%	33.0%	38.6%	44.6%
6	30.6%	37.7%	44.8%	54.3%	67.2%

Table 18 Expected fractional statistical precision of an event tag as a function of tag parameters. This table assumes a sample of 220 events passing event cuts and an R_b of 0.220. For example, measuring R_b from the number of events having at least four tracks with a significance of 2 or more would have an accuracy of 24%. This could be stated as $R_b = 0.22*(1.00\pm0.24)$.

We choose $N_{min} = 3$, $S_{min} = 3$ as the tag criteria for our measurement. This is preferred over $N_{min} = 2$ because of reduced sensitivity to the uncertainty in the tracking resolution. This is because of combinatorics: tails in the tracking resolution have more of an effect on tags requiring a smaller number of tracks, as it is much more probable that the tail will provide a small number of significant tracks. We expect $N_{min} = 3$, $S_{min} = 3$ to achieve a purity of approximately 0.85 and 22% statistical accuracy. The tagging procedure favors c quark events over *uds* quark events; approximately half of the tagged background (*udsc*) events are expected to contain c quarks, which is a significant enhancement.

5.3 The Result

Of the 220 events passing cuts, 29 are tagged giving a tagging fraction of 0.1318. This corresponds to an R_b value of 0.230. Using an R'_b value of 0.235, we find a fractional error for R'_b of 21.2% and a fractional error on R_b of 21.3%. The measurement and statistical error is then

$$R_b = 0.230 \pm 0.049. \tag{42}$$

5.4 Checks

Unfortunately, we are limited by the statistics of the number of events recorded by the Mark II. This makes it impossible to place useful, yet statistically valid, limits on systematic effects by sub-dividing the data. Nevertheless, in this section we look at the distributions of significant tracks to verify that the Monte Carlo predictions underlying the R_b calculations are approximately correct. We also examine three modifications to the tagging algorithm, which have different sensitivities to the details of the tracking resolution function, to show that the R_b result is reasonably robust.

5.4.1 Sensitivity to Tag Parameters

We have chosen to tag events with at least three tracks with a significance greater than three. Figure 78 shows the number of events tagged versus the number of tracks required by the tag algorithm. The Standard Model Monte Carlo curve agrees quite well with the data. We would have measured the same R_b value, within statistical errors, regardless of the value of N_{min} used, so our choice to minimize the statistical error was reasonable.

Figure 79 shows the effect of varying the significance requirement. We would have measured the same R_b value, within statistical errors, for any value of S_{min} less than 10. Again the individual points are not independent, but the plot leaves the clear impression of a few events more events in the data than Monte Carlo predicts for significance greater than 10. The Monte Carlo indicates that a deviation at least this large is expected in about 16% of trials, so it is a slightly larger than 1σ effect. Inspection of these events shows clear, well separated vertices with decay lengths in excess of 5mm. This leads us to believe that these events are properly tagged as containing b quarks.

5.4.2 Analysis by Differences

An improperly understood tracking resolution will effect the efficiency of the tagging algorithm. In Chapter 4 and Section 5.5.1 we have gone to some trouble to quantify our sensitivity and uncertainty in this area, particularly with respect to the resolution function tails.

Another approach would be to select a tagging algorithm that is less sensitive to the presence of tails on the resolution function. An example is a 'difference tagging algorithm'. The method is:

1. Count the number of tracks in an event with a significance at least S_{min}. This is called N^+.

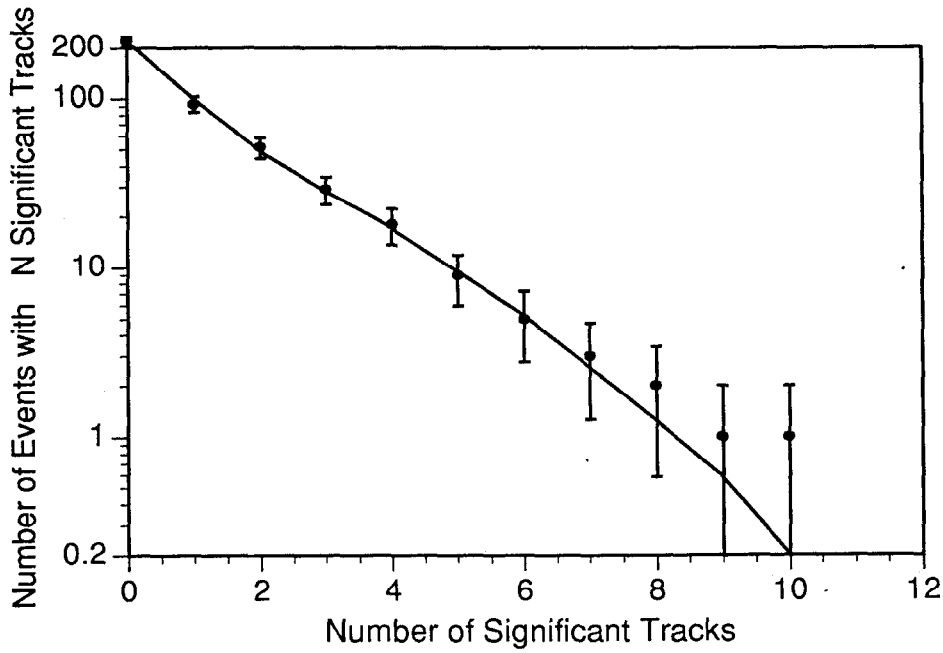

Figure 78 Total number of events tagged as a function of the number of tracks required to have significance greater than three. The curve is the Monte Carlo prediction with the Standard Model value of 0.22 for R_b. This is an integral plot, so the error bars on the points are not independent.

2. Separately count the number of tracks with significance less than $-S_{min}$. Call this N^-.
3. An event is tagged if $N^+ - N^-$ is at least the cut value N_{min}.

A tail on the resolution function that is symmetric between positive and negative values of S would increase the mean value of N^+ and N^- by the same amount. The difference, $N^+ - N^-$, would then be expected to have a lesser increase on the average than N^+ alone.

This method is noticeably less sensitive to the composition of the tail on the resolution function. For example, increasing the fraction of tracks with extra smearing in the Monte Carlo from 15% to 25% results in a 9% fractional change in R_b for the significance tag of Section 5.2 with S_{min}=3 N_{min}=3, but only a 3% change for the difference tag with the same parameters.

Unfortunately, the loss of statistical power is significant. This method was predicted to have a fractional statistical error of 26% as compared to the 22% of the significance tag, which lead us to prefer the significance tag.

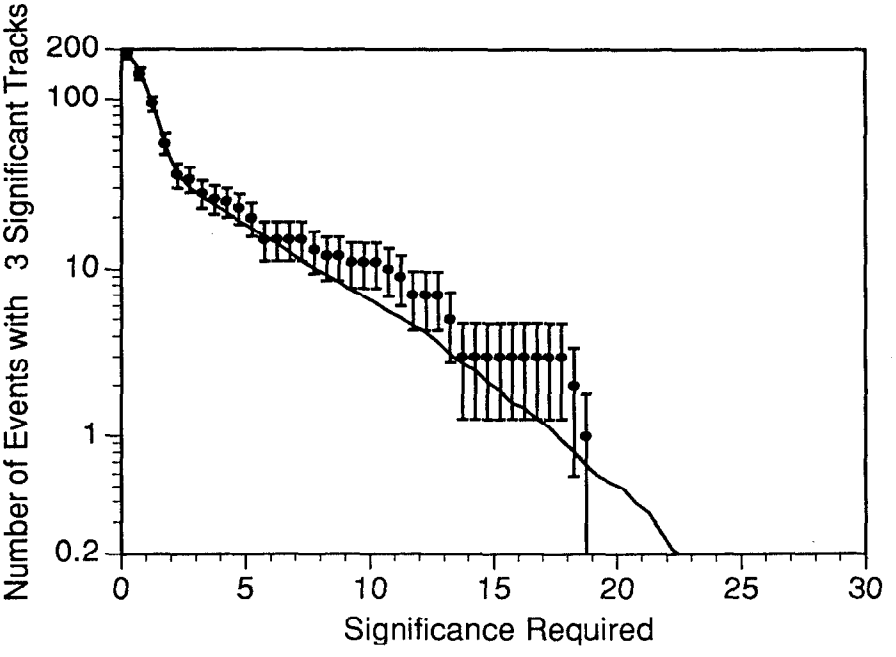

Figure 79 Total number of events tagged as a function of the required track significance. The event is required to have at least three significant tracks. The curve is the Monte Carlo prediction with the Standard Model R_b value of 0.22. This is an integral plot, so the error bars on the points are not

We use the difference tag as a check. For the same S_{min}=3 N_{min}=3 parameters, it tags 18 of the 29 events tagged by the significance tag. Using efficiencies evaluated with the Monte Carlo, this corresponds to an R_b value of 0.183. The Monte Carlo also predicts that 75% of events tagged using the significance tag should be tagged by a difference tag algorithm. This implies that the difference tag should have found 21.7 events with a standard deviation* of 2.2 events. There is a 1.2σ difference between the prediction of 21.7 and the observed 18, which is not considered significant. Fewer events observed than predicted can be caused by a larger tail on the resolution function in the data than predicted by the Monte Carlo.

* Both tagging algorithms are looking at the same sample, and thus the same real number of b quark events. The statistical fluctuations come from the probability that there will be sufficient tracks with significance less than $-S$ to prevent the event from being tagged, which has little sensitivity to the exact value of R_b. This obeys a binomial distribution.

5.4.3 Tagging Using Mean IP

We can repeat the analysis using the mean IP obtained groups of events. In this method, significance is defined using a fixed circular error for the IP instead of the ellipse found in the event. This has the effect of decreasing the significance of high momentum tracks in the core of jets, as the error perpendicular to the thrust axis from finding the IP in the event is usually smaller than the 30 micron circular error assumed for the mean IP. Figure 80 shows the effect schematically.

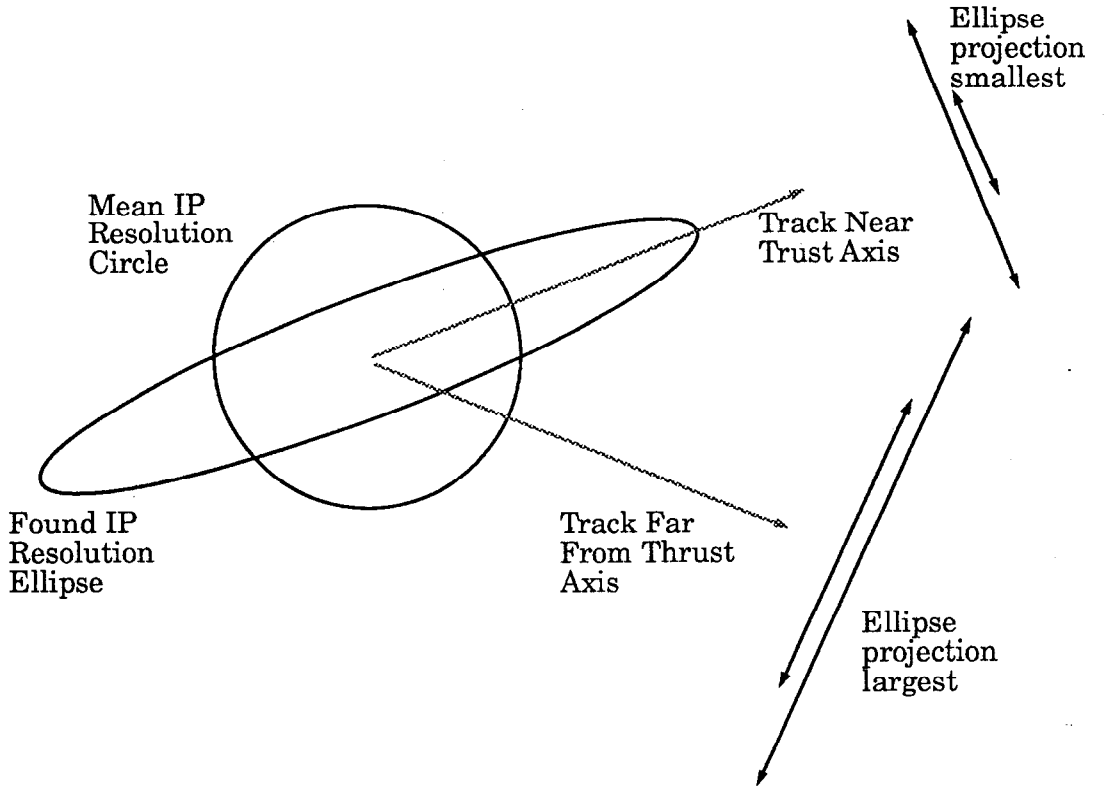

Figure 80 The IP position resolution versus track angle. The circular error of the mean IP is the same for all tracks, but the ellipse for an IP found in the event is more precise for tracks near the thrust axis.

This is compensated to some extent by an increase in average significance of low momentum tracks. Low momentum tracks tend to have a larger angle between the track and the thrust axis. This results in an effectively larger IP position error when finding the IP in the event (Figure 80).

The Monte Carlo simulation using a 30 micron Gaussian distribution to simulate the IP motion predicts 27±2.7 events tagged, based on the 29 found using the tag with an event IP. This algorithm tags 31, which is 1.5σ more than expected.

There are 3 events which are only tagged with the event IP, and 5 that are only found with a mean IP. The Monte Carlo predicted 3.1 and 2.3 respectively. R_b is found to be 0.265 using this method.

Tagging using the mean IP is very sensitive to a tail on the IP motion distribution. We were unable to put a useful limit on this tail in Section 4.3 because of the required sensitivity: a displacement of the IP at the 100 micron level will often result in enough significant tracks to tag the event. Motions of this magnitude in 6 events, 3% of the total, would result in a change in the measured R_b value of 10%. We are unable to rule this out.

We can also apply the difference tag approach of Section 5.4.2 with a mean IP. In that case, we tag 22 events. This corresponds to an R_b value of 0.246. The Monte Carlo prediction varies with its starting assumptions:

1. 23.6±2.3 if you assume the 31 events tagged by the mean IP significance algorithm,
2. 17.1±2.9 if you assume the 18 events tagged by the event IP difference algorithm,
3. and 20.5±2.2 assuming the 29 events tagged by the IP significance algorithm.

The largest discrepancy is 1.3σ, from comparing the two difference tagging algorithms. It is quite possible that the number of events tagged using the difference tag and the IP found in the event has fluctuated low by 3 events, which is 1.3σ.

To summarize, we have measured R_b using the IP found in the event as 0.230±0.049. The three modified tagging algorithms find R_b values of 0.183, 0.265, and 0.246 which are all within the quoted statistical error of our measurement.

5.4.4 A Tagged Event

Figure 81 shows a tagged event in the SSVD. A clear vertex is visible 1 cm from the IP on the upper left. All the tracks from this vertex have high significance, and would be sufficient to tag this event.

Not visible in Figure 81 is a much more typical vertex in the jet to the lower right.* Figure 82 shows an expanded view of this jet in the SSVD. The tracks

* The vertex at lower right that seems to contain three tracks and is well separated from the jet is spurious, as one of the tracks fails quality cuts (no SSVD hits). One of the remaining two tracks is consistent with the IP and the other is consistent with the vertex in the jet. These 'coincidental vertices' are quite common.

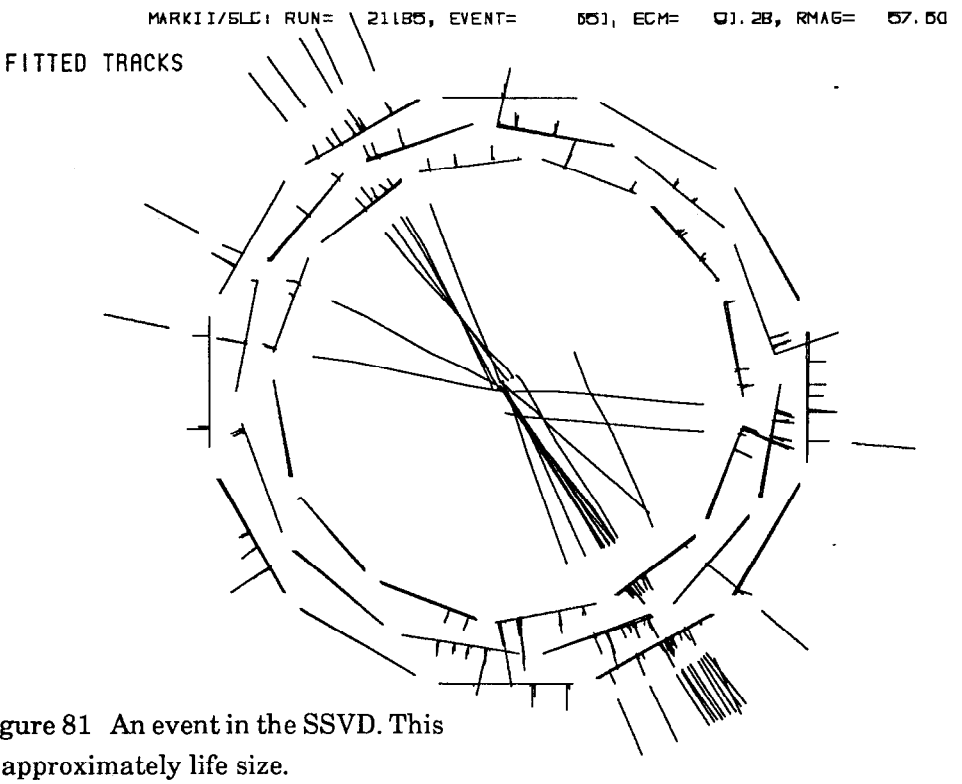

Figure 81 An event in the SSVD. This is approximately life size.

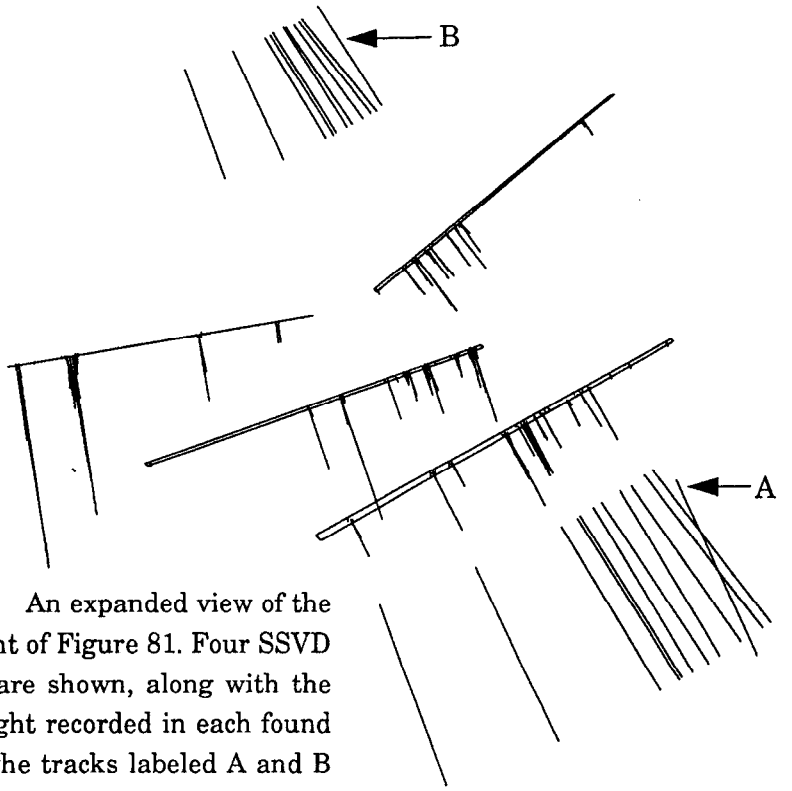

Figure 82 An expanded view of the lower right of Figure 81. Four SSVD modules are shown, along with the pulse height recorded in each found cluster. The tracks labeled A and B do not pass quality cuts.

labeled A and B are missing SSVD hits and do not pass quality cuts. The SSVD clusters are clearly separated.

Figure 83 is a very expanded view of this region. The eye sees a vertex candidate at (0.001, -0.005), but the exact structure of the event is impossible to determine. The decay length of this vertex is about 4 mm. Three tracks have $S > S_{min}$, so this vertex would also suffice to tag this event.

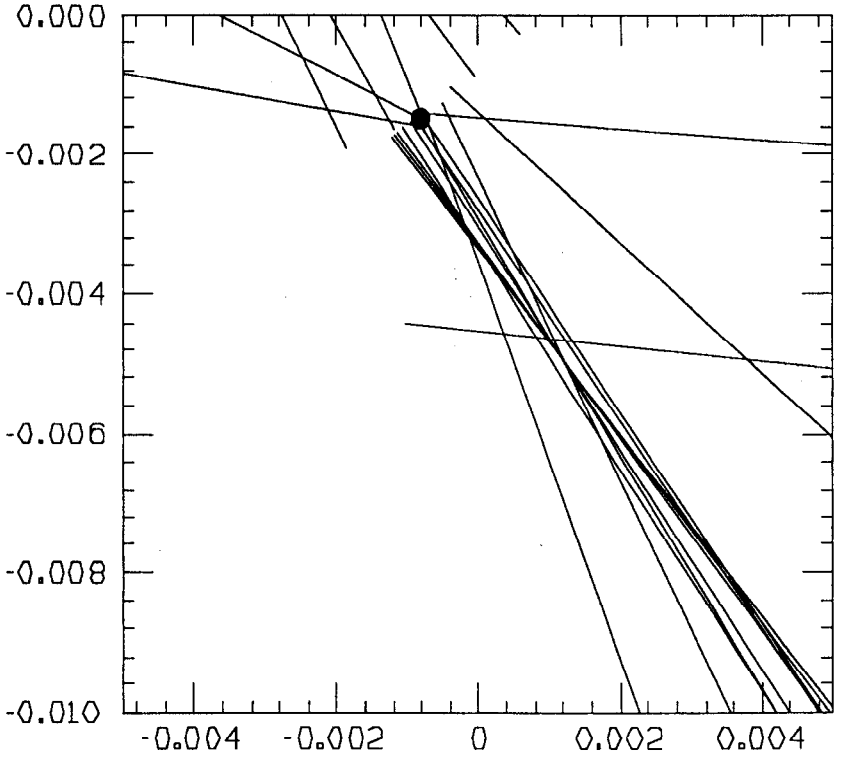

Figure 83 Expanded view of the region around the IP. The scales are in meters. Both the IP found in the event and mean IP lie well within the black dot. The track line width corresponds to 40 microns.

5.5 Systematic Errors

To calculate R_b, we need to find the tagging efficiencies ε_b, ε_{udsc}, s_b and s_{udsc} from the Monte Carlo. These values can have errors, which will effect our final value of R_b. These errors can come from sources such as insufficient Monte Carlo statistics, improper modeling of the tracking resolution and incorrect values of Monte Carlo physics parameters. In this section we will investigate possible sources of systematic error and the size of the uncertainty they introduce in the measurement of R_b.

We evaluate the effect on R_b of these sources of systematic error by adding each of them in turn to the Monte Carlo simulation. We then measure R_b in a sample of 20,000 events using the original values of the efficiencies ε_b and ε_{udsc}. The fractional change from the nominal R_b value of 0.220 is the systematic effect due to the source in question.

5.5.1 Tracking

In Chapter 4 we examined the performance of the tracking system. We were able to describe the range of possible defects in its resolution. We will now determine how our measurement of R_b varies within the permitted range.

5.5.1.1 Core and Tail Resolution

Table 10 on page 89 showed the χ^2 of the match between various smeared Monte Carlo simulations and the data. Table 19 shows the systematic change in R_b for each of those simulations. The double line surrounds the regions which have not been ruled out. The range of changes is -10% to +4%, which we take as the possible systematic error.

The change in the fraction of events tagged due to the presence of a larger tail comes from several sources:

1. Events with two tracks from B hadron decay can pick up an additional significant track from the tail of the tracking resolution function. This is linear in the tail fraction, and there are a large number of events with 2 significant tracks (Figure 78). This is the largest component of the change in R_b.
2. Events containing c quarks can pick up one or more additional tracks. This is the largest contribution to the background tags.
3. Events with three tracks can lose a track to the increased tail. As there are more events with two significant tracks than with three, this effect is noticeably smaller, but it does tend to reduce the systematic effect slightly.

Because our signal is a coincidence of significant tracks, in Chapter 4 we looked for an underlying physical variable which could cause the resolution tail to be correlated within an event. We found no such effect.

Should we have missed a real cause of correlated tracks in the resolution function tail, it might have an impact on our tagging efficiencies. We simulate this using two representative* causes:

1. The tail may be due to a tracking defect which exists in a certain section of the detector. Since events have tracks concentrated in jets, if all tracks through a 15% region of the detector were slightly mistracked we would introduce correlated errors into the tracking of events whose thrust axis points into the defective region.

   We simulate this by adding the 75 micron Gaussian smearing to all tracks in the 15% of the acceptance between $\phi = 0$ and $\phi = 3\pi/10$. It results in a 2% shift in the value of R_b from the result when the smearing is applied to 15% of tracks chosen randomly.

2. The cause could also be slightly more distributed. An example would be a defect in 15% of tracking region of each DCVD cell. We again simulate this by adding the 75 micron Gaussian smearing to tracks in the first 15% of each DCVD cell. This results in a 1% shift of the R_b result.

These differences are small, and are considered to be included in the systematic error from the uncertainty in the size of the tail.

5.5.1.2 Tracks With Very High Significance

There are several effects which can cause extra very high significance tracks. These include photon conversions, nuclear scattering, K^0 and Λ decays far from the origin, and track kinks from charged particle decays. All of these are included to various degrees of accuracy in the Monte Carlo, but the magnitude of their effects is somewhat uncertain.

In Section 4.1.5 we were able to place an upper limit of 0.2% of tracks having an excess normalized resolution of 20 or more. Adding this to the Monte Carlo increases R_b by 2%, which we take as the possible systematic error.

5.5.1.3 Tracking Efficiency

As shown in Section 4.2, the vertex detector tracking efficiency is modeled in the Monte Carlo simulation to better than 2%. By randomly removing tracks in the Monte Carlo with 2% and 5% probability, we find that R_b has a corresponding 2% and 5% change. Note that our knowledge of the efficiency would improve with more tracks, as we are limited in how well we can determine efficiency with less than 3,000 tracks. We will separately investigate multiplicity in Section 5.5.2.3 on page 122.

---

* Note that both of these specific causes have been ruled out by searches described in Chapter 4. They are used here only to capture the statistical correlations that a non-random source of tracking error may cause.

C = 0 microns	*F*, fraction in added tail					
M, tail excess error	0	5%	10%	15%	20%	25%
0	9%	9%	9%	9%	9%	9%
25	9%					
50	9%		7%	6%		
75	9%		3%	2%	-2%	-5%
100	9%		0%	-5%	-9%	-14%
150	9%			-15%		
200	9%					
300	9%					

C = 5 microns	*F*, fraction in added tail					
M, tail excess error	0	5%	10%	15%	20%	25%
0	8%	8%	8%	8%	8%	8%
25	8%					
50	8%	6%	7%	5%	4%	
75	8%		4%	0%	-3%	-7%
100	8%	4%	1%	-5%	-10%	-16%
150	8%	1%	-5%			
200	8%		-10%			
300	8%		-18%			

C = 10 microns	*F*, fraction in added tail					
M, tail excess error	0	5%	10%	15%	20%	25%
0	8%	8%	8%	8%	8%	8%
25	8%					
50	8%					
75	8%					
100	8%		-1%	-6%	-11%	
150	8%					
200	8%					
300	8%					

Table 19 Fractional changes in R_b from uncertainty in the required Monte Carlo smearing. The double line encloses the permitted range from Chapter 4. The variations range from -10% to +4%.

5.5.1.4 Material and Multiple Scattering

In Table 11 on page 92, we show that the core width for tracks of all momentum, which is dominated by multiple scattering, is known to about 2%. This statistical uncertainty translates into a 2% uncertainty in our model of the material in the detector.

We examined the effect of this uncertainty in two ways.

1. We changed all the material in the detector simulation by a uniform 2%.
2. We examined the effect in the Monte Carlo of varying just certain material layers in the detector. For example, instead of scaling all material up 2%, we increased the multiple scattering from the beampipe (normally a quarter of the total multiple scattering) by 8%.

The methods produced the same result. A 2% uncertainty in the material model for the detector, effectively in the width of the core normalized error for lower momentum tracks, causes a 4% systematic change in the measurement of R_b. This forms another systematic error which could be improved with more tracks.

5.5.2 Monte Carlo Input Parameters

We use the Monte Carlo simulation to determine the tagging efficiency and background. Some of the physics parameters used in this simulation are uncertain, and in this section we investigate the sensitivity of our result to these parameters.

5.5.2.1 Fragmentation

As described in Section 2.3 on page 44, the Monte Carlo models a fragmentation process which converts isolated b quarks into B hadrons. For our purposes the most important characteristic of this process is the momentum spectrum of the resulting B hadrons. This will effect the B hadron decay length, on which the impact parameter depends weakly as we have seen in Section 1.5.1. More important, the momentum of the decay particles is proportional to the B hadron momentum, and the tracking resolution is a strong function of particle momentum. Thus a higher momentum B hadron will have slightly smaller impact parameters but much improved tracking resolution, resulting in a net increase of track significance.

The Monte Carlo simulation assumes a B hadron momentum spectrum given by the Peterson[53] function. This has one free parameter, which can be written as the mean energy carried by B hadrons as a fraction of the beam energy

$$\langle x_b \rangle \equiv \langle E_B \rangle / E_{beam} . \quad (43)$$

This has been measured by ALEPH[72] as 0.67±0.04 and by L3[26] as 0.686±0.006±0.016. We use 0.68 for the Monte Carlo value. We reweight Monte Carlo b quark events to vary this mean by ±0.04 and find a change in R_b of -3% or +6%. The Peterson momentum spectrum is approximately maintained by this reweighting. We take this change in R_b as the systematic error.

If the correct distribution is very different from the Peterson function, especially if there is a large fraction of very low momentum B hadrons, our efficiency would be adversely affected. L3 has measured[26] the shape of the B hadron momentum spectrum from x_b = 0.2 to x_b = 1.0 and finds agreement. We do not assign a separate systematic error to the shape of the momentum spectrum.

5.5.2.2 B Hadron Lifetime

The average B hadron lifetime directly affects the impact parameter distribution without changing the tracking resolution, so it has a strong effect on track significance. The Particle Data Book[13] value for the average B hadron lifetime is 1.18±0.10 picoseconds. This is based on data from lower energies, and it is an open question as to whether the mix of B hadrons from Z^0 decays will have the same lifetime. ALEPH has recently measured[66] the average B hadron lifetime in Z^0 decays as 1.29±0.06±0.10 picoseconds. Their average is weighted by the B hadron semi-leptonic branching ratio.

We use 1.24 picoseconds, the unweighted average of these, as our central value in the Monte Carlo. We assume that all long-lived* hadrons containing b quarks have the same lifetime. We vary the mean lifetime for all B hadrons by ±0.12 picoseconds to find our systematic error, which is +7% and -4%.

The individual lifetimes of the B^0 and $B^{\pm}$ mesons have not been precisely measured, although an indirect measurement[73] of the lifetime ratio exists. The lifetime ratio is between 0.44 and 2.08 at the 90% confidence level.[13] We examined the effect of a possible lifetime difference by setting the B^0 lifetime to 0.62 psec, and

* An extremely short-lived component will have zero efficiency for tagging and will not appear in our value for R_b. B^* mesons, for example, decay before they can generate any impact parameter. We explicitly assume that all such short-lived B hadrons have a long-lived B hadron as one of their decay products.

the $B^{\pm}$ lifetime to 1.86 psec. This preserves the average, while giving a 3 to 1 ratio. The change in R_b was less than 2%. We do not quote this as a separate source of systematic error, as it is small compared to the lifetime uncertainty.

5.5.2.3 Multiplicity

There are three types of charged particle multiplicity which affect the measurement:

1. The number of charged tracks in background *udsc* quark events effects their probability of being tagged. We have investigated this by weighting the Monte Carlo events so as to change the mean multiplicity by ±1 track and the effect is entirely negligible.
2. The number of tracks from B hadron decays affects the probability of tagging a *b* quark event. Using CLEO[74] and ARGUS data, the mean decay multiplicity of 5.22 in our Monte Carlo compares well to their measurements of 5.27±0.10.* These numbers include tracks from tertiary D meson decays. There is still some uncertainty in the exact mix of B hadrons present at SLC energies, however, and we conservatively assign a ±3% systematic error based on the effect of a ±0.3 track change in the mean.
3. The number of fragmentation tracks from the IP in a *b* quark event can also effect the tagging efficiency. This is because the tracking resolution function non-Gaussian tail shows a finite probability for a track from the IP passing the significance cut. This charged particle multiplicity from the IP has not been independently measured. Further, our Monte Carlo event generator correlates fragmentation multiplicity with the B hadron energy. Using event weighting to vary this multiplicity by ±2 tracks gives a ±2% systematic error. Varying the multiplicity by ±2 tracks while leaving the mean B hadron energy unchanged results in a ±1% error, indicating that much of the effect comes from the B hadron energy change. We conservatively use the 2% figure.

These three classes are sufficiently independent that combining the errors in quadrature is appropriate. This gives us a 4% systematic error from charged track multiplicity uncertainty.

5.5.2.4 B Decay Kinematics

In addition to the charged track multiplicity of B hadron decays, the kinematic distributions in B hadron decays can conceivably affect tagging efficiency. The

* This was studied in detail by Bruce Schumm.

Monte Carlo normally decays a B hadron by converting the b quark to a u or c quark by coupling to a W boson. The remaining quark(s) of the B hadron are then combined with the u or c quark to form a single new hadron. The W boson is then decayed to leptons or quarks. Leptons are kept in the final state and the standard Lund fragmentation is used to form hadrons from the quarks.

To estimate the effect of uncertainty in the B decay kinematics, we generated two modified Monte Carlo samples. In the first, all the quarks in the decay are allowed to form hadrons via fragmentation. In the other, the final hadrons were given a uniform distribution in phase space. Event weighting was used to keep the mean, though not the RMS, multiplicity unchanged. These resulted in 3% and 4% changes in R_b respectively.

The Monte Carlo simulation also models the creation of B baryons during the fragmentation process. This is assumed to happen approximately 10% of the time. We varied this fraction to 30% while reweighting the multiplicity back to the standard value and found a change in R_b of 3%.

We estimate the systematic error from the uncertainty in our B decay models as 4%, and note that more detailed study of existing data should make it possible to place tighter limits on the model parameters.

5.5.2.5 Charm Fraction

The c quark fraction has been measured at the Z^0 by both ALEPH[23] and DELPHI.[75] Their consensus answer is 0.156±0.041. We use 0.170, the Standard Model value, in the Monte Carlo. We vary it by ±0.040 to find a change in R_b of 1%. We take this as the systematic error from the uncertainty in the charm fraction.

5.5.2.6 Secondary b Quark Production

In addition to direct production of b quarks in Z^0 decays, the Monte Carlo also produces b quarks later in the event simulation. They can be created from hard gluons radiated before hadronization, or from the 'string' used in the hadronization process. The large mass of the b quark causes these mechanisms to be very suppressed, but they can be present in events where the Z^0 decays into any type of quark, including b quarks. This has two effects. First, an event containing four b quarks is significantly more likely to be tagged than an event with two. Second, although an event with b quarks from secondary production is less likely to be tagged than an event containing directly produced b quarks, it still has an significant efficiency, namely about 0.2. The decreased efficiency is due to the lower momenta of the B hadrons, and thus the decreased tracking resolution for the decay

products, and the poor performance of the impact parameter signing algorithm because the thrust axis is not a good indicator of the B hadron flight direction.

We include these effects by defining ε_b and ε_{udsc} in terms of direct production from the Z^0 decay. The extra b quarks effect these efficiencies at the 0.5% level, but the effects compensate each other somewhat. Analyzing events with all secondary b quark events suppressed results in an R_b value shifted by 0.3%.

As there is some uncertainty in the correct amount of this secondary b quark production, we conservatively assign a systematic error of 1% to this source.

5.5.3 Monte Carlo Statistics

We calculated the tagging efficiencies ε_b, ε_{udsc}, s_b and s_{udsc} from the Monte Carlo using a sample of 20,000 generated events. For our N_{min}=3 S_{min}=3 tag, the largest effect on the result is from the combination of s_b and s_{udsc} to form Δ_ε which has a value of 0.030±0.015. The Monte Carlo statistical errors contribute a 2% fractional error on R_b which we treat as a systematic error.

5.5.4 Systematic Error Summary

Table 20 lists the systematic errors we have discussed. The sum in quadrature rounds up to 14%, which we take as the total systematic error. Of this, approximately half can be attributed to items that we would have been able to directly improve with better statistics.

5.6 Tagging Summary

We have used the precision tracking information to separate events containing b quarks in our data sample. We tag 29 events, of which we expect 24.6 to be signal and 4.4 to be background. From this, we compute

$$R_b = 0.230 \pm 0.049 \pm 0.032 \quad (44)$$

where the first error is statistical and the second is systematic.

Effect	Fractional Error
Core/Tail Tracking	-10% +4%
Far Tails	±2%
Tracking Efficiency	±2%
Material and Multiple Scattering	±4%
Fragmentation Model	-3% +6%
B Hadron Lifetime	-4% +7%
Multiplicity	±4%
B Decay Kinematics	±4%
Charm Fraction	±1%
Secondary b Production	±1%
Monte Carlo Statistics	±1%

Table 20 Summary of identified systematic errors.

The best way to predict the future is to invent it.

Alan Kay

6 Conclusions

We find that the precision tracking systems of the Mark II detector measure the impact parameter of high momentum tracks to better than 20 microns. We are able for the first time to use this precision tracking and the finite b quark lifetime to identify events containing b quarks with an expected 48% efficiency and 85% purity.

Of the 220 Z^0 decays passing hadronic identification cuts, 29 are selected by our tagging algorithm. We expect that 24.6 of these contain b quarks. Using the number selected, we have measured

$$R_b \equiv \frac{Br(Z^0 \to b\bar{b})}{Br(Z^0 \to hadrons)} = 0.230 \pm 0.048 \pm 0.030 \qquad (45)$$

where the first error is statistical and the second is systematic. This result is consistent with previous measurements and the Standard Model prediction of 0.22 given a $\sin^2\theta_w$ value of 0.225.

The largest systematic error contributions are due to the uncertainty of the tracking resolution, the B hadron lifetime, and the b quark fragmentation function, all of which can be studied using precision tracking and larger event samples. It is hoped that the systematic and statistical errors of an R_b measurement using precision tracking can be driven down to the 1% level, where it becomes a strong constraint on theory.

6.1 Observations

While studying the performance of the Mark II tracking system during the preparation of this dissertation, we came to a number of conclusions about the advantages and disadvantages of the design. In this section we discuss these observations, but it should be noted that we have not extensively studied alternatives to the Mark II design. It may be the case that alternatives that look quite desirable to us now have flaws that we have not yet discovered.

The Mark II precision tracking system consists of three concentric, independent trackers. Obtaining optimal performance required us to use all the information from all three systems on most tracks. This gives rise to difficulties because the impact parameter resolution is a complex function of momentum and track path. Multiple scattering causes the various track position measurements to receive different relative weights for different particle momenta (Figure 47 on page 52). Although in principle this effect can be exactly calculated, it increases the sensitivity of the tracking algorithms to the exact values of material thicknesses, measurement resolutions of individual hits, and relative alignments of the detectors. It was particularly unfortunate that the momentum at which the three detectors are all making approximately equal contributions (about 2 GeV/c) is also the region of most interest in this measurement. It would seem that a system without this complexity would be preferred, and two alternatives are possible:

1. The inner silicon tracker has a large enough interlayer spacing that it can measure both track position and angle to the desired accuracy. Curvature (momentum) could then be separately measured by an outer tracker.* This implies a large, multi-layer detector.

   The loss of performance due to missing areas of the silicon detector should be carefully considered. Coverage can be lost due to gaps in the original design, failed modules, individual bad channels, and other causes. A two-layer detector which has lost its ability to measure the angle of certain tracks due to missing hits again must rely on the precision of the outer tracker. Provision for realistic losses would seem to imply that three layers is a minimum to avoid reliance on the precision of the outer tracker.

---

* The outer tracker must measure the track position and angle well enough to ensure the correct match between hits and tracks.

2. The multiple scattering in the inner silicon tracker is sufficiently small that an outer tracker can accurately measure the track angle for all momenta of interest. This implies a small, single layer detector.

   Aligning a system of this type using tracks requires the outer detector be extremely precise. Track matching without ambiguity also requires the outer tracker have very good resolution. The modules would have to be reliable as there is no redundant information available. In all, this alternative seems to offer little advantage over a high precision detector similar to the Mark II DCVD.

The Mark II design was intermediate between these two alternatives.

The detector alignment was difficult to determine to the required precision. This includes the relative alignment of the detector systems, plus the internal positions of the SSVD and DCVD elements. The systematic position error, whether due to alignment or other sources, of all the tracking systems must be quite small for the alignment procedure using tracks alone to succeed. This is because track-based alignment in a silicon detector is a very local operation, which is capable of adjusting to, and thus adopting, many systematic errors in the track parameters used for alignment. This is true of silicon vertex detectors with one, two or three layers, although a three layer detector has some limited ability to check for systematic position errors in the outer chambers (Section 3.6.5 on page 68).

It is possible to quantitatively study the alignment sensitivity of a particular detector geometry without excessive Monte Carlo simulation. This can be done by setting up the least squares equations for aligning the desired detector module geometry and solving for the resulting covariance matrix. The eigenvectors and eigenvalues of this matrix then represent the 'normal modes' of motion of the detector elements and how well they are constrained. Numerical studies of this type were used to select the alignment procedure described in Section 3.6. We recommend an exercise of this type be done early in the design of precision trackers to estimate their likely alignment accuracy.

Finally, we found that the non-Gaussian tails on the resolution function due to Coulomb scattering cannot be ignored. This is because of the large difference in thickness (in radiation length units) of silicon detectors and gas chamber cells. Properly including the Moliere model of scattering from non-uniform material was an important step in making our Monte Carlo simulation agree with the data.

If I take refuge in ambiguity, I assure you that it's quite conscious.

Kingman Brewster, Jr.

A Tracking Resolution in Pictures

In this appendix, we develop a simple model relating measurement and tracking resolution. By using a graphical representation of the measurement's resolution, we'll try to understand their individual contributions to the track resolution.

In two dimensions and ignoring curvature, the covariance matrix of the track parameters at the IP can be written as

$$\begin{bmatrix} \sigma_{BB}^2 + R^2\sigma_{\phi\phi}^2 & R\sigma_{\phi\phi}^2 \\ R\sigma_{\phi\phi}^2 & \sigma_{\phi\phi}^2 \end{bmatrix} \tag{46}$$

where $\sigma_{\phi\phi}$ is the angle measurement, σ_{BB} is the track position measurement at its best, typically inside the tracking detector*, and R is the distance from this best measurement to the IP where the track parameters and errors are wanted. The track can be thought of as being inside a hyperbolic 'envelope' as in Figure 84.

A single point measurement, such as a hit in a single SSVD layer, is a special case where σ_{BB} is small but $\sigma_{\phi\phi}$ is infinite. The other extreme, a measurement of only angle, has a small $\sigma_{\phi\phi}$ and large σ_{BB}. Unfortunately, these common cases are difficult to draw as hyperbolas. In the case of no B information at all, we would have to draw two parallel lines infinitely far apart, hardly a useful picture.

---

* The double subscript notation is used for $\sigma_{\phi\phi}$ and σ_{BB} to allow later definition of $\sigma_{B\phi}^2$ as the upper right element in a similar matrix. The capital B is used to avoid confusion with σ_{bb}, the track position resolution at the IP.

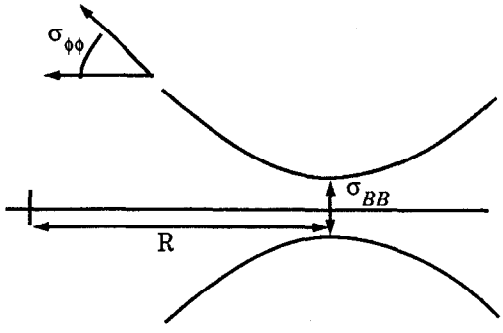

Figure 84 A measurement hyperbola.

We can borrow a different picture from beam optics. These hyperbolas look like a beam envelope, and it is common to represent these as an ellipse in angle-position 'phase space'. Figure 85 shows the same track measurement this way. In this scheme, the ellipse is upright when the track parameters and errors are stated at the point where is the track position information is best, i. e. when R is zero. As R is increased, the ellipse shears to the left (see Figure 86). This increases the vertical projection, which corresponds to the position measurement at the IP, without changing the horizontal projection, the angular measurement.

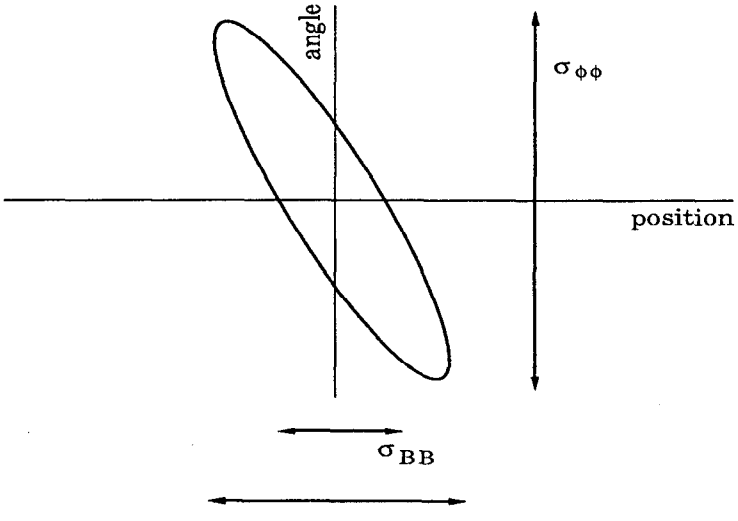

Figure 85 The same measurement as an ellipse in an angle - position space.

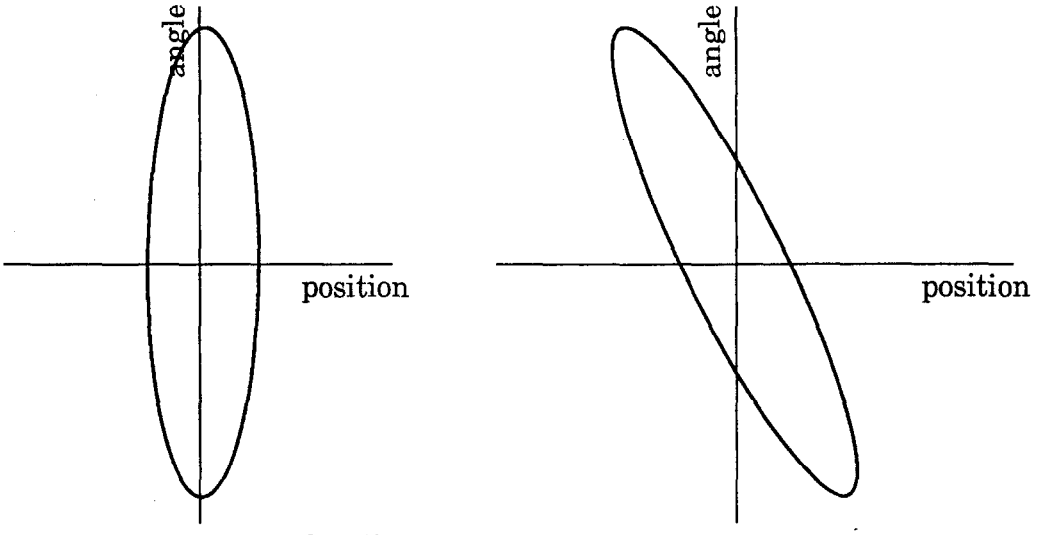

Figure 86 The effect of measuring a track away from the IP. The left ellipse states the track errors inside the tracker (R=0), while the right ellipse is stated at a distant IP.

Multiple scattering acts to degrade angular information at the scattering radius. When a track goes through material, $\sigma^2_{\phi\phi} \rightarrow \sigma^2_{\phi\phi} + \sigma^2_{\text{scattering}}$ which stretches the ellipse vertically. Note that this is different from the shearing caused by transferring to a different point. Figure 87 contrasts these - note that although the projection of each ellipse has been doubled in position or angle respectively, the effects on the correlation and axis crossing are very different.

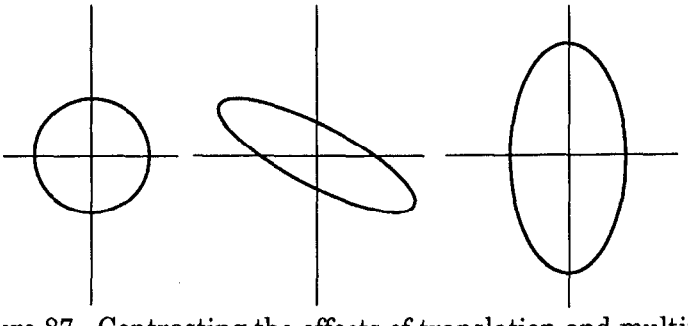

Figure 87 Contrasting the effects of translation and multiple scattering. The left ellipse is the original measurement. The center ellipse has been sheared by translation to the IP, while the right ellipse has been rescaled by multiple scattering.

A real position measurement must be propagated to the IP to be useful. This can involve both translation and multiple scattering at different places. Figure 88 shows how to picture this - start with the measurement in the tracker. Restate it at

the material, which shears the ellipse and degrades the position information, but leaves the angle alone. Add the material by stretching the ellipse vertically, then again shear the ellipse to finally state the track errors at the IP.

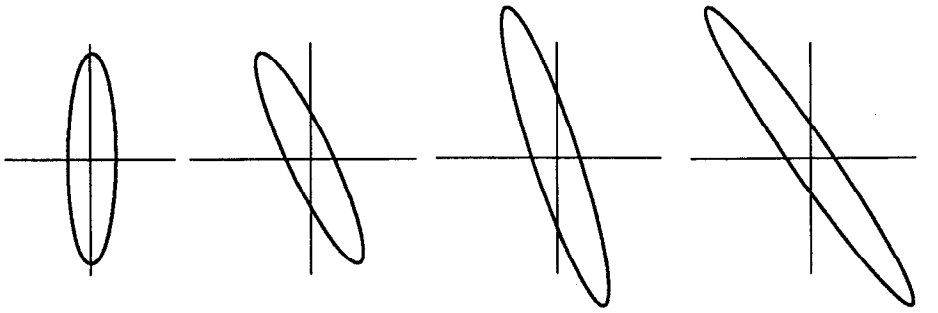

Figure 88 Adding multiple scattering. From the left, these are the measurement error in the tracker, stated at the material, after the angular scattering is added, and finally stated at the

We combine measurements by overlaying the ellipses of each. In the simple case of two point measurements (Figure 89), the final measurement is then the largest ellipse that can be drawn entirely inside the measurement ellipses. In more complex cases, the largest ellipse gives an approximation, although not always the size, of the result. As can be seen in this example, the separation between the two measurement positions, which becomes the angular spread between them in this plot, is critical to the resolution.

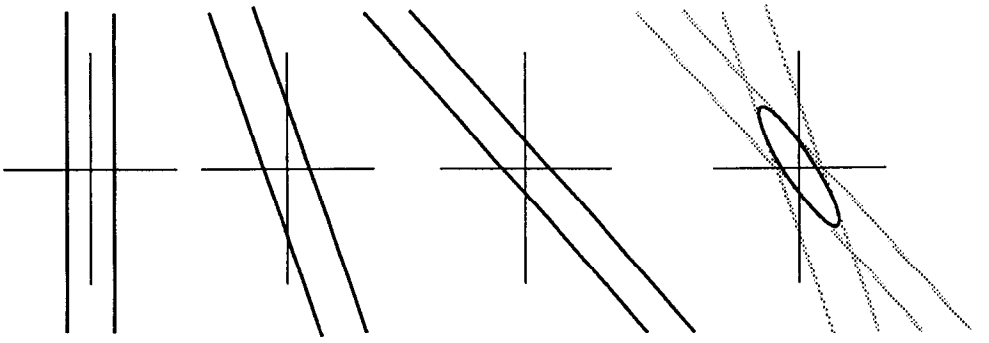

Figure 89 Combining two position measurements into a track measurement. Two position measurements (left) individually give no angular information. After transferring to the IP, they individually give no limit on impact parameter (center plots). Combining the two, however, gives an ellipse limiting both position and angle.

Figure 90 and Figure 91 show two representative cases in the Mark II tracking system. At 5 GeV/c, the two measurements on this track in the SSVD are still too degenerate to contribute, so the angular limit comes from the DCVD/CDC information. At 500 MeV/c, however, multiple scattering has decreased the accuracy of the DCVD/CDC angular limit to irrelevancy, so the SSVD hit separation becomes the limit to the measurement.

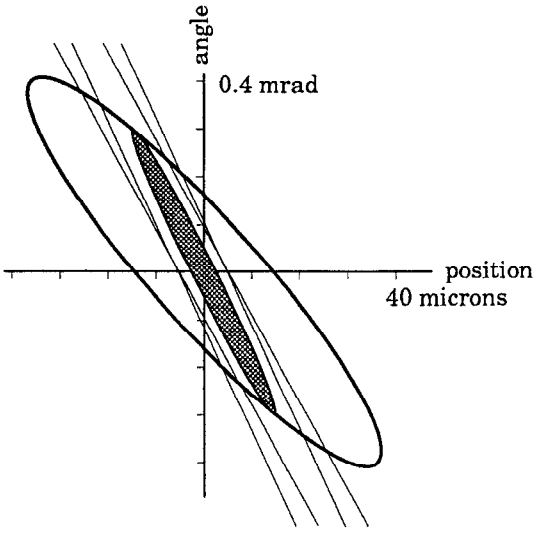

Figure 90 A Mark II track measurement at 5 GeV/c. The ellipse is the CDC/DCVD measurement, which constrains the angle of the track. This limits the projection of the SSVD information (the two bands) and improves the measurement.

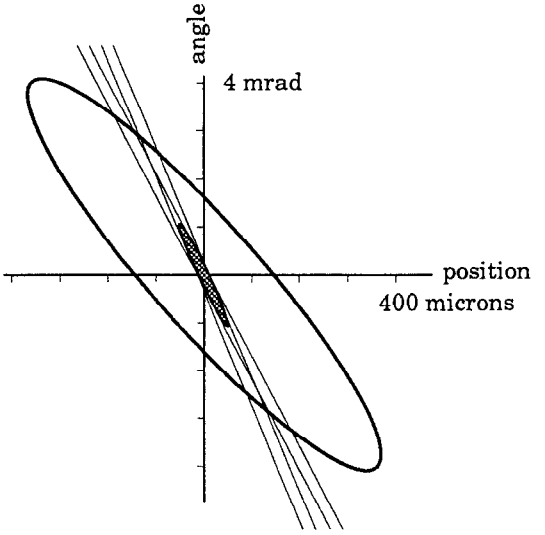

Figure 91 A Mark II measurement at 500 MeV/c. The two SSVD hits provide essentially all the information. Note that the scales have changed by a factor of 10 from Figure 90.

Just as these pictures are borrowed from beam optics, we can also borrow a matrix formalism. In it, a measurement is represented by a matrix M (46), and there are three useful transformations:

1. Translating a measurement to a new position a distance R away is done by defining a translation matrix

$$T \equiv \begin{bmatrix} 1 & R \\ 0 & 1 \end{bmatrix} \tag{47}$$

which generates the transformation

$$M \rightarrow TMT^T. \tag{48}$$

2. Multiple scattering adds to the $\sigma_{\phi\phi}$ component:

$$M \rightarrow \begin{bmatrix} \sigma_{BB}^2 + R^2\sigma_{\phi\phi}^2 & R\sigma_{\phi\phi}^2 \\ R\sigma_{\phi\phi}^2 & \sigma_{\phi\phi}^2 + \sigma_{\text{scatter}}^2 \end{bmatrix} = \begin{bmatrix} 0 & 0 \\ 0 & \sigma_{\text{scatter}}^2 \end{bmatrix} + M \tag{49}$$

where the scattering contribution is calculated from the material and the particle momentum.

3. Combining measurements is by addition of inverses:

$$M_1 \oplus M_2 \rightarrow (M_1^{-1} + M_2^{-1})^{-1} \equiv M_{1+2}. \tag{50}$$

The formalism can also be extended to include curvature (momentum) by adding a third row and column to the matrices, etc. The result would be a method of exactly combining all the individual track measurements by a series of matrix multiplications and additions. This goes beyond our goal of building intuition, however, and the formalism we develop in Appendix B is better suited for exact tracking calculations.

It is the nature of all greatness not to be exact.

Edmund Burke 1774

B The Mathematics of Precision Tracking

In this Appendix we outline the equations used by the SSVD track reconstruction. We restrict the discussion to the xy plane to simplify the notation, although the actual SSVD tracking is done in three dimensions. The computer routines which implement these equations are not described here.*

A track is characterized by impact parameter b, angle ϕ, and curvature k where the values are stated at the origin of the tracking coordinate system. The first two are conventionally signed as indicated in Figure 92. Together these can be written as a three-element track vector. To find best values for these quantities using the full system (V), we will fit to values from the outer tracker (O) and one to three SSVD hits. We know the resolution and position of each SSVD hit, the track momentum for calculating multiple scattering angle distributions and the covariance matrix (C) of the track parameters (v) measured in the outer chamber. C is determined by the CDC and DCVD tracking without including the effects of material in the SSVD and beampipe.

---

* Accuracy of computer floating-point calculations is extremely difficult to ensure or even quantify.[76] The calculational accuracy of the code was studied in depth, but the details of those results are beyond the scope of this dissertation.

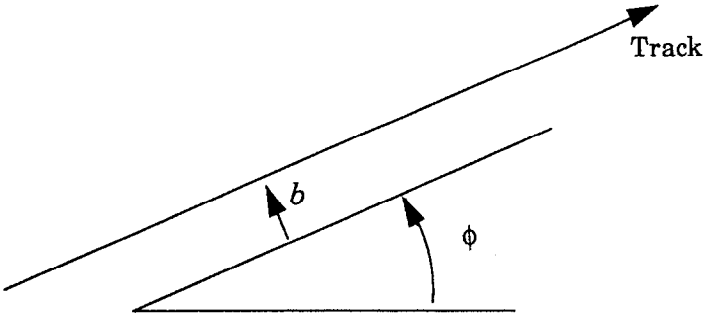

Figure 92 Track parameter sign conventions. The arrows point in the direction of increasing values.

To derive the fit equations, we first examine the case of no multiple scattering. To define x_i as the signed distance between the SSVD hit* in layer i and the track at closest approach, we can write

$$x_i \equiv S_i - S(i, V) \tag{51}$$

where S denotes a distance around the circumference of the detector, S_i is the position of the layer i hit and $S(i, V)$ is the calculated position of the track at the same radius using track parameters V.

In the absence of multiple scattering, the hits are uncorrelated and we can define

$$\chi^2 \equiv \sum_{\text{hits}} \left(\frac{x_i}{\sigma_i}\right)^2 + (V - v)\, C^{-1} (V - v)^T \tag{52}$$

where the second term is the contribution due to the measurement of the track parameters in the outer tracker.

* There may be less than three SSVD hits, in which case we omit the obvious rows and columns of the matrices being derived here.

We can write this as a matrix equation by defining a vector of measurements

$$X = \left[x_1 \quad x_2 \quad x_3 \quad V_b - v_b \quad V_\phi - v_\phi \quad V_k - v_k \right], \tag{53}$$

where v_b, for example, is the impact parameter (b) element of the vector of track parameters (v) measured in the outer trackers. Then Equation (52) is

$$\chi^2 = X \begin{bmatrix} \sigma_1^2 & & & & \\ & \sigma_2^2 & & & \\ & & \sigma_3^2 & & \\ \hline & & & C & \end{bmatrix}^{-1} X^T \tag{54}$$

where the covariance matrix C occupies a 3x3 submatrix in the lower right corner. The optimal values of the components of X are found by minimizing χ^2 with the usual least squares technique.

Multiple scattering correlates the SSVD hits at larger radii (Figure 93). The i^{th} and j^{th} SSVD hits are correlated by

$$\sigma_{ij}^2 = \sigma_\phi^2 (r_i - r_s)(r_j - r_s) \tag{55}$$

where σ_ϕ is the multiple scattering angle, defined in Section 3.1.1 on page 50, r_s is the radius of the scattering material, and r_i and r_j are the radii of the i^{th} and j^{th} SSVD layers.

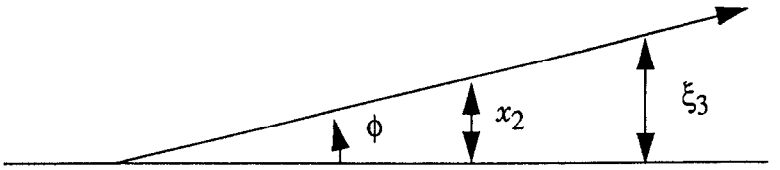

Figure 93 Correlations among SSVD hits due to scattering through an angle ϕ.

Appendix B

Scattering layers produce similar correlations between SSVD hits and the angle measurement in the outer tracker

$$\sigma^2_{i\phi} = \sigma^2_{\phi}(r_i - r_s), \tag{56}$$

between the SSVD hits and the impact parameter measurement in the outer tracker

$$\sigma^2_{ib} = \sigma^2_{\phi}(r_i - r_s) r_s, \tag{57}$$

and between the impact parameter and angle measured in the outer tracker

$$\sigma^2_{b\phi} = \sigma^2_{\phi}(r_i - r_s)\,(r_j - r_s). \tag{58}$$

There are also the contributions to σ^2_{bb} and $\sigma^2_{\phi\phi}$ discussed in Chapter 3.

All these terms are included by iterating over each layer of material and adding the contributions of each to Equation (54). This is practical because there are a managable number of SSVD layers - a different technique is appropriate for wire chambers with a large number of measurements separated by small amounts of scattering material. The χ^2 is then given by

$$\chi^2 = X \left[\begin{array}{ccc:cc} \sigma_1^2 & \sum_{r_s \geq r_2} (\sigma_\phi)_s (r_1 - r_s)(r_2 - r_s) & \sum_{r_s \geq r_3} (\sigma_\phi)_s (r_1 - r_s)(r_3 - r_s) & \sum_{r_s \geq r_1} (\sigma_\phi)_s (r_1 - r_s) & \sum_{r_s \geq r_1} (\sigma_\phi)_s (r_1 - r_s) r_s & 0 \\ & \sigma_2^2 & \sum_{r_s \geq r_3} (\sigma_\phi)_s (r_2 - r_s)(r_3 - r_s) & \sum_{r_s \geq r_2} (\sigma_\phi)_s (r_2 - r_s) & \sum_{r_s \geq r_2} (\sigma_\phi)_s (r_2 - r_s) r_s & 0 \\ & & \sigma_3^2 & \sum_{r_s \geq r_3} (\sigma_\phi)_s (r_3 - r_s) & \sum_{r_s \geq r_3} (\sigma_\phi)_s (r_3 - r_s) r_s & 0 \\ \hdashline & & & & C' & \end{array}\right]^{-1} X^T \tag{59}$$

where we have only shown the terms in the upper half, and the sums run over all material layers satisfying the condition on radius. C' is the covariance matrix of the outer tracker measurement including all multiple scattering material in the SSVD and beampipe.

These equations can then be solved for the track parameters (V) by noting that all the elements of X depend on the track parameters V, either explicitly or through the projected track position $S(i,V)$ which is used in the definition of x_i.

With three parameters I can fit an elephant.

Lord Kelvin

C Tracking Resolution Tables

In Section 4.1.3 on page 81 we examined the tracking resolution by comparison with a number of differently modified Monte Carlos. In this Appendix we record the complete results of those fits.

Table 21 through Table 23 list the three fit variables σ, λ and α for various combinations of Monte Carlo smearing parameters C, F and M. Each table contains the results of fitting the Monte Carlo normalized error after smearing with different tail exponential lengths M and fractions F. The Gaussian smearing C applied to the core is kept constant in each of these tables. Only high precision tracks with a calculated resolution better than 25 microns are included in the Monte Carlo distributions to be fit.

Table 24 through Table 26 again list the fit variables versus smearing parameters, this time for all tracks (including the high precision tracks included in the earlier tables).

σ	data = 1.10±0.034	*F*, fraction in added tail				
M, tail excess error	0	5%	10%	15%	20%	25%
0	1.03	1.03	1.03	1.03	1.03	1.03
25	1.03		1.00	1.12	1.15	
50	1.03	1.06	1.09	1.13	1.17	1.22
75	1.03	1.06	1.07	1.08	1.09	1.11
100	1.03	1.05	1.06	1.05	1.07	1.07
150	1.03		1.06	1.05	1.08	
200	1.03					
300	1.03					

λ	data = 3.14±0.29	*F*, fraction in added tail				
M, tail excess error	0	5%	10%	15%	20%	25%
0	4.26	4.26	4.26	4.26	4.26	4.26
25	4.26		4.01	4.29	4.34	
50	4.26	3.75	3.44	3.35	3.36	3.30
75	4.26	3.70	3.34	3.15	2.97	2.95
100	4.26	3.84	3.43	3.08	3.47	3.36
150	4.26		4.55	4.42	4.52	
200	4.26					
300	4.26					

α	data = 0.173±0.032	*F*, fraction in added tail				
M, tail excess error	0	5%	10%	15%	20%	25%
0	0.077	0.077	0.077	0.077	0.077	0.077
25	0.077		0.080	0.079	0.077	
50	0.077	0.090	0.109	0.120	0.129	0.142
75	0.077	0.102	0.133	0.164	0.205	0.236
100	0.077	0.106	0.146	0.192	0.206	0.254
150	0.077		0.135	0.179	0.207	
200	0.077					
300	0.077					

Table 21 Fit results for Monte Carlo with no additional core smearing *C*, high precision tracks only. The three sections are for the Gaussian width σ, the tail length λ, and the fraction of tracks in the tail α respectively.

σ	data = 1.10±0.034	*F*, fraction in added tail					
		0	5%	10%	15%	20%	25%
M, tail excess error	0	1.09	1.09	1.09	1.09	1.09	1.09
	25	1.09					
	50	1.09	1.10	1.12	1.16	1.19	1.23
	75	1.09	1.08	1.08	1.11	1.15	1.16
	100	1.09	1.09	1.07	1.08	1.10	1.11
	150	1.09		1.08	1.09	1.11	1.09
	200	1.09					
	300	1.09					

λ	data = 3.14±0.29	*F*, fraction in added tail					
		0	5%	10%	15%	20%	25%
M, tail excess error	0	3.98	3.98	3.98	3.98	3.98	3.98
	25	3.98					
	50	3.98	4.05	3.57	3.56	3.54	3.35
	75	3.98	3.89	3.26	3.27	3.18	3.08
	100	3.98	4.16	3.78	3.49	3.43	3.32
	150	3.98		4.13	4.47	4.33	4.53
	200	3.98					
	300	3.98					

α	data = 0.173±0.032	*F*, fraction in added tail					
		0	5%	10%	15%	20%	25%
M, tail excess error	0	0.061	0.061	0.061	0.061	0.061	0.061
	25	0.061					
	50	0.061	0.083	0.100	0.108	0.120	0.134
	75	0.061	0.096	0.137	0.158	0.189	0.218
	100	0.061	0.100	0.136	0.180	0.211	0.254
	150	0.061		0.144	0.174	0.210	0.244
	200	0.061					
	300	0.061					

Table 22 Fit results for Monte Carlo with 5 micron additional core smearing *C*, high precision tracks only. The three sections are for the Gaussian width σ, the tail length λ, and the fraction of tracks in the tail α respectively.

σ	data = 1.10±0.034	F, fraction in added tail				
M, tail excess error	0	5%	10%	15%	20%	25%
0	1.14	1.14	1.14	1.14	1.14	1.14
25	1.14					
50	1.14		1.18	1.21	1.22	
75	1.14		1.16	1.18	1.20	
100	1.14		1.16	1.17	1.14	1.15
150	1.14				1.15	
200	1.14	1.15	1.16		1.17	
300	1.14					

λ	data = 3.14±0.29	F, fraction in added tail				
M, tail excess error	0	5%	10%	15%	20%	25%
0	4.60	4.60	4.60	4.60	4.60	4.60
25	4.60					
50	4.60		3.80	3.54	3.32	
75	4.60		3.58	3.48	3.28	
100	4.60		3.91	3.73	3.55	3.40
150	4.60				4.47	
200	4.60	5.39	5.64		5.97	
300	4.60					

α	data = 0.173±0.032	F, fraction in added tail				
M, tail excess error	0	5%	10%	15%	20%	25%
0	0.074	0.074	0.074	0.074	0.074	0.074
25	0.074					
50	0.074		0.097	0.072	0.133	
75	0.074		0.127	0.148	0.184	
100	0.074		0.129	0.165	0.211	0.256
150	0.074				0.214	
200	0.074	0.098	0.130		0.194	
300	0.074					

Table 23 Fit results for Monte Carlo with 10 micron additional core smearing C, high precision tracks only. The three sections are for the Gaussian width σ, the tail length λ, and the fraction of tracks in the tail α respectively.

σ	data = 1.17±0.02	F, fraction in added tail					
		0	5%	10%	15%	20%	25%
M, tail excess error	0	1.11	1.11	1.11	1.11	1.11	1.11
	25	1.11		1.13	1.14	1.15	
	50	1.11	1.12	1.14	1.16	1.18	1.20
	75	1.11	1.13	1.14	1.16	1.18	1.20
	100	1.11	1.12	1.14	1.14	1.17	1.19
	150	1.11		1.13	1.14	1.16	
	200	1.11					
	300	1.11					

λ	data = 3.66±0.30	F, fraction in added tail					
		0	5%	10%	15%	20%	25%
M, tail excess error	0	4.10	4.10	4.10	4.10	4.10	4.10
	25	4.10		4.28	4.21	4.26	
	50	4.10	4.07	3.94	3.66	3.62	3.58
	75	4.10	3.94	3.49	3.39	3.27	3.16
	100	4.10	3.85	3.51	3.24	3.20	3.10
	150	4.10		3.64	3.56	3.50	
	200	4.10					
	300	4.10					

α	data = 0.087±0.015	F, fraction in added tail					
		0	5%	10%	15%	20%	25%
M, tail excess error	0	0.061	0.061	0.061	0.061	0.061	0.061
	25	0.061		0.061	0.062	0.062	
	50	0.061	0.065	0.069	0.076	0.079	0.082
	75	0.061	0.070	0.086	0.094	0.105	0.118
	100	0.061	0.076	0.095	0.117	0.129	0.150
	150	0.061		0.109	0.134	0.158	
	200	0.061					
	300	0.061					

Table 24 Fit results for Monte Carlo with no additional core smearing C, all tracks. The three sections are for the Gaussian width σ, the tail length λ, and the fraction of tracks in the tail α respectively.

σ	data = 1.17±0.02	F, fraction in added tail				
M, tail excess error	0	5%	10%	15%	20%	25%
0	1.13	1.13	1.13	1.13	1.13	1.13
25	1.13					
50	1.13	1.13	1.15	1.17	1.19	1.21
75	1.13	1.14	1.14	1.16	1.19	1.21
100	1.13	1.13	1.14	1.14	1.17	1.19
150	1.13		1.14	1.15	1.16	1.19
200	1.13					
300	1.13					

λ	data = 3.66±0.30	F, fraction in added tail				
M, tail excess error	0	5%	10%	15%	20%	25%
0	4.22	4.22	4.22	4.22	4.22	4.22
25	4.22					
50	4.22	4.06	3.86	3.76	3.70	3.64
75	4.22	3.93	3.49	3.39	3.31	3.21
100	4.22	3.87	3.52	3.15	3.60	3.08
150	4.22		3.61	3.57	3.44	3.45
200	4.22					
300	4.22					

α	data = 0.087±0.015	F, fraction in added tail				
M, tail excess error	0	5%	10%	15%	20%	25%
0	0.061	0.061	0.061	0.061	0.061	0.061
25	0.061					
50	0.061	0.065	0.069	0.073	0.077	0.080
75	0.061	0.070	0.087	0.094	0.103	0.115
100	0.061	0.076	0.093	0.121	0.131	0.153
150	0.061		0.109	0.132	0.161	0.181
200	0.061					
300	0.061					

Table 25 Fit results for Monte Carlo with 5 micron additional core smearing C, all tracks. The three sections are for the Gaussian width σ, the tail length λ, and the fraction of tracks in the tail α respectively.

σ	data = 1.17±0.02	*F*, fraction in added tail					
		0	5%	10%	15%	20%	25%
M, tail excess error	0	1.14	1.14	1.14	1.14	1.14	1.14
	25	1.14					
	50	1.14		1.17	1.18	1.20	
	75	1.14		1.17	1.19	1.21	
	100	1.14		1.17	1.18	1.20	1.22
	150	1.14				1.19	
	200	1.14	1.14	1.15		1.18	
	300	1.14					

λ	data = 3.66±0.30	*F*, fraction in added tail					
		0	5%	10%	15%	20%	20%
M, tail excess error	0	4.21	4.21	4.21	4.21	4.21	4.21
	25	4.21					
	50	4.21		3.92	3.90	3.59	
	75	4.21		3.74	3.52	3.39	
	100	4.21		3.62	3.41	3.26	3.12
	150	4.21				3.50	
	200	4.21	4.07	4.00		4.02	
	300	4.21					

α	data = 0.087±0.015	*F*, fraction in added tail					
		0	5%	10%	15%	20%	25%
M, tail excess error	0	0.062	0.062	0.062	0.062	0.062	0.062
	25	0.062					
	50	0.062		0.068	0.111	0.080	
	75	0.062		0.079	0.091	0.100	
	100	0.062		0.089	0.109	0.127	0.151
	150	0.062				0.158	
	200	0.062	0.087	0.115		0.180	
	300	0.062					

Table 26 Fit results for Monte Carlo with 10 micron additional core smearing *C*, all tracks. The three sections are for the Gaussian width σ, the tail length λ, and the fraction of tracks in the tail α respectively.

If your only tool is a hammer, all your problems tend to look like nails.

Unknown

References

[1] Fundamental Particles and Interactions Chart Committee, W. T. Achor, et al., "Fundamental Particles and Interactions: A Wall Chart of Modern Physics", Physics Teacher, pp. 556-565, Dec 1988, SLAC-PUB-4796

[2] Fundamental Particles and Interactions Chart Committee, H. R. Quinn, et al., "Teacher's Resource Book on Fundamental Particles and Interactions", LBL-26669-mc (microfiche), to accompany reference [2]

[3] F. Halzen and A. Martin, "Quarks & Leptons: An Introductory Course in Modern Particle Physics", John Wiley and Sons, New York, 1984.

[4] P. Collins, et al., "Particle Physics and Cosmology", John Wiley and Sons, New York, 1989.

[5] J. Dorfan, "Future Frontiers for e+ e– Collisions: Physics of SLC and LEP", lectures given at the Lake Louise Winter Institute on New Frontier in Particle Physics, Lake Louise, Canada, February 1986, SLAC-PUB-3928

[6] J. Dorfan, "Z Physics at the SLC", Lectures at Banff Summer Inst., Aug 1988 and NATO ASI on Techniques and Concepts of High Energy Physics, St. Croix V.I., July, 1988. Published in St. Croix ASI 1988:117 (QCD161:N15:1988) SLAC-PUB-4816

[7] M. Kobayashi and T. Maskawa, "CP Violation in the Renormalizable Theory of Weak Interaction", Progress of Theoretical Physics **49** p. 652 (1973)

[8] B. Flaugher and K. Meier, "A Compilation of Jet Finding Algorithms", FERMILAB-Conf-90/248-E, to be published in the proceedings of the 1990 Summer Study on High Energy Physics, Snowmass, CO, June 1990

[9] S. Weinberg, "A Model of Leptons", Phys. Rev. Lett. **19**, 1264 (1967)

[10] S. L. Glashow, "Partial-Symmetries of Weak Interactions", Nucl.Phys. **22**, 579 (1961)

References

[11] A. Salam and J. C. Ward, "Electromagnetic and Weak Interactions", Phys. Lett. **13**, 168 (1964)

[12] R. P. Feynmann, "QED: The Strange Theory of Light and Matter", Princeton Univ. Press, Princeton, N. J., 1985

[13] M. Aguilar-Benitez, et al. (The Particle Data Group), "Review of Particle Properties", Physics Letters **B239** April 1990.

[14] W. Brown, "Quantum theorists hit the boredom threshold", New Scientist, 16 February 1991, p. 23

[15] D. C. Kennedy and B. W. Lynn, "Electroweak Radiative Corrections with an Effective Lagrangian: Four-Fermion Processes", Nuc. Phys. B322 1,1989 SLAC-PUB-4039 (Rev)

[16] B. W. Lynn and R. G. Stuart, "Electroweak radiative corrections to b-quark production", Phys. Lett. B. 252 **4**, pp. 676 - 682

[17] M. Boulware and D. Finnell, "Radiative Corrections to BR(Z→bb) in the Minimal Supersymmetric Standard Model", SLAC-PUB-5519, April 1991, submitted to Phys. Rev. D.

[18] G. Alterelli, et al., "Physics at LEP", CERN 89-08 (1989)

[19] R. Cahn, "Z Decays and Tests of the Standard Model", lectures at the 1990 SLAC Summer Institute, LBL-29604

[20] L. Susskind, "Dynamics of Spontaneous Symmetry Breaking in the Weinberg-Salam Theory", Phys. Rev. D **20**, 2619 (1979)

[21] S. L. Wu, in 1987 International Symposium of Lepton and Photon Interactions at High Energies, North-Holland, Amsterdam (1987) p 39-133.

[22] The DELPHI Collaboration, "A Measurement of the Partial Width of the Z Boson into b Quark Pairs", CERN-PPE/90-118, Contributed to the Singapore Conference, August 1990

[23] The ALEPH Collaboration, "Heavy flavour production in Z decays", Phys Lett B 244, #3,4 p 551 (1990)

[24] J. F. Kral, "Measurement of the Z-Boson Branching Fraction into Hadrons Containing Bottom Quarks", Ph. D. Thesis University of California, Berkeley, LBL-29485, September 1990

[25] The OPAL Collaboration, "A Study of Heavy Flavour Production using Muons in Hadronic Z Decays", CERN-PPE/91-48 March 1991, submitted to Phys. Lett. B.

[26] The L3 Collaboration, "Measurements of Z→bb Decays and the Semileptonic Branching Ratio Br(b→l+X)", L3 Preprint #27, February 1991

[27] John Rees, "The Stanford Linear Collider", Sci. Am. 261 no. 4 p. 8, 1989

[28] G. E. Fischer, "SLAC Site Geology, Ground Motion and Some Effects of the October 17, 1989 Earthquake", SLAC-0358, Dec. 1989

[29] B. W. LeClaire, "A Search for Supersymmetric Electrons with the Mark II Detector at PEP", Ph. D. Thesis, SLAC-Report-321, October 1987

[30] W. Davies-White, *et al*, "A Large Cylindrical Drift Chamber for the Mark II Detector at SPEAR", Nucl. Inst. Meth. **160**, 1979 p. 227-238

[31] J. A. Jaros, "The Mark II Secondary Vertex Detector", in *Proc. of the Int. Conf. on Instrumentation for Colliding Beam Physics*, SLAC-Report-250, Edited by W. Ash, 1982, p. 29

[32] G. Abrams, *et al.*,"The Mark-II Detector for the SLC", Nucl. Inst. Meth. A **281**, 55 (1989)

[33] G. Hanson, Nucl. Instr. and Meth. A252 (1983) 343

[34] K. F. O'Shaughnessy, "Properties of Hadronic Decays of the Z Boson", SLAC-0360, Ph. D. thesis, June 1990

[35] J. Perl, *et al.*, "Track Finding with the Mark-II / SLC Drift Chamber", Nuc. Inst. Meth. **A252**, (1986), p. 616

[36] J. P. Alexander et al., "The Mark II Vertex Drift Chamber", Nucl. Inst and Meth. **A283** (1989) 519

[37] D. Durrett et al., "Calibration and Performance of the Mark II Drift Chamber Vertex Detector", *5th International Conference on Instrumentation for Colliding Beam Physics*, Novosibirsk, USSR March 1990

[38] R. Jacobsen et al., "Recent Experience with Backgrounds at the SLC", presented at the Particle Accelerator Conference, May 1991, San Francisco

[39] R. Jacobsen et al., "Detector Background Conditions at Linear Colliders", *5th International Conference on Instrumentation for Colliding Beam Physics*, Novosibirsk, USSR March 1990, pp. 455-461

[40] R. Jacobsen, "The Silicon Strip Detector at the Mark II", *5th International Conference on Instrumentation for Colliding Beam Physics*, Novosibirsk, USSR March 1990, pp. ???-???

[41] G. Gratta, et al., "The Mark II Silicon Strip Vertex Detector", SLAC-PUB-5443, in preparation

[42] J. Walker, et al., "Development of High Density Readout for Silicon Strip Detectors", Nucl. Inst. Meth. 226: 200, 1984

[43] M. Breidenbach, et al., "Semiautonomous Controller for Data Acquisition: The Brilliant ADC", IEEE Trans. Nucl. Sci NS-25 No. 1 (1978) 706-710 SLAC-PUB-2032

[44] C. Adolphsen et al., "Test Beam Results for Silicon Microstrip Detectors with VLSI Readout", Nucl. Instrum. Meth. **A253** (1987)

[45] A. Breakstone et al.,"Design of a Capacitative Displacement Measuring System for Vertex Detectors at Colliding Beam Machines", Nucl. Instrum. Meth. **A281** (1989) 453-461

[46] C. Field, et al., "A compact beam profile probe using carbon fibres", Nuc. Inst. Meth. A295 (1990) 279-282, SLAC-PUB-5253.

[47] Jordan Nash, "A Measurement of the Resonance Parameters of the Neutral Intermediate Vector Boson", Ph. D. Thesis, Stanford University, January 1990, SLAC-Report-356

References

[48] T. Sjöstrand, Comput. Phys. Commum. **39**, 347 (1986)

[49] T. Sjöstrand and M. Bengtsson, "The Lund Monte Carlo for Jet Fragmentations and e+e- Physics: Jetset version 6.3: An update" Comput. Phys. Commum. **43**, 367 (1987)

[50] S. Stone, in *Proceedings of the 1983 International Symposium on Lepton Photon Interactions at High Energies*, edited by D. G. Cassel and D. L. Kreinick (Cornell Univ.), 1983, p. 204

[51] A. Petersen et al., "Multi-hadronic Events at E(cm) = 29 GeV and Predictions of QCD Models from E(cm) = 29 GeV to E(cm) = 93 GeV", Phys. Rev. D **37**, 1 (1988)

[52] J. D. Bjorken, "Properties of Hadron Distributions in Reactions Containing Very Heavy Quarks", Phys. Rev. D **17**, 171 (1978)

[53] C. Peterson, et al., "Scaling Violations in Inclusive e+ e- Annihilation Spectra", Phys. Rev. D **27**, 105 (1983)

[54] W. Bartel et al.,"Experimental Studies on Multi-Jet Production in e+ e- Annihilation at PETRA Energies", Z. Phys. C **33** 23 (1986)

[55] V. L. Highland, "Some Practical Remarks on Multiple Scattering", Nuc. Inst. Meth. **129** (1975) 497-499 and erratum Nuc. Inst. Meth. **161** (1979) 171

[56] D. E. Amidei, "The Lifetime of the Tau Lepton", Ph. D. Thesis, LBL-17795, May 1984

[57] R. A. Ong, "Measurement of the B Hadron Lifetime", Ph. D. thesis, SLAC-Report-320, September 1987

[58] G. H. Trilling, LBL Physics Note TG360, 1982, unpublished

[59] M. Regler and R. Fruhwirth, "Reconstruction of Charged Tracks", in Techniques and Concepts of High Energy Physics V, T. Ferbel ed.

[60] C. W. Akerlof, "Statistical Estimation of Tracking Resolution". Mark II/SLC Note 62, Feb 17, 1984

[61] R. K. Bock et al., *Formulae and Methods in Experimental Data Evaluation*, European Physical Society, vol. 3, p. I2

[62] M. Abramowitz and I. Stegun, "Handbook of Mathematical Functions", Dover, 1972

[63] Gluckstern, R. L. "Uncertainties in Track Momentum and Direction due to Multiple Scattering and Measurement Errors", Nucl. Instr. and Meth. **24**, 381 - 389 (1963)

[64] C. Adolphsen, *et al.*, "An Alignment Method for the Mark-II Silicon Strip Vertex Detector Using an X-ray Beam", Nuc. Inst. Meth. **A288** (1990) p257-264

[65] P. D. Dauncey, Optical Alignment internal memo, unpublished

[66] The ALEPH Collaboration, "Measurement of the *B* hadron lifetime", preprint CERN-PPE/90-195, 20 December 1990, submitted to Physics Letters B

[67] K. Hayes,"B Tagging at the SLC", Mark II/SLC Note 73, May 8, 1984, unpublished

[68] K. Hayes, "*b* and *c* Quark Exclusive Decays with the Vertex Detector", in Proceedings of the Third Mark II Workshop on SLC Physics, SLAC-315, July 1987

[69] C. K. Jung, et al., "Search for Longlived Massive Neutrinos in Z Decays", Phys. Rev. Lett 64: 1091, 1990

[70] Paul Weber. "Separated Vertex Search and Measurement of the B Hadron Lifetime in e+e– Annihilation at $\sqrt{s}$ = 29 GeV". Ph. D. thesis, Department of Physics, University of Colorado, Boulder, Colorado, 1990

[71] B. A. Schumm for the Mark II Collaboration, "High Precision Tracking and the Measurement of B(Z→bb)/B(Z→hadrons)", to be published in the proceedings of the 25th Recontres de Moriond, LBL-30709, March 1991.

[72] The ALEPH Collaboration, "Heavy flavour production in Z decays", Physics Letters **B244** pp. 551 - 565, July 1990

[73] The ARGUS Collaboration, "Measurement of the Lifetime Ratio τ(B+)/τ(B0)", DESY 89-117, September 1989

[74] E. H. Thorndike and R. A. Poling, "Decays of the b Quark", Physics Reports 157, 3, p 202 (1988)

[75] The DELPHI Collaboration, "A Measurement of the Partial Width of the Z Boson into Charm Quark Pairs", Phys Lett B 252 #1 p 140 (1990)

[76] D. Goldberg, "What Every Computer Scientist Should Know About Floating-Point Arithmetic", ACM Computing Surveys, Vol. 23 Number 1, March 1991 pp5 - 48.

Nothing is more demanding than drafting original prose.

Winston Churchill

Colophon

This thesis was laid out with FrameMaker 2.1 on the Apple Macintosh. The body text is set in 11 point New Century Schoolbook with 7 point leading. Chapter headings are in 18 point Optima with 36 point numbers. Section headings are smaller sizes of Optima.

Equations were set with FrameMath, except some of the more complex matrix equations in Appendix B required MathType for proper layout.

Drawings were done using Adobe Illustrator 88 and Adobe Illustrator 3.0. The on-line archives of the SLAC Publications Department were invaluable. Most plots were laid out with DeltaGraph 1.5, with minor editing done using Illustrator.